Dissertation

Zur Erlangung des akademischen Grades
„Doktor der Naturwissenschaften“
im Promotionsfach Geologie/Paläontologie

am Fachbereich
Chemie, Pharmazie und Geowissenschaften
der Johannes Gutenberg-Universität Mainz

Reactive flow in porous media based on numerical simulations at the pore scale

vorgelegt von

Christian Hinz

geboren in Dieburg

Mainz, September, 2019

Arbeitsgruppe Hydrogeochemie

Institut für Geowissenschaften

Johannes Gutenberg – Universität Mainz

Abstract

Long-term evolution of permeability and tortuosity due to porosity changes evoked by reactivity of aqueous solutions is of paramount importance for predicting water-rock interaction. This challenge is best tackled by introducing pore-scale modeling, where the modeling domain is a high-resolution tomographic image of the porous media. This thesis presents such a novel reactive fluid dynamics modelling approach combining numerical flow, transport and geochemical solvers. A voxel based Navier-Stokes-Brinkman solver in a finite volume formulation is coupled to the thermodynamic equilibrium code PhreeqC. A Lagrangian transport approach realizes the sequential simulation of advection, diffusion and reaction. Virtual particles transport aqueous solutions that equilibrate with the pore fluid. The thus changed species distributions potentially induce local disequilibria at reactive grain surfaces and initiate dissolution and precipitation reactions. The novel approach enables to couple at high spatial and temporal resolution transport with reactivity of the fluid, and the quantity of mineral alteration in the pore matrix depending on both, the local geochemical equilibrium and mineral phase reaction kinetics. The approach is realized by high-performance parallelized computations that are performed directly on the voxel grid of digital rock samples. SrSO4 precipitation is modelled with a diffusive geochemical system in a sand grain matrix. Retreat of calcite cements in a sandstone matrix due to dissolution reactions is directly visualized by digital rock physics experiments. Results highlight the necessity of concerning the effect of local pore alterations on the development of system-specific transport parameters.

Zusammenfassung

Die Entwicklung von Permeabilität und Tortuosität, ausgelöst durch reaktive wässrige Lösungen, ist von größter Bedeutung für die Vorhersage von Fluid-Gestein-Interaktionen. Modellierungen auf der Porenskala, in einem hochauflösenden tomographischen Bild der porösen Medien, können diese Herausforderung am besten bewältigen. Die vorliegende Dissertation stellt einen neuartigen reaktiven fluiddynamischen Modellierungsansatz vor, der numerische Strömungs-, Transport- und geochemische Löser kombiniert. Ein voxelbasierter Navier-Stokes-Brinkman-Löser mit endlicher Volumenformulierung ist mit dem thermodynamischen Gleichgewichtscode PhreeqC gekoppelt. In einem Transportansatz nach Lagrange realisieren virtuelle Partikel die Simulation advektiven und diffusiven Transports wässriger Lösungen, die mit dem Porenfluid equilibriert werden. So können lokal Ungleichgewichte an reaktiven Mineraloberflächen entstehen und Lösungs-, bzw. Fällungsreaktionen auslösen. In hoher zeitlicher und räumlicher Auflösung werden Transport, Fluid-Reaktivität und Veränderungen der Mineralmasse in der Porenmatrix gekoppelt; abhängig sowohl vom lokalen geochemischen Gleichgewicht als auch von der Reaktionskinetik der Mineralphase. Der reaktive Transport wird mit leistungsstarken parallelisierten Berechnungen direkt auf dem Voxelgitter digitaler Gesteinsproben realisiert. Sowohl SrSO4 Ausfällung in einer diffusionskontrollierten Sandkornmatrix als auch die Auflösung von Kalzitzementen eines Reservoirsandsteins werden simuliert. Die Ergebnisse zeigen die Notwendigkeit, den Effekt lokaler Porenraumveränderungen bei der Entwicklung systemspezifischer Transportparameter zu berücksichtigen.

Acknowledgements

I would like to thank my supervisors for supporting my research efforts with their valuable knowledge about geochemistry and the scientific way. Furthermore, I would like to highlight their efforts for guiding me through this thesis. They assisted me with essential advises, discussions and further support. The Math2Market team are thanked for specific code adaptions and their helpful support. I want to thank my colleagues for proof-reading, valuable discussions, time-consuming µCT measurements and the according reconstruction, phase segmentation and 3d-imaging.

In addition, I would like to express my gratitude to all those, that assisted me throughout my studies. Among those I want to mention my wife and my parents for their persistent support throughout my studies, as well as my friends and fellow students for valuable discussions.

My research is part of the research project HyINTEGER, which was approved for three years. I am grateful for the funding of my work, which was granted by the Federal Ministry for Economic Affairs and Energy (BMWI; funding number: 03ET6073).

I am grateful for the availability of the µCT generated digital geometries: (1) the sand grain geometry measured with a CT-alpha 160 (Procon, Germany) at the university of Mainz. (2) The Kreuznach sandstone structure that was measured at the TOMCAT beamline of the SLS at the PSI Villigen (Switzerland) in 2010. (3) The sandstone structure from the Rotliegend formation measured in 2018. I acknowledge DESY (Hamburg, Germany), a member of the Helmholtz Association HGF, for the provision of experimental facilities. Parts of this research were carried out at PETRA III and I would like to thank the beamline scientists in charge for assistance in acquiring the µCT scans of the rock sample at the P05 imaging beamline.

Table of contents

List of figures

List of tables

Abbreviation index

BC	Boundary Conditions
C-S-H	Calcium Silicate Hydrate
CentOS	Community Enterprise Operating System
CFD	Computational Fluid Dynamics
Da	Damköhler number
DESY	German Electron Synchrotron
DRP	Digital Rock Physics
EB	Error Bound (flow field accuracy)
EOR	Enhanced Oil Recovery
GCC	GNU Compiler Collection
GUI	General User Interface
HPC	High-Performance Computing
IAP	Ion Activity Product
ICP-OES	Inductively Coupled Plasma Optical Emission Spectrometry
ITWM	Fraunhofer-Institut für Techno- und Wirtschaftsmathematik (Kaiserslautern, Germany)
LBM	Lattice Boltzmann Methods
LIR	Left-Identity-Right (flow field solver)
µCT	Micro-Computed Tomography
MPI	Message Passing Interface
NSB	Navier Stokes-Brinkman
OpenMP	Open Multi-Processing
OS	Operating System
pCO_2	CO_2 partial pressure
PETRA	Positron-Electron Tandem Ring Accelerator
PSI	Paul Scherrer Institute (Villigen, Switzerland)
REV	Representative Elementary Volume
ROI	Region Of Interest
SB	Stokes-Brinkman
SI	Saturation Index
SRCT	Synchrotron Radiation Computed Tomography
SSA	Specific Surface Area
TOMCAT	Tomographic Microscopy and Coherent Radiology Experiments (SRCT beamline)
USGS	United States Geological Survey
VSA	Voxel surface area

Formula index

Symbol	SI Unit	Name
{ }		Ion activity
$\boldsymbol{A}$	m^2	(Cross-sectional) area
$\boldsymbol{A_s}$	m^2	(Reactive) surface area
$\boldsymbol{A_{s,0}}$	m^2	Initial surface area
$\boldsymbol{c}$	$mol\ m^{-3}$	Molar concentration of aqueous species (commonly: $mol\ L^{-3} = M$)
$\boldsymbol{c_p}$	$mol\ m^{-3}$	Molar mineral phase concentration
$\boldsymbol{C_c}$	*dimensionless*	Cunningham correction factor
$\boldsymbol{D_{grains}}$	m	Grain diameter
$\boldsymbol{D}$	$m^2\ s^{-1}$	Diffusion coefficient
$\boldsymbol{D_m}$	$m^2\ s^{-1}$	Molecular diffusion coefficient
$\boldsymbol{dx_{vl}}$	m	Voxel length
$\boldsymbol{\Delta x}$	m	Average distance (of particle displacement)
$\boldsymbol{Da}$	*dimensionless*	Damköhler number
$\boldsymbol{f_{roughness}}$	*dimensionless*	Surface roughness factor
$\boldsymbol{IAP}$	*dimensionless*	Ion activity product
$\boldsymbol{K_{sp}}$	*dimensionless*	Thermodynamic solubility product (g species per g solution)
$\boldsymbol{k_B}$	$J\ K^{-1}$	Boltzmann constant ($k_B = 1.38064852\ 10^{-23}\ J\ K^{-1}$)
$\boldsymbol{\kappa}$	m^2	Permeability (commonly listed in darcy (d): $1d \approx 10^{-12} m^2$); Kappa ($\boldsymbol{\kappa}$) is used instead of K to avoid confusion with the solubility
$\boldsymbol{l}$	m	Length
$\boldsymbol{m}$	kg	Mass
$\boldsymbol{moles}$	mol	Amount of moles
$\boldsymbol{\mu}$	$Pa\ s = kg\ m^{-1}\ s^{-1}$	Dynamic viscosity
$\boldsymbol{\mu\ \kappa^{-1}}$	$kg\ m^{-3}\ s^{-1}$	Flow resistivity
$\boldsymbol{\nu}$	$m^2\ s^{-1}$	Kinematic viscosity
$\boldsymbol{p}$	Pa	Pressure
$\boldsymbol{Pe}$	*dimensionless*	Péclet number
$\boldsymbol{Pe_{grid}}$	*dimensionless*	Grid Péclet number
$\boldsymbol{\phi}$	*dimensionless*	Porosity
$\boldsymbol{Q}$	$m^3\ s^{-1}$	Volumetric flow rate
$\boldsymbol{R}$	m^3	Gas constant ($\boldsymbol{R} = 8.3144598\ J\ mol^{-1}\ K^{-1}$)
$\boldsymbol{r_p}$	m	Particle radius
$\boldsymbol{R_k}$	$mol\ m^{-2}\ s^{-1}$	Overall kinetic reaction rate of mineral phases
$\boldsymbol{r_k}$	$mol\ m^{-2}\ s^{-1}$	Specific kinetic reaction rate for phase k
$\boldsymbol{r_f}$	$mol\ m^{-2}\ s^{-1}$	Forward rate for kinetic reactions
$\boldsymbol{r_b}$	$mol\ m^{-2}\ s^{-1}$	Backward rate for kinetic reactions
$\boldsymbol{Re}$	*dimensionless*	Reynolds number

Symbol	SI Unit	Name
$\boldsymbol{\rho}$	$kg\ m^{-3}$	Density
$\boldsymbol{SI}$	*dimensionless*	Saturation Index
$\boldsymbol{sc}$	*dimensionless*	Stoichiometric coefficient
$\boldsymbol{SSA}$	m^{-1}	Specific surface area in $m^2\ m^{-3}$
$\boldsymbol{t}$	s	Time
$\boldsymbol{T}$	K	Temperature (also: $°C = -273.15\ K$)
$\boldsymbol{u}$	$m\ s^{-1}$	Velocity
$\boldsymbol{V}$	m^3	Volume
$\boldsymbol{VSA}$	m^{-1}	Voxel surface area
$\boldsymbol{\vec{W}}$	*dimensionless*	Wiener measure

1 Introduction

Reactive transport in pore scale porous media is both an experimental and numerical challenge. Recent technical advancements in synchrotron facilities and X-ray micro-computed tomography (µCT) scanners enable time-resolved in-situ measurements of pore scale dissolution and precipitation experiments (Menke et al., 2016; 2017; 2018). This development is accompanied by continuous advances in computer technology. Thus, computationally expensive simulations can be performed in increasingly suitable computational times at modern high-performance workstations and clusters. Numerical approaches are still rare at the pore scale, although reactive transport modeling has become an essential tool for the analysis of coupled physical, chemical, and biological processes in Earth systems at various scales (Steefel et al., 2005). Accordingly, this thesis provides a significant contribution for enhancements in pore scale reactive flow simulations. The presented reactive flow model sequentially couples fluid physics to hydrogeochemistry. It considers reaction calculations at the voxel scale while tracking spatial changes at the sub-voxel scale. Additionally, the code applies a high temporal resolution while offering a scaling factor for kinetic pore alteration in order to enable efficient reactive transport simulations in a parallelized computing environment.

1.1 Scales and applications

Numerical simulations of reactive transport in subsurface environments are performed across different geological length scales. The field or reservoir scale is of main interest for the oil and gas industry, contaminant transport e.g. in aquifers (Bear and Cheng, 2010), geothermal energy (Bonte et al., 2014; Guarracino et al., 2014), storage of nuclear waste (Xiong et al., 2015; Xie et al., 2011) and gas storage applications such as CO_2 sequestration (Sell et al., 2013) or CO_2 storage in general (Blunt et al., 2013) and hydrogen underground reservoirs (Yekta et al., 2018; Flesch et al., 2018). At the continuum scale, fluid transport and water-rock interactions are quantitatively described on basis of an idealized mathematical characterization of the physical system (Steefel et al., 2015). However, that scale relies on a statistical simplification of the pore scale, which in contrast incorporates individual pores and grains typically identified via µCT measurements and image processing methods. Rock-describing parameters obtained from reactive transport simulations at this microscopic scale can potentially be upscaled to a macroscopic scale individually ranging from mesoscale to the reservoir scale. In general,

petrophysical properties obtained at the pore scale can be applied to the core scale, if a representative elementary volume (REV) was used for the numerical simulations. Thus, reservoir scale applications such as the enhanced oil recovery (EOR) in petroleum engineering (Wei, 2012) require pore scale experiments (Leu et al., 2014; Bartels et al., 2017) and simulations (Maheshwari et al., 2013). Pore scale models also become increasingly important in contaminant and colloidal reactive transport (Oostrom et al., 2016). For reactive transport models at the pore scale, the consideration of sub-micron scales might also be of interest in order to account for potentially heterogeneous phenomenon such as locally varying mineral dissolution rates (Fischer et al., 2012). Reaction rates are proportional to the available surface area if not restricted by transport processes. The ratio between the actual surface area and the geometric surface area is described by the surface roughness factor ($f_{roughness}$), which influences the mineral dissolution rates (Deng et al., 2018). Coupled experimental and numerical approaches implicate the necessity of incorporating complex domain geometries for modeling reactive transport (Stoll et al., 2018).

Although the last two decades have seen numerous efforts in coupling different problems in porous media (e.g., Enzmann, 2000; Drießen et al., 2015), numerical codes are still often limited in solving a specific set of physical processes (Nardi et al., 2014). Nevertheless, several codes are capable of simulating reactive transport at the continuum scale by coupling fluid dynamics and chemistry such as PhreeqC (Parkhurst and Appelo, 2013), OpenGeoSys (Kolditz et al., 2012), TOUGHREACT (Xu et al., 2012), PFLOTRAN (Hammond et. al, 2012) and CRUNCHFLOW (Steefel and Lasaga, 1994; Steefel et al., 2015), which are benchmarked amongst others by Steefel et al. (2015). The coupling of 3D transport and PhreeqC has been accomplished by e.g., PHT3D (Prommer and Post, 2010) and iCP (Nardi et al., 2014). Pore scale models might improve predictions of the above mentioned models, when more insight is necessary. Pore scale results may be upscaled to fit to continuum scale models by applying a volume averaging method, when simulations are performed in representative elementary volumes (Lichtner and Kang, 2007). Apart from improving and validating continuum descriptions, pore scale modeling also aims at identifying the key parameters and physicochemical processes, which control the macroscopic phenomena (Lichtner and Kang, 2007; Oostrom et al., 2016).

Pore scale reactive transport models require an increased computational performance and thus, few research is published. Yoon et al. (2012; 2017) modeled the precipitation of calcite in

synthetical 2D geometries. Gao et al. (2017) propose a geochemical numerical model for kinetically dissolving calcite upon carbonic acid reactions during purely diffusive transport. However, in the study of Gao et al. (2017) two billion time steps and 2,048 cores were required for simulating 1,600 days in total. In contrast to other studies (e.g., Yoon et al., 2015), the model is validated against an experiment (Gao et al., 2017). For the purpose of enhanced oil recovery (EOR), Maes and Geiger (2018) simulate the effect of a reactive fluid phase during multiphase flow modeling. Pereira Nunes et al. (2016) simulate carbonate dissolution in µCT images at the pore scale using a particle-based method. They successfully predicted the experimental increases in porosity and permeability of Menke et al. (2015), however by applying the dissolution rate known a priori as input parameter. Cvjetkovic et al. (2018) use a similar method for acidizing treatments in carbonate rocks, but they apply a fixed pH value as constant input and thus derive a varying dissolution rate. With varying constant flow velocity inputs, they reproduce the dissolution regimes presented by Maheshwari et al. (2013).

Accordingly, predictive pore scale models for reactive fluids are still a challenging task (Oostrom et al., 2016), especially when it comes to a general applicability on different hydrogeochemical systems at different time scales and at an appropriate computational performance.

1.2 Research project HyINTEGER

In the energy transition time, it is essential to have methods for storing excess energy from renewable energy sources and recover it if energy demand is higher than production. With energy consumption, hydrogen can be produced from water and then stored in geological underground reservoirs such as depleted oil and gas fields. From there, it can be recovered and converted back to energy (Flesch et al., 2018). HyINTEGER investigates the integrity of wells and technical components exposed to highly corrosive conditions in geological hydrogen underground reservoirs (www.hyinteger.com). Therefore, sandstones were exposed to hydrogen in highly saline formation fluids under respective temperature and pressure realized with autoclave experiments. The experiments were accompanied with microscopic, petrophysical and µCT-based analyses before and after. Based on their results, Flesch et al. (2018) propose the applicability of hydrogen injection into reservoirs in consideration of the geological and geochemical conditions. Depending from the sample locations, they observed the dissolution of pore filling cements. Anhydrite ($CaSO_4$) and Carbonates ($CaCO_3$) were

dissolved due to the acidification of the formation fluid during hydrogen injection. However, ongoing research still has to validate the integrity of the technical wellbore components for determining whether hydrogen storage in underground reservoirs is safe (Flesch et al., 2018).

The linking of simulations at the reservoir scale (e.g., Hagemann, 2018) to such pore altering experiments requires insights into the development of the hydromechanical transport parameters. The aim of this thesis is resolving the process of pore cement dissolution by means of digital reactive flow experiments at the pore scale. Therefore, a code was developed, which emphasizes both the high computational effort and the advantages of the simulation of reactive fluid dynamics at the pore scale. However, there are still open questions considering reaction kinetics e.g. at high temperature-pressure conditions and high salinity. Nevertheless, thermodynamic equilibrium calculations can be performed at these conditions (Appelo, 2015), which enables the accomplishment of the aimed task within the scope of the HyINTEGER project.

1.3 The reactive transport code

The presented code is based on a workflow combining numerical flow and transport solvers coupled to a geochemical calculation code. It has been developed according to the operator splitting approach realized by an MPI-parallelized C++ script. The GeoDict software package (Math2Market GmbH, Germany) iteratively computes the flow field in voxel-based geometries and simulates the motion of virtual particles in the pore space. The PhreeqC code performs hydrogeochemical reaction calculations that are fully coupled with flow and transport.

The GeoDict module FlowDict computes the flow field employing the Navier Stokes-Brinkman (NSB) equation. The module AddiDict simulates the advective and diffusive motion of the virtual particles. These particles carry inflow solutions and mix with a pore fluid (initially in equilibrium with the structure) at the voxel scale. The C++ library of PhreeqC (IPhreeqc) is implemented to perform reactions at the computing domain considering kinetically controlled geochemical equilibrium thermodynamics. Due to dissolution and precipitation, porous voxels evolve and influence the local porosity and permeability of the digital geometry. The structures used are usually derived from preceding X-ray µCT measurements. Accordingly, the advantage of such digital experiments is based on offering a non-destructive option for analyzing and characterizing porous media concerning the evolution of its petro-physical parameters (Saenger

et al., 2011). The reactive transport simulations are realized by a time loop resulting in the time-resolved development of geochemical and petrophysical properties such as the porosity-permeability relationship according to the Digital Rock Physics (DRP) concept.

2 Fundamentals of reactive flow

This chapter presents the basic scientific principles summarized in Fig. 1 at a level sufficient to understand the processes implemented in the reactive fluid model. This is to embrace the dynamics of fluid flow behavior, the transport of geochemical species and water-rock interactions in geological porous media at the pore scale.

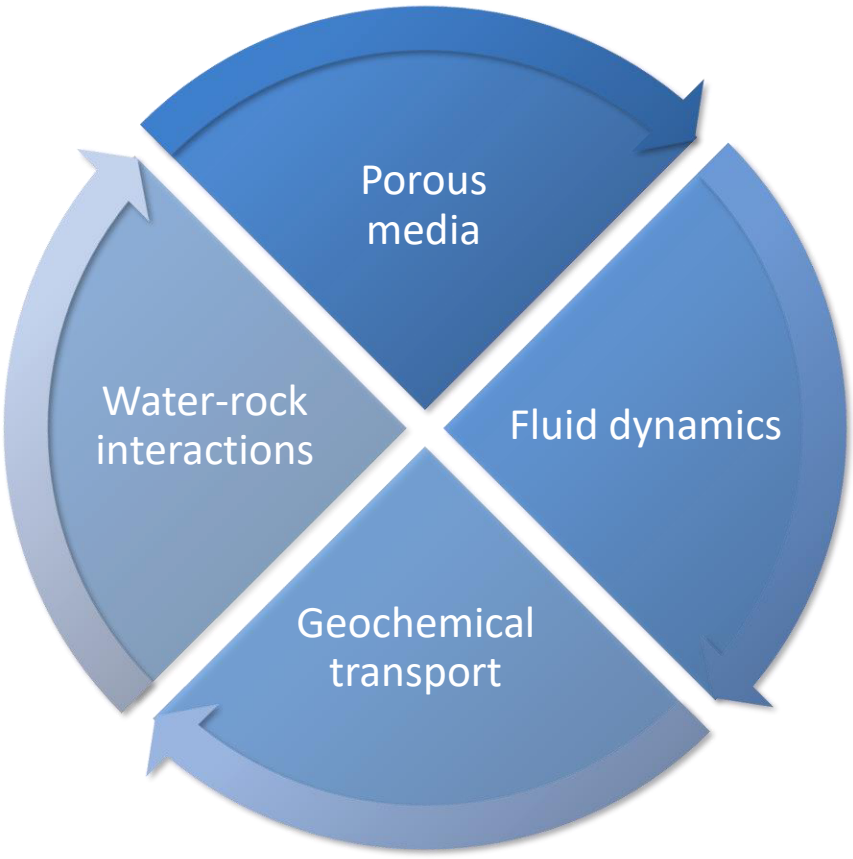

Fig. 1. General processes

This cycle comprises the general processes discussed in this thesis. Starting point is a digital rock geometry at the pore scale. The flow properties of that structure are numerically determined and used to simulate geochemical transport. Reaction calculations are performed at water-rock interfaces, potentially resulting in pore alteration. Continuous structure changes result in repetitions of that cycle, since dissolution and precipitations of any kind modify the pore morphology and in turn directly affect flow and transport processes (Norouzi Rad et al., 2013).

2.1 Porous media

A porous medium in geosciences considers a structure such as a rock or unconsolidated sediments consisting of solid components and a void space (pores). The pore space contains gaseous and/or liquid phases while the solid phase consists of one or multiple mineral phases.

The porosity (ϕ) is defined as the fraction of void spaces in the porous medium. In order to achieve fluid flow in a geomaterial, it has to be permeable, i.e. the pore space has to be connected (Hölting and Coldewey, 2005).

In order to obtain digital 3D geometries at pore scale resolution, micro-computed tomography measurements (µCT) are typically performed. This non-destructive technique is capable of characterizing rock samples at resolutions down to a few hundred nm (Cnudde and Boone, 2013). The image resolution however depends on the sample size and thus, the specimen may require diameters down to 1 mm for high-resolution CT (Cnudde et al., 2009). A common setup is the cone-beam µCT (Feldkamp et al., 1984) shown in Fig. 2. The sample is centered on a rotation stage while penetrated by the X-ray beam. The detector measures the received beam intensity. In addition to such laboratory instruments, synchrotron facilities also offer the possibility to measure at a higher energy flux leading to an increase in image resolution and measurement speed. At such facilities, electrons are accelerated to near light speed in an electron accelerator while magnetic fields force them into a circular orbit. So, electromagnetic radiation is emissioned, which is called synchrotron light. At synchrotron radiation computed tomography (SRCT) setups, a polychromatic X-ray beam is generated passing a monochromator (Fig. 2) to select an energy bandwidth. The beam is then attenuated by the rotating sample while the scintillator screen collects the beam energy and converts it to visible light (Cnudde and Boone, 2013). Optical magnification lenses can thus improve the spatial resolution of images (Koch et al., 1998) detected with SRCT setups.

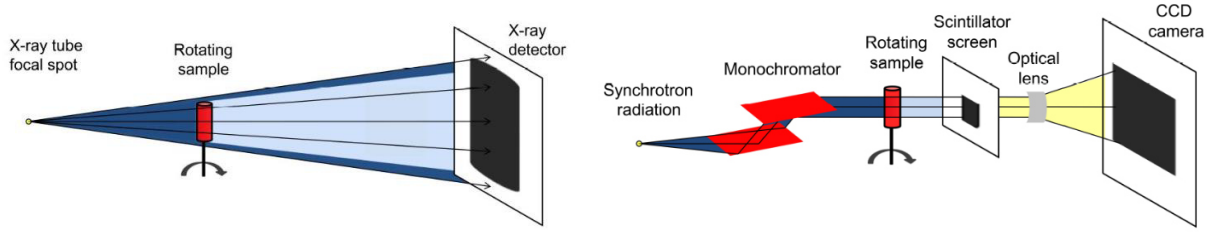

Fig. 2. Schematic setup of µCT and SRCT (Cnudde and Boone, 2013)
Standard setups are schematically illustrated for a cone-beam µCT (left) and the SRCT (right) as published by Cnudde and Boone (2013).

First step of post-processing is that the raw data needs to be reconstructed to a 3D image matrix yielding in millions or billions of voxels, which is the term for 3D pixels. Therefore, the initial stack of 2D image slices requires a transformation to 3D objects consisting of 3D voxels instead of 2D pixels by applying a reconstruction algorithm (e.g., Marone and Stampanoni, 2012).

Subsequently, several image artifacts such as beam hardening, the cone-beam effect and the phase contrast have to be considered for correctly determining the different phases in the greyscale image (Cnudde and Boone, 2013). The 3D image processing usually requires various grayvalue filtering methods typically including the non-local means (NLM) filter (e.g., Buades et al., 2005) and can be performed with available software tools such as the GeoDict software package and Avizo (FEI). The following phase segmentation step is most important for quantitative pore space analysis and subsequent fluid dynamics modeling (Iassonov et al., 2009). The identification of phases is usually done via grey value thresholding. Despite the present operator dependency of the resulting 3D images (Cnudde and Boone, 2013), machine learning segmentation tools (e.g., Chauhan et al., 2018) have not yet caught on.

The digital rock physics (DRP) concept aims at obtaining macroscopic rock properties such as the permeability and elastic moduli (Andrä et al., 2013a; 2013b) from digital 3D rock samples. Conclusions based on experimental measurements or numerical simulations at the micron scale require the selection of an according region of interest (ROI) concerning a given property (Bear, 1972; Saxena et al., 2017). Such a volume is subsequently referred to as representative elementary volume (REV), which is favorable for parameter determinations according to the DRP concept. For porous media, Bear and Cheng (2010) state that a REV contains average values for the geometrical characteristics of the pore space at an acceptable error and at rather constant average values over a series of different regions of interest (ROIs). However, the determination of an REV for heterogeneous porous media is rather complex in comparison to periodic media. Singh (2017) proposes spatiotemporal REVs for reactive flow simulations in digital rock samples. Thus, the determination of an REV in a reactive environment might require the coupling of the spatial scale with the temporal scale. The REV size increases due to increasing heterogeneity during reaction-induced pore alteration (Singh, 2017). Menke et al. (2018) summarize that the scale dependence of pore alterations induced by reactive transport has not yet sufficiently been investigated and is thus subject of future research.

2.2 Fluid dynamics

Fluid dynamics describe the flow of fluids. That might concern multiple phases being liquid or gaseous. The physical flow properties in 3D geometries can be computed by applying computational fluid dynamics (CFD) software such as GeoDict, Fluent (ANSYS, Inc.) or

OpenFOAM (OpenCFD Ltd). At the pore scale, fluid flow is characterized by advection. The stationary flow field of a digital sample can be computed by solving the (Navier) Stokes-(Brinkman) system of equations (NSB) resulting in a 3D flow field. The Stokes equation may be extended by a Navier part stating the inertia term and thus accounting for non-linear flow. The Brinkman term allows for concerning microporous voxels for the flow computation by applying a viscous flow resistivity. The NSB conservation of momentum is solved based on a given pressure gradient (∇p on $\Omega \subset [0, \mathrm{l_x}] \times [0, \mathrm{l_y}] \times [0, \mathrm{l_z}]$):

$$\underbrace{-\mu\Delta\vec{u}}_{\text{Stokes}} + \underbrace{(\rho\nabla\vec{u})\vec{u}}_{\text{Navier}} + \underbrace{\mu\kappa^{-1}\vec{u}}_{\text{Brinkman}} + \underbrace{\nabla p = \vec{f}}_{\text{conservation of momentum}} \tag{1}$$

Next to the velocity tensor ($\vec{u}$), the Stokes part of the equation considers the dynamic viscosity (μ) while the Navier part concerns for the density (ρ). The Brinkman term takes into account a given flow resistivity tensor calculated from local permeability values. The conservation of mass is described by $\nabla \cdot u = 0$ on Ω. For this study, the velocity on solid surfaces is defined as No-slip ($u = 0$). Different boundary conditions (BC) can be applied to the image edges, ranging from encasements and No-slip boundaries to periodic structure repetitions and structure "mirrorings".

Darcy's law describes laminar flow through a pore system. The applied flow solver calculates the permeability (κ) from the law according to the given parameters as shown in Eq. (2). Permeability describes the potential of fluids to flow through a specific porous media. However, κ is depending from the given pressure gradient and thus, the permeability values calculated in this thesis do not represent intrinsic rock properties.

$$\kappa = \frac{Q \times A}{\mu} \times \frac{\Delta p}{l} \tag{2}$$

The rearrangement of Darcy's law relates the volumetric flow rate (Q) and the pressure gradient (Δp) in flow direction to the dynamic fluid viscosity (μ) according to the object dimensions. The volume is considered by the area of the cross section (A) and the digital rock length (l) in flow direction. However, the law is true only for laminar flow.

Additional approaches are capable of calculating the permeability depending from the digital geometry. Eq. (4) is a simplification of the cubic law and in this state however only true for parallel plates (Schwarz and Enzmann, 2012):

$$\kappa = \frac{(\phi \times l)^2}{12} \tag{4}$$

The permeability is calculated in consideration of the porosity (ϕ) and characteristic length (l).

The Kozeny-Carman equation estimates the permeability at laminar flow regimes and single-phase fluid flow by considering an average grain diameter (D_{grains}) and a typical proportionality and unity factor ($a = 0.8 \cdot 10^6 / 1.0135$). Eq. (5) is derived by Kozeny (1927) and Carman (1937):

$$\kappa = \frac{a \times {D_{grains}}^2 \times \phi^3}{(1-\phi)^2} \tag{5}$$

However, a mismatch between directly compared experimental and computed properties of heterogeneous material is expectable when relating volumes of different sizes with each other. Thus, a comparison of trends is more favorable such as permeability versus porosity (Dvorkin et al., 2011).

The lattice Boltzmann method (LBM) is another approach for simulating fluid flow. This method models flow by simulating the transport of fictive particles, which propagate according to the Boltzmann equation. LBM is also used in reactive transport models (Yoon et al., 2015; Gao et al., 2017).

2.3 Geochemical transport

Transport at the pore scale is characterized by both advection and diffusion. Advective transport follows the motion of the fluid according to the flow field. Diffusion is the spreading of molecules or solids typically from areas with high concentration towards areas with low concentration. It is based on random motion that results from collisions within the fluid. This so-called Brownian motion was first observed by R. Brown and decades later proven by Einstein (1905). The diffusion coefficient (D) describes the mobility of a solute and is defined

as mean square distance it travels in a certain time. The concentration (c) change in a liquid over time (t) is shown at the advection-diffusion transport equation:

$$\frac{\partial c}{\partial t} = \underbrace{-\nabla(\vec{u}c)}_{\text{advection}} + \underbrace{\nabla(D_m \nabla c)}_{\text{diffusion}} + R \tag{6}$$

The value R describes enhancement ($R > 0$) or reduction ($R < 0$) of the concentration. Advection is determined by the flow field ($\vec{u}$) while the Brownian motion is described by the concentration gradient change in dependence of the molecular diffusion coefficient (D_m). The general interplay of both motions is depicted in Fig. 3 for geological porous media. Along the streamlines, advection dominates the transport while diffusive motion determines concentration changes at the microporous layer.

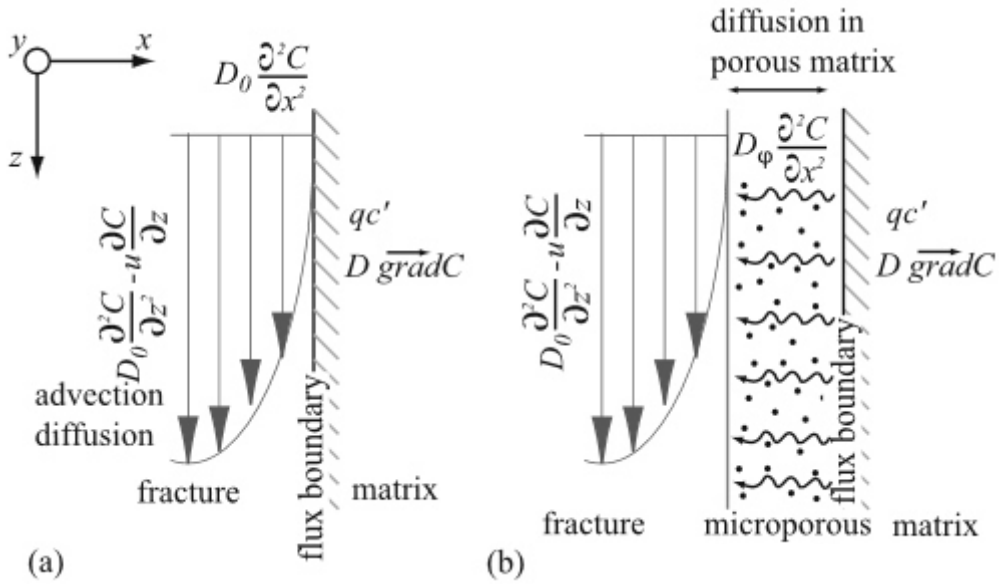

Fig. 3. Advection and diffusion (Noiriel et al., 2007)

Schematic representation of transport phenomena along streamlines, shown here as fracture (Noiriel et al., 2007). (a) Advection typically dominates along the flow path (b) while diffusion dominates in the porous matrix that is not supporting the main flow paths, here shown as microporous layer.

The simulation of combined advective and diffusive transport is realized by either the Lagrangian or the Eulerian approach. The latter solves the species distribution numerically while the Langrangian transport utilizes particles to transport species and solids. According to Benson et al. (2017), particle transport methods show the potential for simulating reactive transport at the field scale more accurately. Such methods circumvent the problems of advection errors in the numerical method and the subsequent artificial mixing in the Eulerian method.

Diffusivity of solids in the fluid (particles) at a certain diameter can be described by the Stokes-Einstein equation:

$$D = \frac{C_c \times k_B \times T}{3\,\pi \times \nu \times \rho \times r_p} \tag{7}$$

The equation uses the Boltzmann constant (k_B), the temperature in K (T), the kinematic viscosity (ν), the fluid density (ρ), the particle radius (r_p) and the Cunningham correction factor (C_c), which concerns for slip occurring at fluid-solid interfaces (Cunningham, 1910).

The average distance (Δx) particles travel in a certain time depends from the diffusivity (Smoluchowski, 1906; Lavenda, 1985) and can thus be calculated:

$$\Delta x = \sqrt{2D \times t} \tag{8}$$

The interplay between advection and diffusion is measured by the Péclet number (Pe), which is defined as ratio between advective and diffusive transport rate. Accordingly, advection dominates at $Pe > 1$. If applied at the voxel scale, a grid Péclet number (Pe_{grid}) can be calculated by relating the local velocity (u) and the voxel length (dx_{vl}) to the molecular diffusion coefficient (D_m):

$$Pe_{grid} = \frac{u \times dx_{vl}}{D_m} \tag{9}$$

The interplay of liquids at different composition is controlled (1) by transport concerning the locations and (2) by geochemistry determining the result of aqueous fluid mixing or respectively, geochemical equilibration. In geochemical modeling codes, the compositions are mixed at a certain percentage. The resulting aqueous solution is subsequently equilibrated concerning parameters such as the pH value.

2.4 Water-rock interactions

Fluids might interact with a solid material at rock surfaces. In this study, various topics such as sorption (e.g., Hayes et al., 1991), double layers (e.g., Lauw et al., 2010) and surface charge in general (Hunter, 1981) are neglected while focusing on (kinetic) equilibrium reactions and subsequent pore alteration. Aqueous solutions are tracked at the voxel scale. Accordingly,

reactions are controlled by both transport and kinetics if applied. Reactions at water-rock interfaces may lead to precipitation or dissolution of mineral phases at the sub-voxel scale. Pore alterations affect the accessible pore space and thus the flow field and the geochemical transport in general. Eq. (6) is therefore extended to the advection-reaction-diffusion equation:

$$\frac{\partial c}{\partial t} = -\nabla(\vec{u}c) + \nabla(D_m \nabla c) - \frac{\partial c_p}{\partial t} \tag{10}$$

The concentration gradient that changes over time is additionally influenced by the mineral phase concentration (c_p) gradient, which is also developing with time. Accordingly, fluid dynamics and geochemical transport have to be adjusted according to the phase changes. An important measure for the accuracy of reactive fluid models is determined by the ratio of the temporal resolution of CFD and transport simulations related to the amount of pore alterations. This temporal resolution is described by the time step that controls the general sequence illustrated in Fig. 1.

Several open-source codes are capable of calculating geochemical equilibrium reactions in reactive transport models. Among those are PhreeqC (Parkhurst and Appelo, 2013), GEMS (Kulik et al., 2013) and Reaktoro (Leal et al., 2017; Leal et al., 2015). Parkhurst and Wissmeier (2015) published PhreeqcRM, which is a specific reaction module for transport simulators based on PhreeqC.

In geochemical equilibrium thermodynamics, precipitation and dissolution of mineral phases is controlled by the law of mass action. Therefore, activities (indicated with curly brackets) of the reactants have to be considered. Eq. (11) shows the corresponding relationship between the stoichiometric coefficients a and b and the reactants A and B:

$$A_a B_b = a\{A\} + b\{B\} \tag{11}$$

In principal, the equilibrium constant (K_{sp}) of a given phase is set equal to the activities (indicated with curly brackets) of the reactants A and B with the stoichiometric coefficients as exponents a and b. The reactant activities would here need to be divided by the pure solid phase activity, which is however set to 1 by convention. Eq. (12) shows this representation approach and also a more generalized equation for pure-phase equilibria according to Parkhurst and Appelo (1999). K_{sp} is the product of the activities of each master species m with the exponent

$sc_{m,p}$ meaning the stoichiometric coefficient of the according master species in the dissolution reaction (Parkhurst and Appelo, 1999).

$$K_{sp} = \{A\}^a\{B\}^b = \prod_{m}^{M_{aq}} \{m\}^{sc_{m,p}} \tag{12}$$

From the thermodynamic solubility product (K_{sp}) and the ion activities, the saturation index (SI) is calculated describing the potential for precipitation and dissolution of mineral phases. When the SI is above zero, an oversaturation with respect to the corresponding phase is indicated and precipitation can be expected. In principal, the SI is the log ratio of the ion activity product (IAP) and K_{sp}.

$$SI = \log_{10}\left(\frac{IAP}{K_{sp}}\right) \tag{13}$$

The solubility product determines the ion activities at geochemical equilibrium while the IAP describes the product of the ion activities as is. Accordingly, a geochemical equilibrium is reached when $IAP = K_{sp}$ and $SI = 0$. Consequently, an aqueous solution is oversaturated with respect to the given mineral phase if $SI > 0$ and undersaturated if $SI < 0$. At geochemical equilibrium reactions, the amount of solid phase alteration is the volume that is necessary for reaching an equilibrium.

In comparison to experiments, the major discrepancy of geochemical equilibrium models is the time interval reactants need to reach equilibrium. Thus, reaction rates have been determined experimentally for various mineral phases (e.g., Plummer et al., 1978). From the numerical perspective, reaction rates must be integrated over given time intervals while considering the effect of ongoing solution changes on the reaction rate (Parkhurst and Appelo, 1999). A general rate equation is given in Eq. (14) describing the concentration changes (Δc_i) of the aqueous species i. Therefore, the stoichiometric coefficient of species i in the kinetic reaction ($sc_{i,k}$) is multiplied by the specific reaction rate for phase k (r_k in mol/kgw·s):

$$\frac{\Delta c_i}{\Delta t} = sc_{i,k}\, r_k \tag{14}$$

An overall kinetic reaction rate (R_k) of mineral phases is given in Eq. (15) according to Appelo and Parkhurst (1999). It considers the specific reaction rate (r_k in mol/m^{2}s), the initial surface

area ($A_{s,0}$), the mass of solution (m in kgw) and a factor accounting for the continuous concentration changes during dissolution reactions. That factor considers the initial moles of the solid phase k ($moles_{k,0}$), the moles at a given time ($moles_k$) and an exponent (n) considering changes in the area to volume ratio during dissolution. For uniform dissolution of spheres and cubes: $n = {}^2/_3$ (Appelo and Parkhurst, 1999).

$$R_k = r_k \frac{A_{s,0}}{m} \left(\frac{moles_k}{moles_{k,0}} \right)^n \tag{15}$$

The Damköhler number (Da) is a measure relating the reaction rate to the mass transport rate. Eq. (16) calculates these rates as volume difference per second and as volumetric flow rate Q, which is the product of physical velocity and the cross-sectional Area (A). The Damköhler number is dimensionless and can be used for determining the dissolution regime. At $Da \ll 1$, the reactions are transport-controlled, at $Da \approx 1$, homogeneous dissolution can be observed throughout the structure and at $Da \gg 1$, pore alteration is increasingly controlled by reaction kinetics.

$$Da = \frac{Reaction\ rate}{Mass\ transport\ rate} = \frac{\Delta V_{phase} \Delta t^{-1}}{Q} = \frac{\Delta V_{phase}}{u \cdot A \cdot \Delta t} \tag{16}$$

2.5 Dissolution regimes

In continuum models, Maheshwari et al. (2013) make a distinction between three general dissolution regimes showing quite different visual patterns. They divide these from the ratio of convection to dispersion based on an acid injection rate and the resulting Damköhler number, which can be transferred to the ratio to at the pore scale. The dissolution regimes are shown in Fig. 4 for decreasing flow velocities. In consideration of reaction kinetics, uniform dissolution evolves at dominant advection (Fig. 4a) while wormholing is observed at similar advective and diffusive forces (Fig. 4b,c). Face dissolution develops at $Pe \ll 1$ (Fig. 4d). Accordingly, the Damköhler numbers increase from Fig. 4a to Fig. 4d. In the uniform dissolution regime, the inflowing fluid reacts rather homogeneously throughout the structure (Fig. 4a). Accordingly, the flow rate dominates the reaction rate implying a low Damköhler number. The dissolution is then controlled by surface reaction kinetics. In the wormholing regime, wormholes form especially at the inflow region. When advective and diffusive velocity are comparable, the

reactant tends towards bigger pores while reacting at pore throats extending these. However, only a few wormholes propagate (Fig. 4b). When diffusion slightly dominates the flow rate, the wormholing forms a canonical shape (Fig. 4c). At slow flows and thus high Damköhler numbers, a diffusion front develops as clearly visible in Fig. 4d. That regime is called face dissolution. Golfier et al. (2002) have found a similar relation of Péclet and Damköhler numbers to dissolution regimes, however at different values.

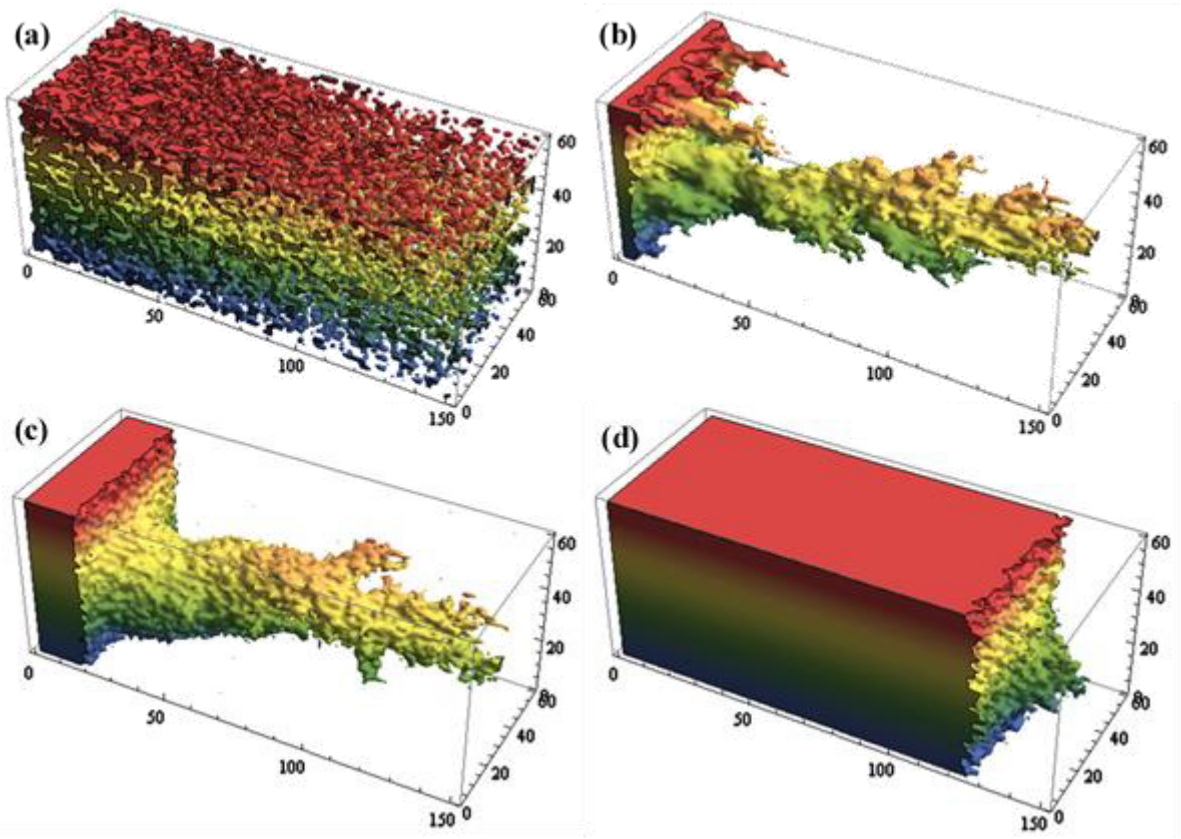

Fig. 4. Dissolution regimes (Maheshwari et al., 2013)
The images show (a) uniform dissolution at $Da = 1$, (b) wormholing regime at $Da = 200$, (c) conical wormhole regime at $Da = 2{,}000$ and (d) at $Da = 10{,}000$, face dissolution of carbonate rocks as obtained by acid injection simulations in a two-scale continuum model with injection rates decreasing from the first image to the latter. Spatial resolution is 3.5×1.4×1.4 cm at a mesh consisting of 150×60×60 grid cells (Maheshwari et al., 2013).

Menke et al. (2016) performed pore scale experiments with in-situ synchrotron measurements showing three types of dissolution regimes visualized in Fig. 5. Using Estaillades and Portland limestones for experiments, Menke et al. (2016) find a structure-dependency for the formation of dissolution regimes. With a higher porosity and at the same experimental setup according to reservoir conditions, the Estaillades limestone more likely shows uniform dissolution while the experiment with the Portland sample results in a new dissolution regime, which Menke et al. (2016) call the channeling formation.. Damköhler numbers are in the range of 10^{-4} to 10^{-5} and

thus do not represent the continuum scale assumptions. Nevertheless, varying acid injection rates in heterogeneous systems at the pore scale also result in different carbonate dissolution regimes, which however depend from the structure. Accordingly, the formation of dissolution regimes is not determined by certain Da and Pe numbers but by a relative relationship of advection, diffusion and reaction rate.

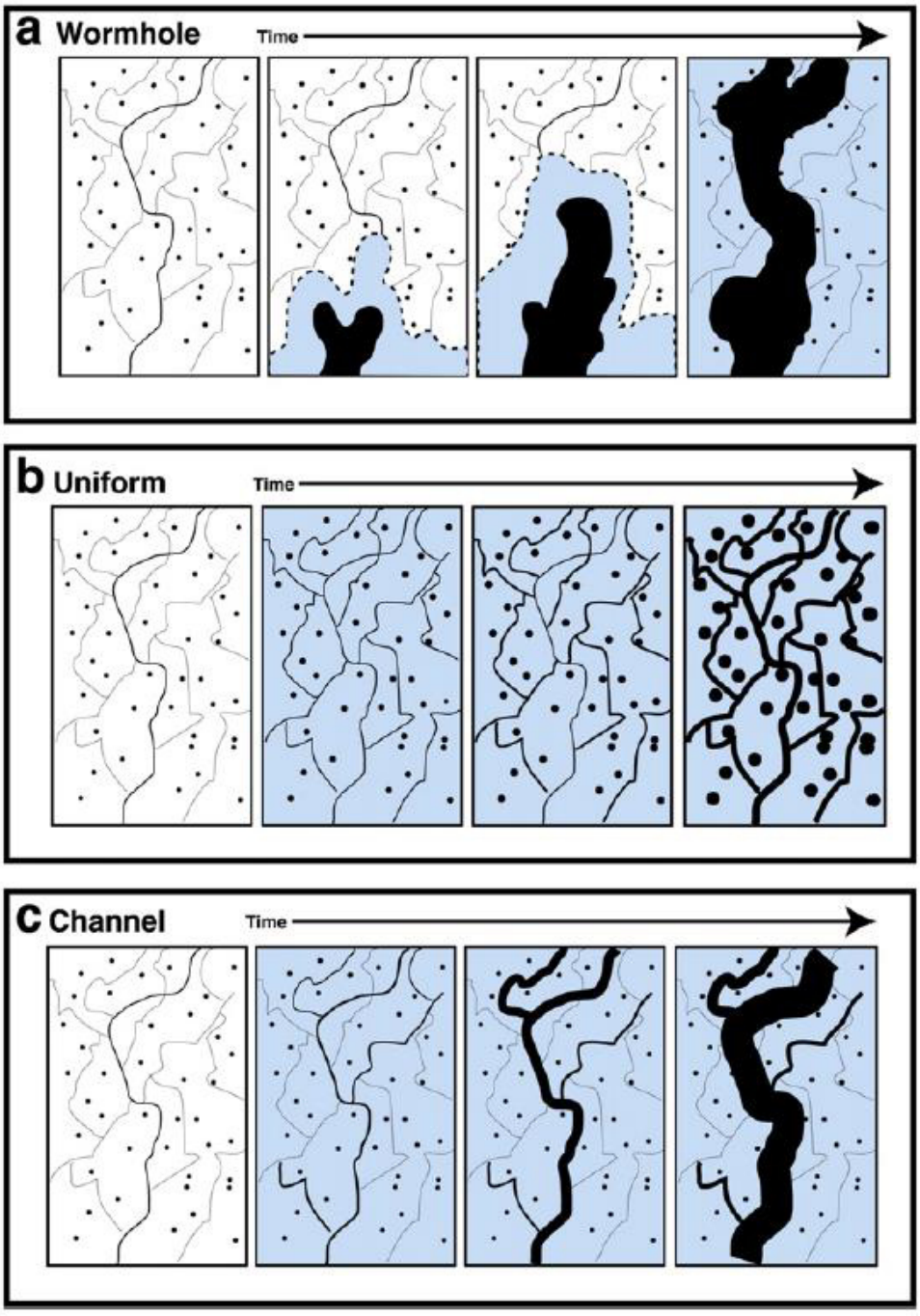

Fig. 5. Schematics of dissolution regimes (Menke et al., 2016)

The schematics represent the development of (a) wormholing, (b) uniform and (c) channel formation dissolution regimes (Menke et al., 2016).

2.6 Geochemical systems

In this work, simulation models and results are presented for three generally different geochemical systems. These are (1) celestite precipitation, (2) halite precipitation induced by calcite diffusion and (3) kinetic calcite dissolution.

Our geological pore scale research aims at aquiring time-resolved characteristics of a rock-fluid system developing due to coupled geochemical and physical reasons. Thus, the results are expected to vary for the different geochemical setups, initial structures and physical boundary conditions.

2.6.1 Celestite precipitation

As a first geochemical system, celestite ($SrSO_4$) precipitation has been chosen based on experimental results of Chagneau et al. (2015). The diffusion-controlled experimental setup and the fast precipitation kinetics of celestite render the experiment a potentially convenient benchmark study since flow field computations are not required while non-kinetic equilibrium reaction calculations can be performed.

In the experiment of Chagneau et al. (2015), a horizontally arranged sand column of 5 cm length and 1 cm diameter was connected to two reservoirs containing aqueous solutions at 0.5 M of (1) $NaSO_4$ and (2) $SrCl_2$ (Fig. 6). The column was filled with cleaned sand grains at diameters of 100-300 µm and purified water containing a background electrolyte of 1 mM NaCl (Chagneau et al., 2015). Nylon filters separate column and reservoir on either side. Near the center, a thin precipitation front developed clearly visible at day 7 of the experiment and reaching a steady state at day 15 (Fig. 6). The reservoir solutions were regularly renewed onto day 29. After an experimental time of 63 days in total, µCT measurements were performed (Chagneau et al., 2015).

When the SO_4^{2-} and Sr^{2+} ions approach each other, involved aqueous solutions equilibrate and precipitation is potentially possible:

$$Na_2SO_4 + SrCl_2 \rightarrow SrSO_4 + 2Na^+ + 2Cl^- \tag{17}$$

Considering the default PhreeqC database (Parkhurst and Appelo, 2013) and room conditions, the celestite saturation index ($SI_{Celestite}$) can be calculated at Eq. (18) by employing the celestite equilibrium constant ($K_{Celestite} = 10^{-6.66}$):

$$SI_{Celestite} = \log_{10}\left(\frac{\{Sr^{2+}\}\{O_4^{2-}\}}{10^{-6.66}}\right) \tag{18}$$

If Eq. (18) results in $SI_{Celestite} > 0$, an oversaturation with respect to the aqueous solution is given indicating precipitation.

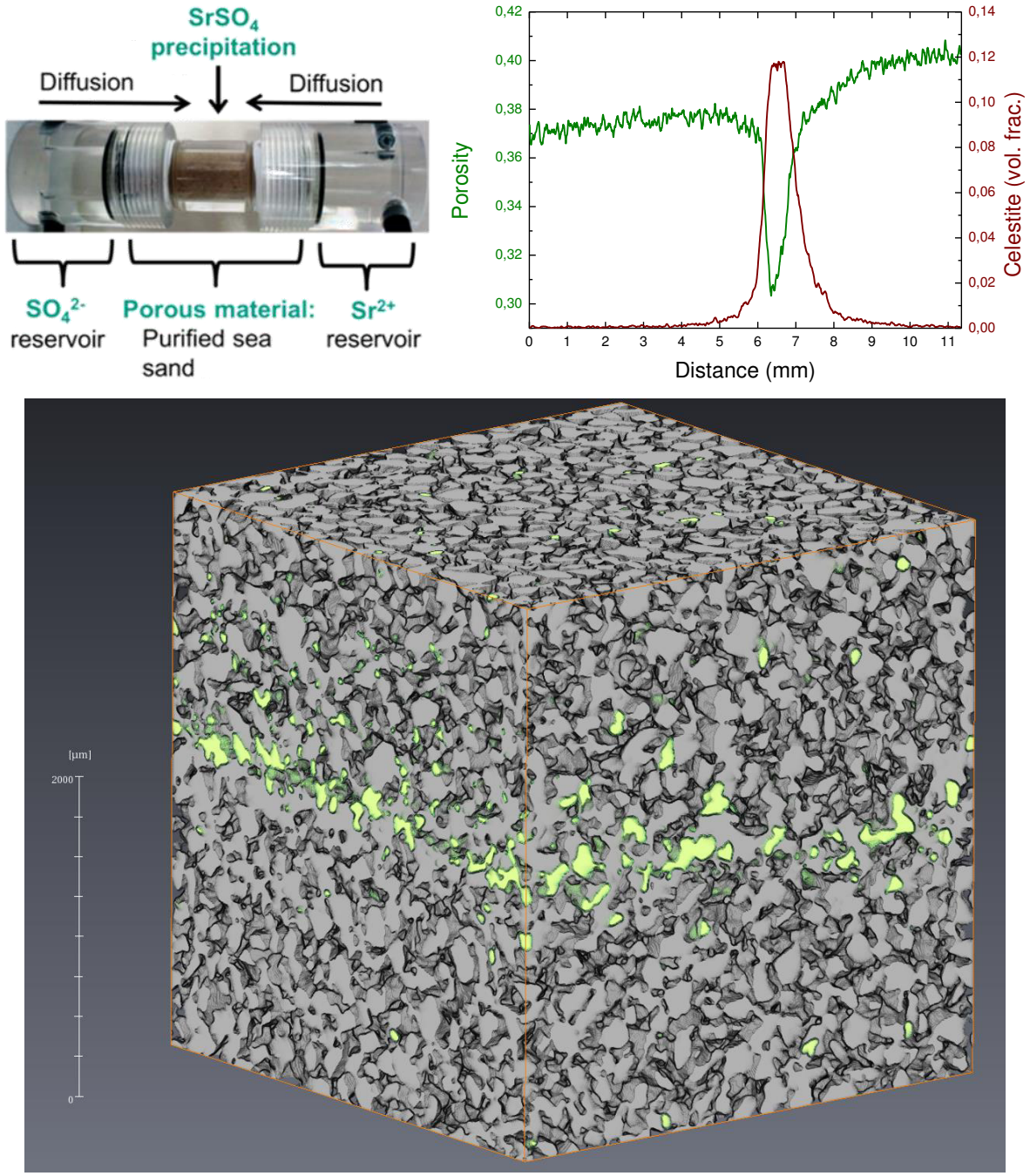

Fig. 6. Celestite precipitation experimental setup and results

The experimental setup inducing celestite precipitation (top left), the resulting horizontal distribution of pore space and celestite near the column center (top right) and the 3D image based on segmented µCT measurements (bottom) showing the celestite precipitation front in yellow color (Chagneau et al., 2015).

2.6.2 Halite precipitation and calcite dissolution

The second geochemical system was chosen in consideration of the HyINTEGER project. Halite (NaCl) precipitation is induced by calcite dissolutions that slightly increase the halite saturation index from an initial equilibrium to an oversaturation with respect to the aqueous solution. For reservoir conditions of 100 °C and 20 MPa, the mass-action equations for calcite and halite equilibrium are shown in Eq. (19) and (20). The solubility product of the according solid phases is related to the product of the activities (indicated with curly brackets) of the aqueous species. The equilibrium constant is extracted from PhreeqC calculations (Parkhurst and Appelo, 2013).

$$K_{Halite} = 10^{1.63} = \{Na^+\}\{Cl^-\} \tag{19}$$

$$K_{Calcite} = 10^{-9.09} = \{Ca^{2+}\}\{CO_3^{2-}\} \tag{20}$$

Salt precipitation is a well-known issue in near wellbore regions when e.g., CO_2 is injected (Ott et al., 2013). Such precipitations reduce the porosity and, subsequently, the formation permeability and the injection rate. The simulation of halite precipitation induced by inflow of aqueous fluids can also model the clogging of the pore space, although the applied simulation model does not consider gas injections. However, the reactive fluids model is generally capable of concerning initial solutions with the according gas partial pressures.

2.6.3 Kinetic calcite dissolution

In different structures, the solid calcite phase was dissolved in consideration of reaction kinetics. In order to determine the calcite reaction rate ($r_{calcite}$), the rate expression of Plummer et al. (1978) was applied:

$$r_{calcite} = \underbrace{k_1\{H^+\} + k_2\{CO_2\} + k_3\{H_2O\}}_{\text{forward rate } (r_f)} \underbrace{- k_4\{Ca^{2+}\}\{HCO_3^-\}}_{\text{backward rate } (r_b)} \tag{21}$$

The temperature-dependent kinetic dissolution rate constants of the forward rate (r_f) are $k_1 = 10^{0.198\,-\,444\,/\,T_K}$, $k_2 = 10^{2.84\,-\,2177\,/\,T_K}$, $k_3 = 10^{-5.86\,-\,317\,/\,T_K}$ for $T_K \leq 298.15\ K$ and $k_3 = 10^{-1.1\,-\,1737\,/\,T_K}$ for $T_K > 298.15\ K$. However, in the acidic pH range used within this thesis, only k_1 is of relevance according to the activities (indicated with curly brackets). The kinetic constant k_4 and the accompanying activities in Eq. (21) determine the calcite

precipitation and thus the backward rate (r_b). Parkhurst and Appelo (1999) approximate the HCO_3^- concentration to twice the Ca^{2+} concentration and are hence capable of simplifying r_b to Eq. (22):

$$r_b = k_4\{Ca^{2+}\}\{HCO_3^-\} \cong k_4 2\{Ca^{2+}\}^2 \tag{22}$$

At equilibrium, $r_{calcite} = r_f - r_b = 0$ and $\{Ca^{2+}\}$ is the activity at saturation $\{Ca^{2+}\}_s$. For a pure $Ca\text{-}CO_2$ system with a constant CO_2 pressure (p_{CO_2}), the ion activity product (IAP) is determined by Eq. (23) while the solubility product of calcite ($K_{calcite}$) is described by Eq. (24).

$$IAP_{calcite} = \frac{\{Ca^{2+}\}\{HCO_3^-\}^2}{p_{CO_2}} \approx 4\frac{\{Ca^{2+}\}^3}{p_{CO_2}} \tag{23}$$

$$K_{calcite} = 4\frac{\{Ca^{2+}\}_s^3}{p_{CO_2}} \tag{24}$$

The backward rate term of Eq. (21) can be simplified to Eq. (25) by considering Eq. (22) - (24):

$$r_b = -\left(r_f \times 10^{2/3\ SI_p}\right) \tag{25}$$

The saturation index of the calcite phase ($SI_{calcite}$) can be calculated according to Eq. (13). The factors surface area (A_s) and time step (Δt) are proportional to the change in calcite solid phase concentration ($\Delta c_{calcite}$) and are thus multiplied with the calcite reaction rate:

$$\Delta c_{calcite} = A_s * (k_1\{H^+\} + k_2\{CO_2\} + k_3\{H_2O\}) * \left(1 - 10^{2/3\ SI_{calcite}}\right) * \Delta t \tag{26}$$

However, Eq. (26) is limited to calcite-water systems at constant p_{CO_2}.

3 Methods

The code presented in this chapter is based on a basic workflow comprising the possibilities and the capability of this novel reactive fluid dynamics modeling approach (Fig. 7). This workflow was developed at a preceding master thesis that highlights the feasibility of this novel reactive fluid dynamics modeling approach.

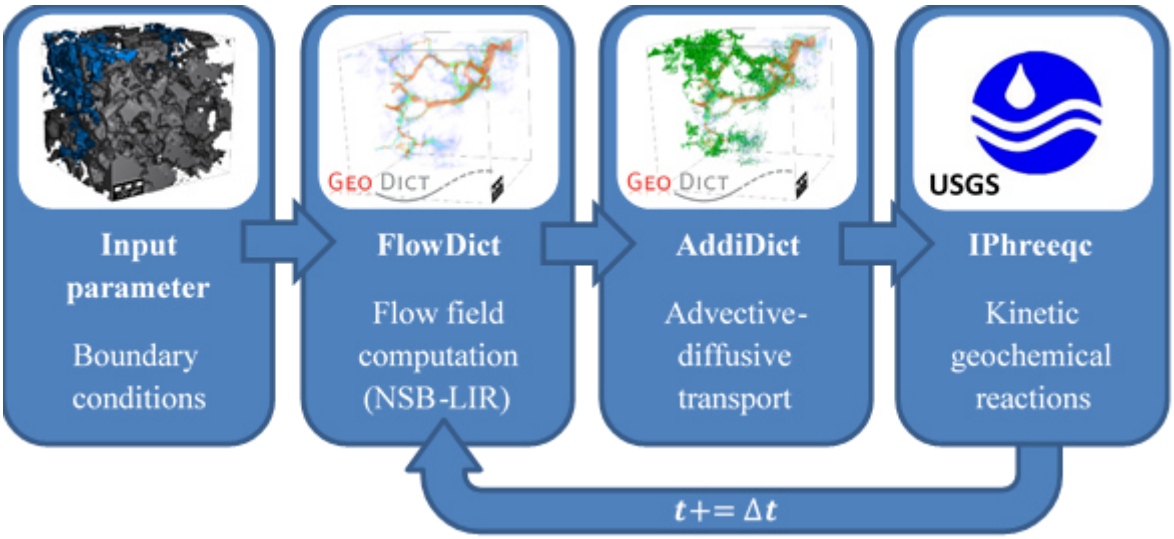

Fig. 7. ReacDict workflow

Depending on the input parameters, the three modules are run in sequential order until the final given time step is reached. The images show an example of a sandstone structure with visualized calcite pore cements and open pore space, according flow field and an exemplary particle distribution snapshot with flow direction from left to right during code execution. Visualizations were produced with GeoDict 2018.

A script was initially proposed using a Python-MATLAB interface as shown in Fig. 8. For performance reasons, that workflow has been realized in C++. Throughout this work, the code was parallelized and continuously extended based on requirements and preliminary simulation results. The code names *ReacDict*, which is the combination of *Reac*tion and pre*Dict*ion. ReacDict realizes reactive transport simulations by combining different software in an operator-splitting approach.

The development and the chosen benchmark studies partly aim at performing reactive flow simulations at reservoir conditions and, thus, at high P-T and high salinity. A second objective was to obtain a reasonable accuracy, which depends highly on the respective computational environment and the efficiency of the code. Thus, significant performance improvements were intended next to a high spatial and temporal resolution. A simple possibility for starting an individual simulation was planned coupled to the possibility of having a high influence on the

individual parameters. A text-based parameter file realizes this idea. All variables therein are briefly explained in the appendix.

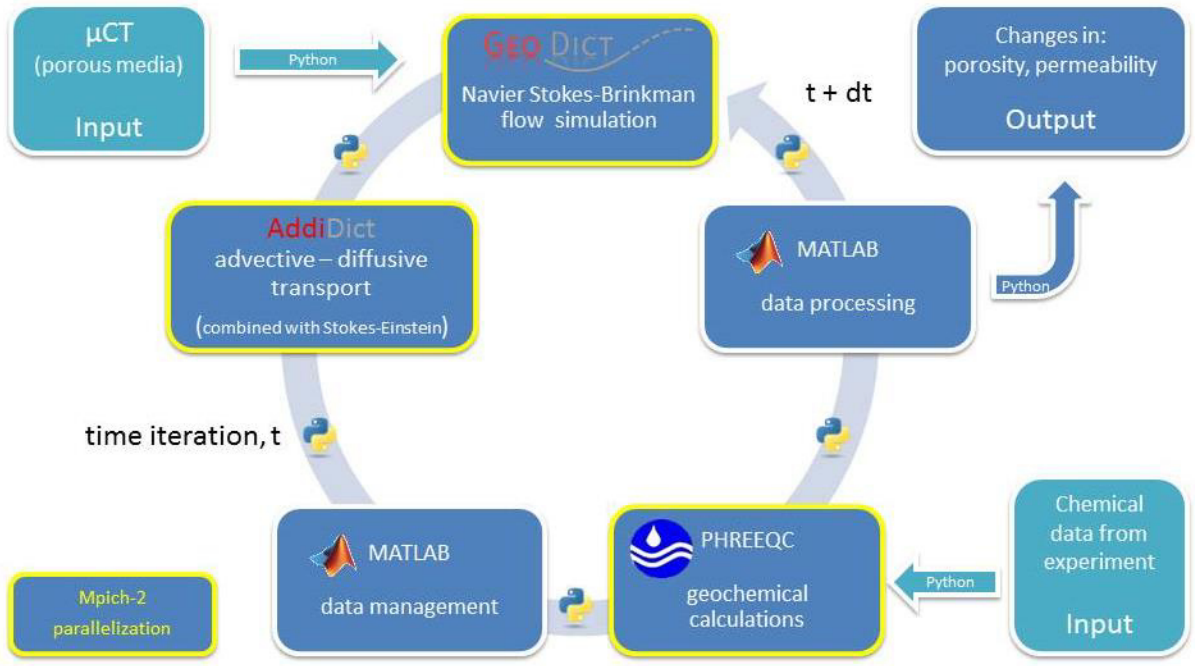

Fig. 8. Initially intended general workflow
This image comprises a general workflow of a preceding master thesis, which this work initially aimed at.

In general, ReacDict is capable of simulating flow, transport and reaction simultaneously at the pore scale. Based on dozens of individual user parameters, a virtual particle swarm flows through the binarized µCT-generated structure according to the computed flow field and the applied diffusion coefficient(s). These particles carry aqueous solutions that equilibrate with a pore fluid at the voxel scale. Resulting local disequilibria potentially induce dissolution and/or precipitation at reactive mineral surfaces. The geochemical equilibrium thermodynamics may be extended by reaction kinetics if available or added to PhreeqC databases. For simulations at increased time scales an alteration factor is provided to reduce computational time significantly. This factor increases the amount of dissolved and precipitated phases. The local and accordingly heterogeneous geometry changes induce a reactive porosity-permeability development potentially at REV size. Thus, based on individual data input, a wide variety of pore-scale hydrogeochemical systems may be simulated at high-performance computing (HPC) environments.

The simulations were mostly performed on a 32-core workstation (Kronos, University of Mainz) with 64 available threads and 512 GB RAM running Scientific Linux 6.7

(*https://www.scientificlinux.org*). The final simulation (model 4b) was executed on a more powerful system (Lapsus, University of Mainz) running CentOS 7 (*https://www.centos.org*). The integrated Dual Intel Xeon Platinum Gold 8160 Processors provide 96 threads in total. In general, Lapsus reaches a significantly increased performance with a total amount of 768 GB DDR4 RAM. The code is compiled with GCC version 4.8.5 employing C++14. The workstations allowed a significantly improved performance by employing the possibilities of code parallelization. Therefore, OpenMP and MPI-based approaches were applied with the open-source implementation Mpich-3 (*http://www.mpich.org*). ReacDict was tested in parallel with up to 48 threads. The presented code is scripted for execution on Linux operating systems (OS). For a portability to other OS, few code adjustments might be necessary.

3.1 GeoDict

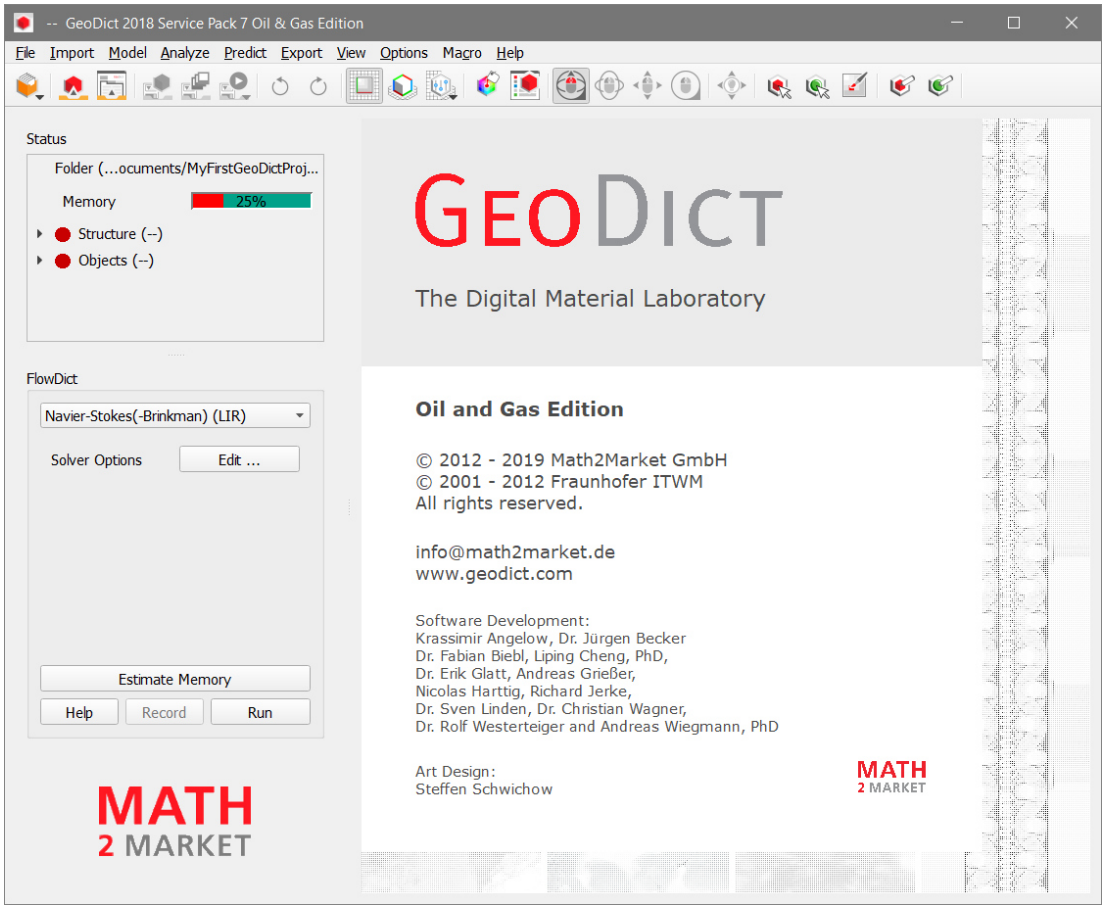

Fig. 9. GeoDict 2018 GUI

The figure shows the GUI of GeoDict 2018 in the Oil and Gas Edition. The modules can be accessed via the menu bar. Several symbols provide shortcuts to often used functions including an “Undo Processing” button. A status box offers an overview on available working memory, the working folder and the loaded components such as structure and volume field. The module section on the left shows that FlowDict was selected. The main part of the GUI is reserved for 2D and 3D visualization purposes.

The GeoDict software package was released in 2003 at the Fraunhofer ITWM (Kaiserslautern). Since 2011, it is distributed by Math2Market GmbH (Kaiserslautern, Germany). GeoDict is capable of importing and processing 3D images, designing new material structures, analyzing geometries, predicting material properties and behavior as well as advanced 3D visualization. In addition, the general user interface (GUI) of GeoDict (Fig. 9) is intuitive to use. Also, GeoDict supports the automation and optimization of individual workflows with various interfaces. This work exploits the advanced option of starting the solvers externally. The software offers highly efficient numerical solvers rendering GeoDict a very good choice for coupling a geochemical calculator and performing reactive transport simulations in µCT-generated structures.

3.1.1 Flow-solver

The flow fields are computed employing the FlowDict module of the GeoDict software package. The module is capable of computing incompressible, stationary Newtonian flows. At the voxel scale, it determines the velocity tensor iteratively. FlowDict predicts the physical mean flow velocity for a given pressure drop (Wiegmann et al., 2010) enabling the permeability calculation of a porous structure at the pore scale by applying Darcy's law shown in Eq. (2). FlowDict computations assume a steady flow regime whereby time-dependent phenomena such as turbulence are not taken into account.

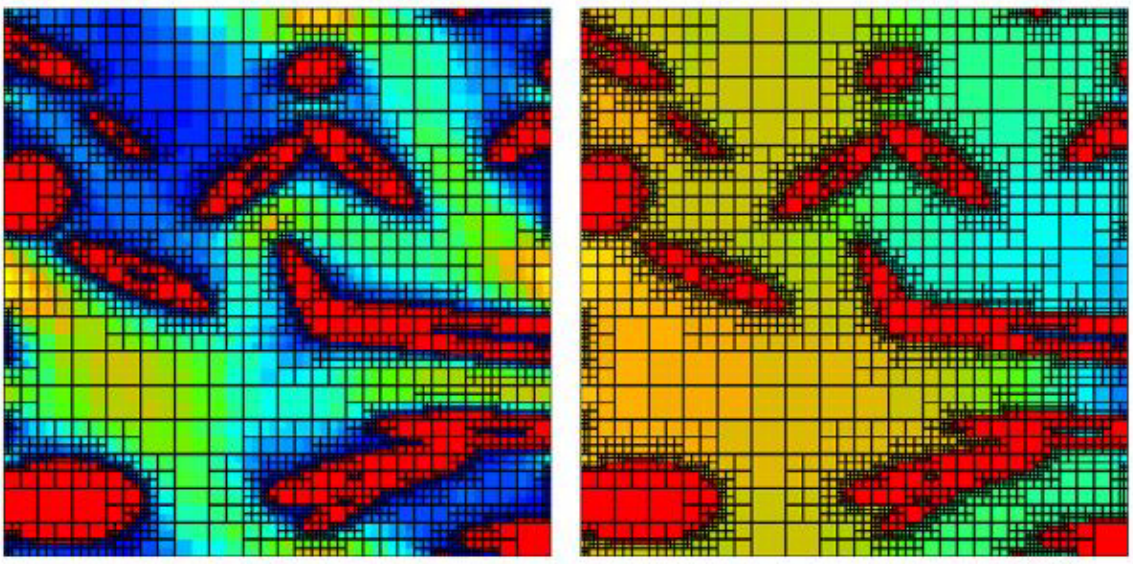

Fig. 10. LIR solver grid adaptions (Linden et al., 2015)
Solid material is shown in red color, the velocity (left) increases from blue to orange color. On the right, the pressure field is shown with a gradient decreasing from left to right (Linden et al., 2015).

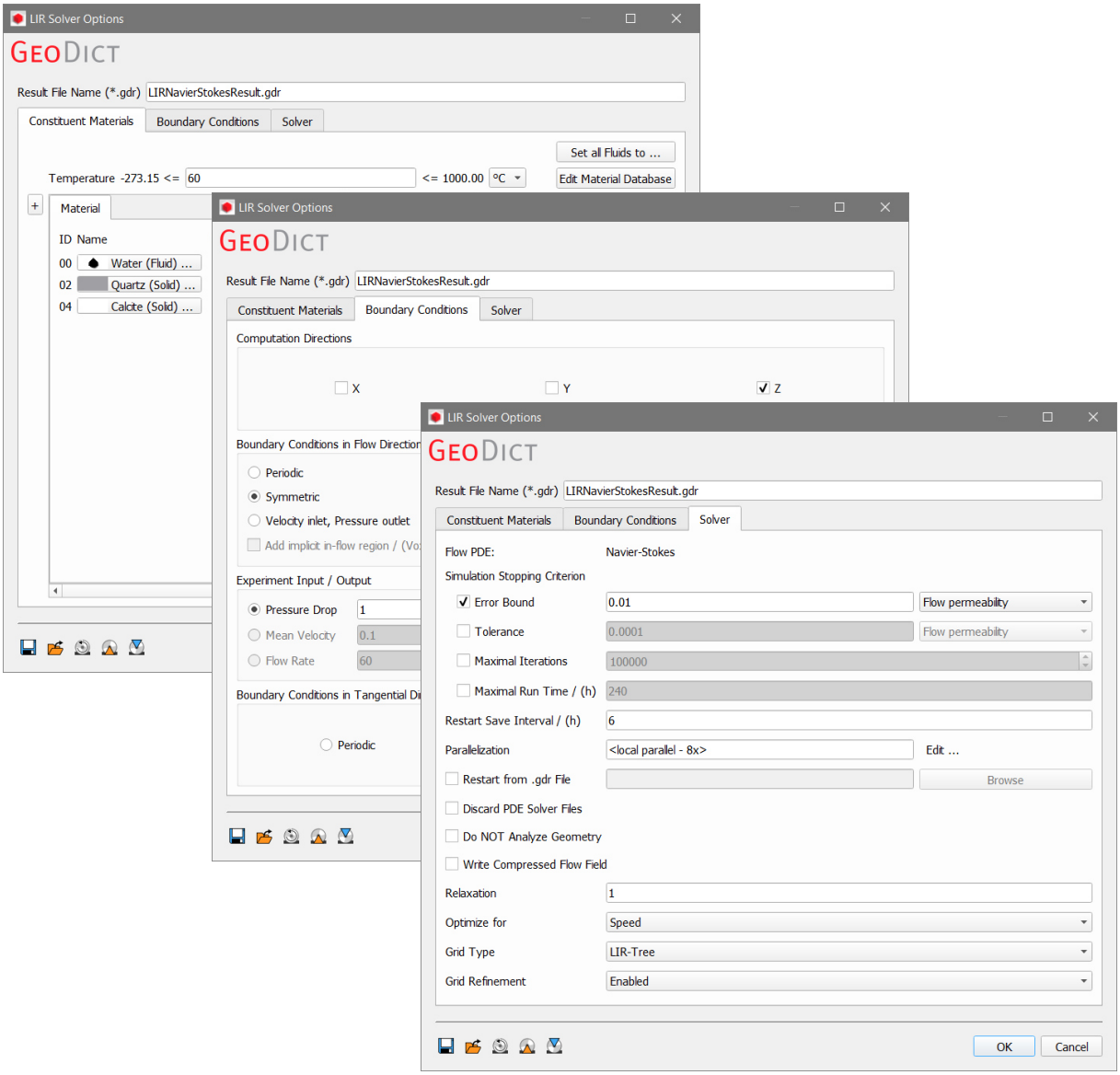

Fig. 11 FlowDict – LIR solver options

The LIR solver offers various properties that allow to adapt each flow simulation to individual needs. These options range from temperature-dependent fluid properties and boundary conditions to convergence settings and computational properties in order to account for the available hardware configuration.

For linear flows with empty, solid and porous voxels, the Stokes-Brinkman equation is applied to iterate the result with a given tolerance as convergence criterion. It is adequate for modeling laminar flow. Faster flows having a non-linear relation between pressure drop and mean velocity are described by adding the Navier term. Apart from the input parameters in the control file (*.pde*), the (Navier) Stokes-Brinkman solver needs a porous and permeable voxel-based structure file (*.gdt*) and a flow resistivity file (*.gfr*) for the Brinkman model. The input of local flow resistivity values allows the implementation of clogging phenomena at the sub-voxel resolution affecting the computed transport properties. For porous voxels a local permeability

is calculated based on the voxel-porosity and the chosen model: (1) a percentage from the global permeability of the previous time step, (2) application of the simplified cubic law described by Eq. (4), (3) consideration of the Kozeny-Carman equation given at Eq. (5). The flow resistivity is then the fluid viscosity divided by the local permeability.

The partial differential equations were solved with the LIR (Left-Identity-Right) solver. This method is appropriate for modeling linear (Linden et al., 2015) as well as non-linear fluid flow. The solver is capable of generating a tree representing a huge 3D voxel geometry with billions of voxels (Linden et al., 2014). The non-uniform adaptive grid (Fig. 10) has very low memory requirements. For highly porous materials, it is very fast compared to other solvers (Saxena et al., 2017). The properties for the LIR solver in FlowDict offer a suitable flexibility with minimum requirements in basic knowledge of fluid dynamics (Fig. 11).

Boundary conditions (BC) are an important choice as these can be crucial for the quality of simulations. A symmetrical boundary condition would be suggestive for modeling flow through low porosity structures. Flow through a tangentially enclosed structure would for example suggest choosing No-Slip as a secondary option. A list of recommendations for boundary conditions is given in Table 1. Therein periodic BCs are listed; they mean duplications of the ROI in the specified directions. This would suggest either an initial high porosity or the implementation of inflow and outflow region (inlet). However, inlets can significantly increase the runtime.

Table 1. Boundary conditions

This table shows recommendations for boundary conditions in GeoDict kindly provided by Dr. S. Linden (Math2Market). It relies on results from comparable experiments.

		Tangential boundary conditions		
		Periodic	Symmetric	No-Slip
Flow BC	Periodic	Highly porous and periodic structures	Symmetric flow fields and structures	Encased structures
	Periodic with inlet	Highly porous structures	Low porosity structures, Rocks	
	Symmetric	Low porous structures, Rocks	Low porosity structures, Rocks	

3.1.2 Particle transport modeling

Particle transport paths are simulated by the AddiDict module of the GeoDict software package. Time-dependent particle positions are obtained from *Trajectories.gpt* result files for calculating the (inflow) fluid migration at the geochemical workflow.

An insight on the AddiDict capabilities is given by a case study about nanoparticle migration (Glatt et al., 2015). AddiDict is capable of simulating mass transport by considering both advection and diffusion (see Fig. 3). Accordingly, the particle motion is the additive combination of Brownian motion as well as the flow field, which is stored by FlowDict in the *.vap* file containing local fluid velocities according to the flow direction. The module is capable of calculating particle diffusivities from given particle diameters and fluid characteristics by applying the Stokes-Einstein equation, which is decribed by Eq. (7). The presented ReacDict simulations use the option of infinitesimally small virtual particles that are given diffusion coefficients directly. Considering infinitesimally small particles, the diffusive motion is simulated applying a random walker combining Eq. (8) and the 3D Wiener measure ($d\vec{W}$) as a probability function closely related to the normal distribution:

$$\frac{dx}{dt} = \vec{u} + \sqrt{2D}\frac{d\vec{W}(t)}{dt} \tag{27}$$

In a voxel-based structure, a random particle distribution within a single specified volume is created. For ReacDict, particles can be created directly at the inflow plane or in a single cuboid limited by Z-axis values. The initial positions are stored in the GeoDict input file *TrackerInitialParticles.gpp*. In the *.gpt* output file, particle positions are stored at user-defined time intervals onto the maximum time according to the general time step. By default, particles are created at the inflow plane depending from the ratio of flow velocity to voxel length. In addition, a probability function is applied accounting for decimal values of this ratio. Fig. 12 shows an example for an initial particle distribution.

Particle interactions with solid voxels are controlled by selectable collision models. The "sieving" model was chosen to enable free particle motion. This approach does not allow particles to stick to the solid material unless they are connected to two solid voxels and do not move anymore. However, with particles at $\lim_{d\to 0} d$, particles never stick to solid voxels. In either case, a restitution parameter is set at *CollisionParameters*. By default, a restitution of 0.5

triggers a slowdown of particles by 50 % at each collision and thus, the particle energy reduces by 75 %.

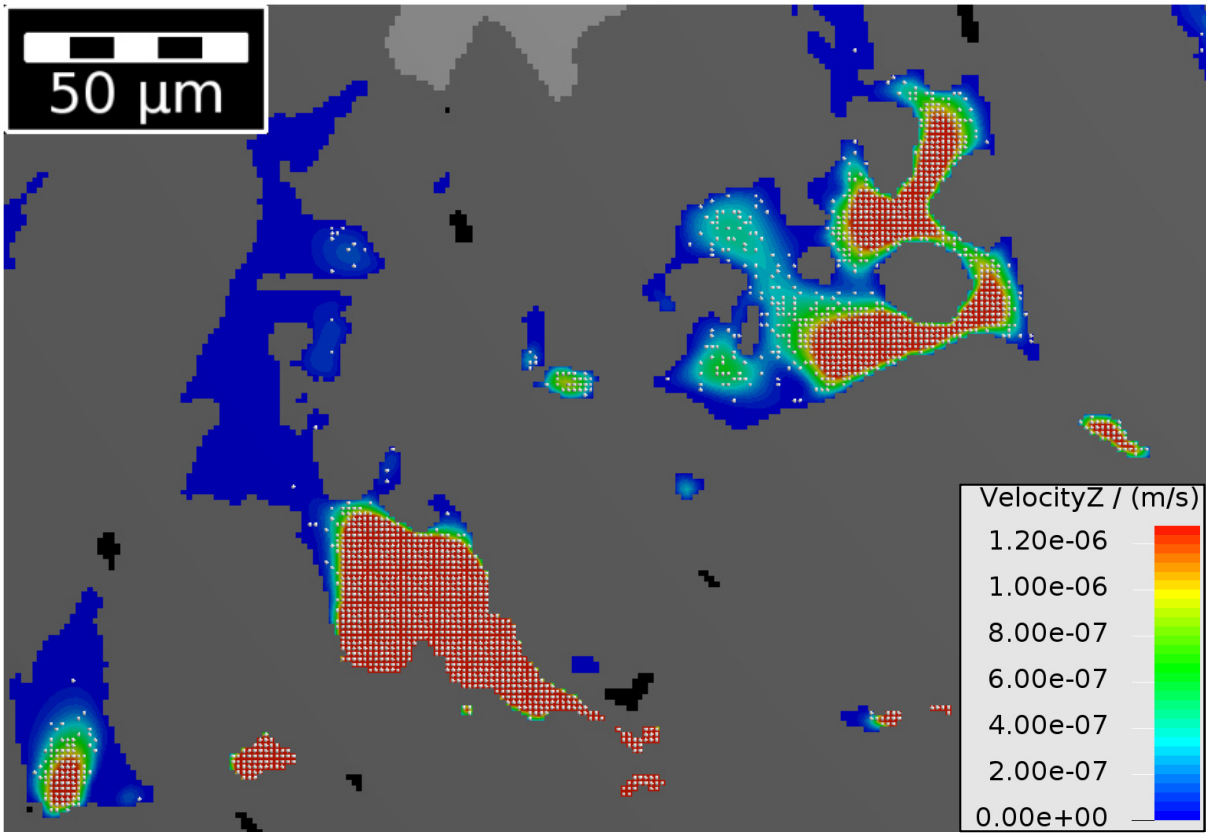

Fig. 12. Initial particle distribution based on the flow field

The 2D image shows inaccessible voxels (grey and black) and the flow velocities in the inflow plane of simulation model 4a and 4b. Particles are visualized as white points. In the pore space, the Z-axis velocity is shown in the range of up to one voxel length per second. Accordingly, red color indicates the mandatory creation of at least one particle per inflow voxel. For velocities below the maximum color bar value, particles are created at a probability decreasing linearly with local velocities.

The properties for the particle tracker range from intuitive basic settings to expert parameters (Fig. 13).

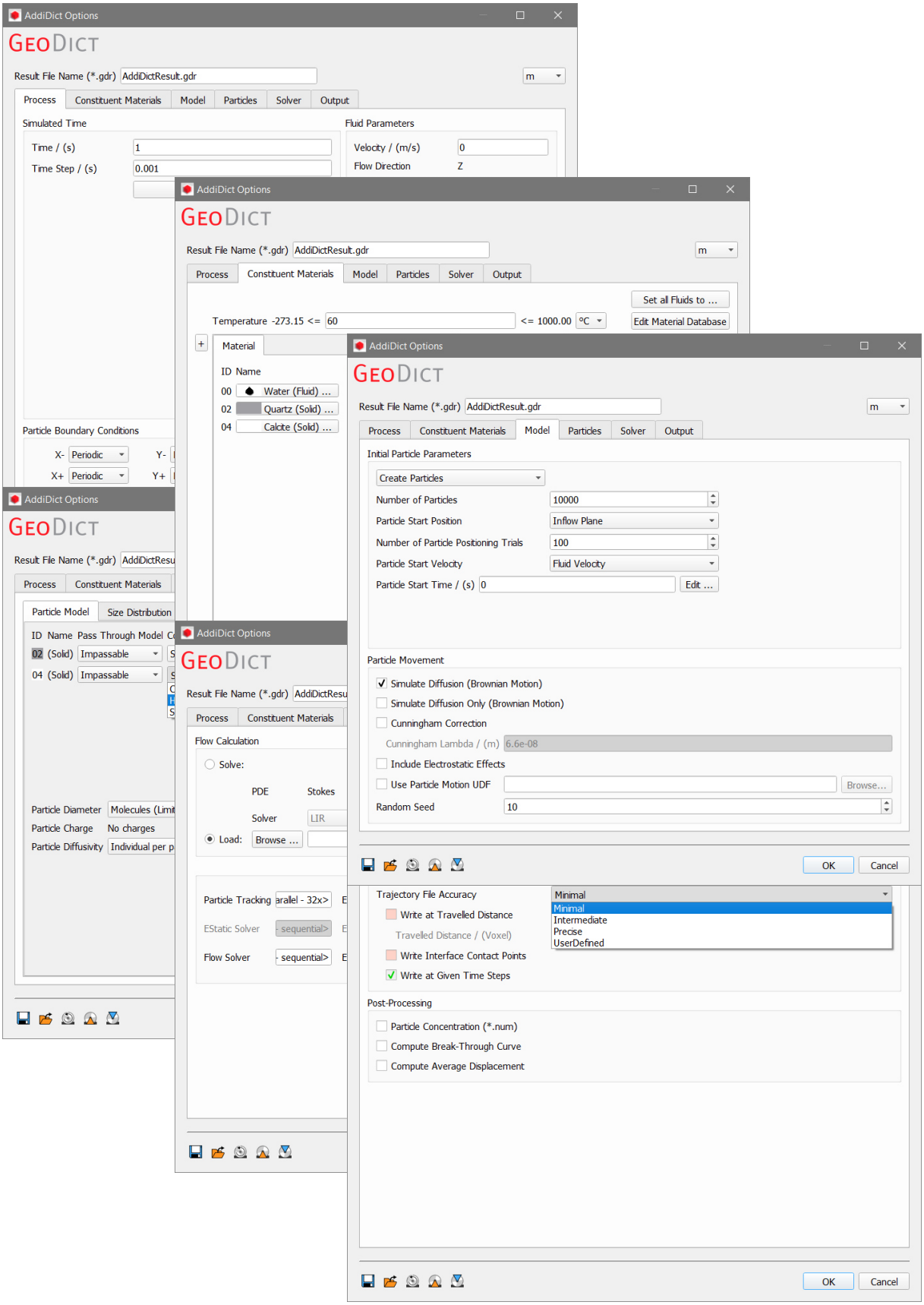

Fig. 13 AddiDict options

The particle tracker options window offers 6 main tabs with properties ranging from time, material and particle specifications to collision models, computational aspects, storage and post-processing options.

3.1.3 Synthetic dissolution

The approach of uniform material surface dissolution has the advantage of getting fast results concerning the porosity-permeability development. The concept of synthetic dissolution has been realized using a Python script that can be executed in the GeoDict GUI. The dilate function from the ProcessGeo module and FlowDict are repeatedly employed. Several parameters control the repeated global dissolution steps on grain surfaces. The grain boundaries can be dissolved in up to 4 steps. In order to set up partial dissolution, local permeability values are calculated in three different ways.

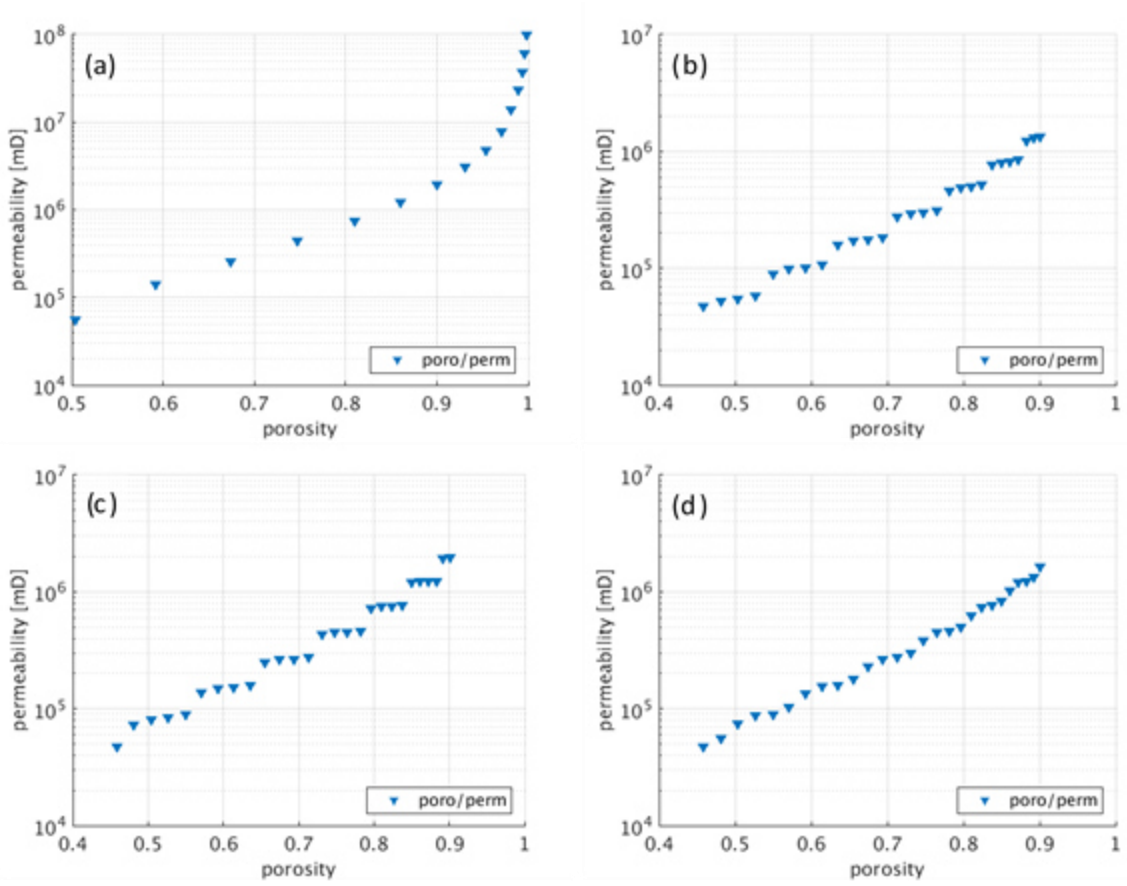

Fig. 14. Porosity-permeability plots, synthetic dissolution

Figure (a) shows the dissolution of full grain surfaces. For the other plots, 25% grain surface porosity reductions were applied with local permeability calculations based on (b) a percentage of the permeability, (c) cubic law and (d) the Kozeny-Carman equation.

However, this concept neither considers flow field and flow direction nor kinetic reactions. Although the approach is neither replacing a reactive flow experiment nor such a simulation, it is anyway capable of providing a first impression on the development of the hydromechanical transport parameters during uniform dissolution. Another advantage is the capability of testing approaches on local permeability calculations. This is shown in Fig. 14 based on the

homogeneously distributed grain matrix from the 128^3 structure presented in chapters 4.1 and 4.2. For this structure, the Kozeny-Carman equation provides best results compared to other approaches. The porosity-permeability diagrams suggest further improvements.

3.2 Geochemical calculations with PhreeqC

For (kinetic) geochemical equilibrium calculations, IPhreeqc (USGS, v3) is implemented. The open-source software code is the C++ library of PhreeqC (USGS) and capable of calculating saturation indices for a number of species depending on the input solution and the chosen database (Parkhurst and Appelo, 2013). IPhreeqc is well known for the capabilities in modeling reactive transport (e.g., Nardi et al., 2014). Several databases exist for different application purposes. Every database offers a specific set of elements and phases for a range of P-T conditions. The CEMDATA database (Lothenbach et al., 2019) provides thermodynamic data for hydrated Portland cements in the system CaO-Al_2O_3-SiO_2-$CaSO_4$-$CaCO_3$-Fe_2O_3-MgO-H_2O. The Pitzer database of Appelo (2015) improves thermodynamic data for precipitations in deep wellbore regions. It considers temperatures up to 200 °C, high pressures and salinities in the Na-K-Mg-Ca-Ba-Cl-CO_2-HCO_3-SO_4-H_4SiO_4 system. However, kinetic reactions are typically not considered at such specialized databases and would thus require manual adjustments based on experimental results.

In ReacDict, particles act as containers carrying aqueous solutions including values for pH, temperature, pressure, element concentrations. Kinetically reacting systems also consider the redox sensitivity, which is considered by the pe value. By default, PhreeqC uses O_2 in order to calculate the pe, which is in turn used to determine the distribution of species of redox elements. In flow-through simulations, particles are continuously created at the inflow plane carrying a given inflow solution. These solutions equilibrate along the flow path with the pore fluid at the voxel scale. A user-defined pore fluid is initially given being in equilibrium with the existing reactive mineral phases. These equilibrations are performed employing the MIX command of PhreeqC. The local pore fluid and the according container solution are changed according to IPhreeqc results. The pore fluid continuously approaches the inflow solution with a gradient from inflow to outflow area. At solid surfaces, reactions are performed by employing the EQUILIBRIUM_PHASES or KINETICS keywords as chosen by the user. However, given mineral phases have to be described by a PHASES data block in the chosen database and, for kinetic reactions, a mineral-specific kinetic RATES data block is required along additional

parameters handed over by ReacDict such as specific surface area. Reactions may result in partial dissolution or precipitation of mineral phases.

For calcite, the PHASES data block in the default database (*phreeqc.dat*) is shown in Table 2. It is used to calculate the saturation index (SI) for solid phases in aqueous solutions and the amount of dissolved or precipitated phase to reach a specified SI (if possible). However, the current version of ReacDict automatically determines these calculations for an SI of zero.

Table 2. PhreeqC PHASES data block for Calcite
Descriptions in the mostly applied default database *phreeqc.dat* (Parkhurst and Appelo, 2013).

Lines	**Description**
Calcite	Phase name
CaCO3 = CO3-2 + Ca+2	Dissolution reaction
-log_k -8.48	Log solubility at 25 °C
-delta_h -2.297 kcal	Enthalpy of reaction at 25 °C
-analytic -171.9065 -0.077993 2839.319 71.595	A_1-A_4 for calculating the temperature dependence of K
-Vm 36.9 cm3/mol	Molar volume (molecular weight / density at 25 °C)

The temperature (T) dependence of the thermodynamic solubility product (K_{sp}) is calculated based on the values in the analytical expression ($A_{1\text{-}6}$; Table 2); undefined parameters are set to zero (Parkhurst and Appelo, 2013):

$$\log_{10} K_{sp} = A_1 + A_2 T + \frac{A_3}{T} + A_4 \log_{10} T + \frac{A_5}{T^2} + A_6 T^2 \tag{28}$$

In addition, PhreeqC calculates the pressure dependence of log K_{sp} (Parkhurst and Appelo, 1999) by considering the volume change of the reaction (ΔV_r), T in Kelvin, the gas constant (R) and the pressure (p) in atm:

$$\log K_{sp}(p) = \log K_{sp}(p = 1) - \frac{\Delta V_r}{2.303 \times RT}(p - 1) \tag{29}$$

PhreeqC models the equilibrium between an aqueous phase and a pure phase by employing heterogeneous mass-action equations (Parkhurst and Appelo, 1999) according to Eq. (12). The equilibrium is thereby identical to the minimum Gibbs energy for the system (Parkhurst and Appelo, 2013). Considering the phase-specific saturation index at equilibrium ($SI = 0$), PhreeqC uses Eq. (30) for determining the phase equilibrium ($f_{phase\ eq}$) in the numerical method (Parkhurst and Appelo, 1999). Therefore, the master species concentrations (c_m) and activities ($\{m\}$) and also the phase solubility constant (K_{sp}) are used:

$$f_{phase\ eq} = \left(\ln K_{sp} - \sum_{m}^{M_{aq}} {}_{m} \ln\{m\}\right) \tag{30}$$

For Eq. (26), PhreeqC calculates the surface area (A_s) via input of a specific surface area (SSA) and the initial amount of solid moles. In ReacDict, the SSA is calculated as the product of the voxel surface area (VSA), the user-defined global surface roughness factor ($f_{roughness}$) and the ratio of the number of dissolvable voxels to the dissolvable moles. According to Eq. (31), this ratio normalizes the available solid mass in order to set the SSA to a rough surface area with a maximum amount of reactive phase volume. The number of dissolvable voxels is up to seven since adjacent voxels are also concerned. The dissolvable moles limits the amount of the dissolvable phase volume and hence, the calcite kinetics of the PhreeqC default database can be applied without implementing any changes.

$$SSA = VSA \times f_{roughness} \times \frac{\#voxels_{dissolvable}}{moles_{dissolvable}} \tag{31}$$

For kinetic calcite dissolution, the final code uses a different approach. The calcite RATES data block has been adjusted to process more input parameters: (1) The surface area, (2) the alteration factor and (3) the maximum amount of moles that can be precipitated in the corresponding voxel. The alteration factor is used to calculate a maximum dissolvable amount of moles, which are not interfering with that factor when processing the geochemical results. This approach improves the numerical stability by limiting the voxel solid fractions to the range 0-1. For using different RATES blocks, these additional adjustments are recommended. The adjusted calcite RATES data block is available in the appendix. Unconventional RATES data blocks might require a few code adjustments.

The molar volume changes of the reactive species are passed to ReacDict to calculate the corresponding voxel fractions. The alteration factor is applied on that fraction before it is added or subtracted from the corresponding voxel. If there is no reactive mineral phase to dissolve at the respective voxel, the adjacent voxels are used for a homogeneously distributed pore alteration. When the phase changes could be processed completely, the solutions are also updated. In case of kinetic reactions, a separate Boolean data matrix is employed to consider persistent disequilibria at a local voxel. Accordingly, PhreeqC calculations are not only performed at particle positions but also at each voxel in disequilibrium. Thus, the runtime of the geochemical workflow is increased, which is another reason for the importance of using multiple threads. For the MPI parallelization, any phase fraction and solution alterations of

voxels in halo areas are temporarily stored and collectively communicated to the according threads. Solution changes of the virtual solution blobs are first gathered and then broadcasted to all threads.

3.3 Program code

The C++ code was developed continuously for three years. Code execution is controlled by various parameters providing the user with a suitable degree of freedom for setting up individual reactive transport scenarios. In order to understand the full range of code capabilities, the explanations below help to prepare a simulation as expected. In addition, an overview on the workflow and output during execution is given in order to be able to follow the running code status messages and make proper use of produced data for post-processing purposes.

3.3.1 Input data

Slightly more than 100 parameters are adjustable by the user in order to run a simulation. Various options allow a wide range of different geochemical systems, time scales and structures. This subchapter explains the most important parameters and describes important relationships between these. A full list including all available parameters is given with explanations in the appendix.

A project directory (*Directory*) and file naming standard (*FileNaming*) has to be set along with other file paths to executables including GeoDict solvers (*AddiDictExecutable*, *FlowDictExecutable*). Several input files are necessary: a GeoDict geometry (*PresetGDT*), an initial particle tracker file (*PresetGPP*), a flow resistivity file (*PresetGFR*), a flow file (*PresetVAP*) and an according GeoDict license file name (*AD.LicenseFileName*). Accordingly, before starting ReacDict, a structure has to be imported to GeoDict and saved as compressed *.gdt* file. From that structure a flow field computation needs to be started including the Brinkman solver to obtain a flow resistivity file next to the flow file, which however requires the definition of porous voxels or microporous materials. Then a particle transport simulation needs to be started. From the *.gpp* and *.gfr* files, the header files are needed for file preparation according to the simulation data.

In general, a time step has to be chosen, which controls the amount of FlowDict and AddiDict executions (*TimeStepInSec*). A maximum number of time steps describes a stopping condition

for ReacDict (*NumberOfTimeSteps*). This parameter can be increased later by restarting the simulation at any given time step, but, however, the number of digits is limited to the first definition. Thus, it is reasonable to set this stopping criterion initially to a higher value. Anyway, ReacDict can be stopped at any time by terminating the process without losing data. Stopping the running program may be achieved by pressing *Ctrl+C* in the executing terminal window or by closing it. For a restart, the *begin* parameter can be adjusted or optionally the ReacDict execution parameters can be used (see *below*). To control the amount of stored data, the number of directories, which are kept directly (*KeepDir*) need to be set along with the possibility to store full time step directories each X seconds (*Saveruns_Xs*). The version of GeoDict is given as year number at *GeoDictRelease* (e.g., 2018). ReacDict was performed on several versions each requiring code adaptions concerning the interfaces to GeoDict. However, the most actual version is not guaranteed to run on any other release than the 2018 version. This is due to continuous changes on GeoDict control files and data storage characteristics at the annual version releases. For performance reasons, the parallelization is improved by redistributing the data periodically at the beginning of the geochemical workflow. The parameter DataDistributionEveryXdt determines the frequency of these adaptions regarding the positioning of new particles at the inflow region.

In order to increase the frequency of FlowDict initializations, the parameter *FlowDictEachTimestep* may be set to *true*. The calculation of the local flow resistivity by *KozenyCarman* may also be changed to *true*. By default, ReacDict starts with a given flow field and initializes FlowDict only if the structure has been altered previously. ReacDict initializes FlowDict at the first (or restarted) time step with the parameter *StructureChanged* set to *true*. For the flow computations, a restart file is used to significantly reduce the computational time. However, restarting at every time step requires experience and knowledge at setting proper convergence criterions. Thus, the *.vap* restart file is stored directly at the project directory and only updated if the requirement of the *UpdateRestartFileAfterFDruntime* is met. Updating the restart file whenever FlowDict execution time reached 600 s has shown to be a good way to minimize irregularities in the permeability development due to unfavorable convergence parameters. For pure diffusion simulations, *FlowDict* may be set to *false*.

For the particle handling in ReacDict, several parameters are adjustable. For maximum performance, the default parameters are recommended, so that no parameters need to be set in the parameters file. By default, new particles are created based on the flow field in flow

direction at the inflow plane (*NewParticlesBasedOnFlow true*). Particles will be combined, whenever they are at the same voxel and the same time (*CombineParticles true*). This includes the possibility of creating particles initially representing multiple particles depending from the local flow velocity. For further runtime improvements, particles may be created representing X^2 inflow voxels (*SkipVoxel X*). If particles are not combined after being created, the parameter *CombineParticlesOnlyInitial* can be used to prevent further particle summation. During early code development, homogeneous particle distributions were coded. This option is still available and offers the possibility to set both the number of inflow particles per time step (*n_interacting*) and the possibility to limit the number of active particles (*MaxNumberOfParticles*).

Pure diffusion scenarios were performed with GeoDict 2017 and have not been tested with GeoDict 2018. These scenarios make use of a fixed set of particles (*n_interacting*), which diffuse through the structure and equilibrate within reservoirs. To set up diffusion reservoirs, the *ZReservoirVector* parameter has to be used as described in the appendix. In addition, *AD.BoundaryConditions.ZPlus* has to be set to *Reflective* for keeping particles within the structure. However, before the reflective boundary option was available within GeoDict, non-reactive barriers had to be created in order to keep the particles within the structure (*InflowParticleBarrier* and *InflowBarrierMaterial*).

For the geochemical workflow, an alteration factor can be chosen. The choice of this parameter is crucial, since it might interfere with the general time step. ReacDict limits the amount of dissolved species, so that the data is numerically correct. However, errors may approach and increase with reaction time due to an increasing amount of necessarily neglected phase reactivity. Thus, it is up to the user to find a proper setting to limit pore alteration especially when kinetic reactions are applied. It is recommended to perform a pre-examination by employing PhreeqC. In addition, an interval for the geochemical calculations has to be set (*GeochemTimestep*). Pore equilibrations and reactions are typically performed at time intervals below the general time step. The interval needs to be a natural multiple of the AddiDict time step (*AD.Trajectories.TimeStep*) at which the transport steps are calculated and stored. It should be chosen taking into account the ratio of particle velocity to voxel length. With a slow interval, the overall performance increases while the accuracy decreases. Possibly, the outflow voxels get comparably less particle positions resulting in a minor reactivity and, consequently, in a lower permeability as expected from the remaining structure. Reactive material phases have to be defined (*MaterialPhases*), which are considered at each reaction calculation. These phases

require additional information (e.g., *Calcite.MaterialNumber*); variables beneath the material number are shown in the appendix. Finally, non-reactive material phases are defined by applying the *OtherMaterial* parameter. The aqueous inflow and pore fluid solutions are specified with keywords (e.g., *InflowSolution.1.pH* or *PoreFluidSolution.1.Ca*). For pore fluids, cuboids with different initial solutions may be described by using the *PoreFluidSolution.1.areaXXYYZZ* parameter for given solutions numbered in ascending order. A constant pressure may be passed in *atm* using *PhreeqcPressure*. Additional 3D data output for aqueous species (e.g., HCO_3^-) may be set by employing *TrackSpecies* whereby names must be entered according to PhreeqC species naming.

GeoDict control files are created from both ReacDict default and user parameters. In order to set up FlowDict and AddiDict, the parameters file allows for a lot of adjustments. FlowDict offers several solvers, but only the LIR solver is available in the ReacDict environment. It may be chosen to solve the NSB or SB equation.

3.3.2 Code output

The ReacDict processes create log files and constantly update these with actual information of the code execution. If set to *true*, the *DebugMessages* parameter significantly increases the amount of output, which might be useful for debugging new code lines and finding reasons for unexpected behavior of the reactive system.

The output is generally classified as status, info, debug or error message. Status messages describe the processes ReacDict is executing. During the geochemical workflow, status messages also provide information about the progress, updated at the end of each calculation interval. Info messages give insight on the execution times of various time-consuming steps. At the end of the geochemical workflow, a general summary is supported concerning the geochemical system. Such a message might look like:

[INFO] Geochemistry after 100 timesteps at 10 s: 4.40764e+06 IPhreeqc-calls (noAlteration: 92 %; mixOnly: 64 %; PoreFluidOnly: 5 %; prec: 5 %; diss: 3 %). Total structure alteration: -2.3e+03 voxel. Total Alteration Error: 3e+01 voxel. Total Dissolution: 16283, Precipitations: 0, Errors: 0. Runtime Geochemistry: 53.60 s; MPI efficiency: 67.8 %.

Debug messages show various information, that is mainly thread-depending. It is recommended to leave this parameter at default (*false*), since strongly increased output may result in log files

with hundreds of MB. Several error messages are prepared to inform the user if something went wrong during ReacDict execution. For example, they will appear if a file is missing.

ReacDict writes a reduced amount of output to the terminal window for providing information on the steps ReacDict is actually processing. The ReacDict terminal output mainly concerns status and info messages. During execution of GeoDict modules, the terminal window exclusively displays according GeoDict information, also providing insight on the progress of the respective module.

Generally, ReacDict reads data files from AddiDict and FlowDict iterations, calculates modifications and, subsequently, writes new GeoDict-files for following time steps. In order to execute the algorithm, the GeoDict modules require both a control file (*.pde*) and a compressed GeoDict structure file (*.gdt*). Either of these modules create a log file. In addition, FlowDict is passed a flow resistivity file (*.gfr*) for computing the flow field tensors and the pressure field (*.vap*) and, thus, for storing four values for each voxel. A results text file is created containing resulting values for permeability, physical velocity and the accuracy. All of these files are stored in a specific directory, one for each time step. The same is true for the ReacDict summary text file to simplify post-processing. The summary file contains values for total runtime and porosity as well as statistics for the geochemical workflow. AddiDict requires an initial particle distribution (*TrackInitialParticles.gpp*) that is created based on the header of the *PresetGPP* file, the user parameters and the final particle positions of the previous run (*TrackerFinalParticles.gpp*). The resulting particle paths are stored in *Trajectories.gpt* containing values for each particle concerning particle ID, type, position, time and status. For the geochemical workflow, additional data files are created. The transported aqueous solutions are stored in *Solutions.rd* while the pore fluid is written to *VoxelSolution.rd*. The voxel fractions of reactive phases are stored in *phases.rd*. Additional geochemical data may be found in the automatically created *pCO2.rd* and the individual *TrackMolality1d.rd*. Voxels in geochemical disequilibrium concerning kinetic mineral phases are tracked at *KinPoreFluidReac1d.rd*.

3.3.3 Code development

The code has been developed based on a prototype version (Fig. 15). It has been continuously adapted to fit the needs of performed simulations. In addition, during three years of development time, various GeoDict versions were used, each with its own set of necessities

concerning code adjustments. Thus, the various interfaces between ReacDict and GeoDict were adjusted periodically to suit the requirements of new GeoDict versions usually released in autumn.

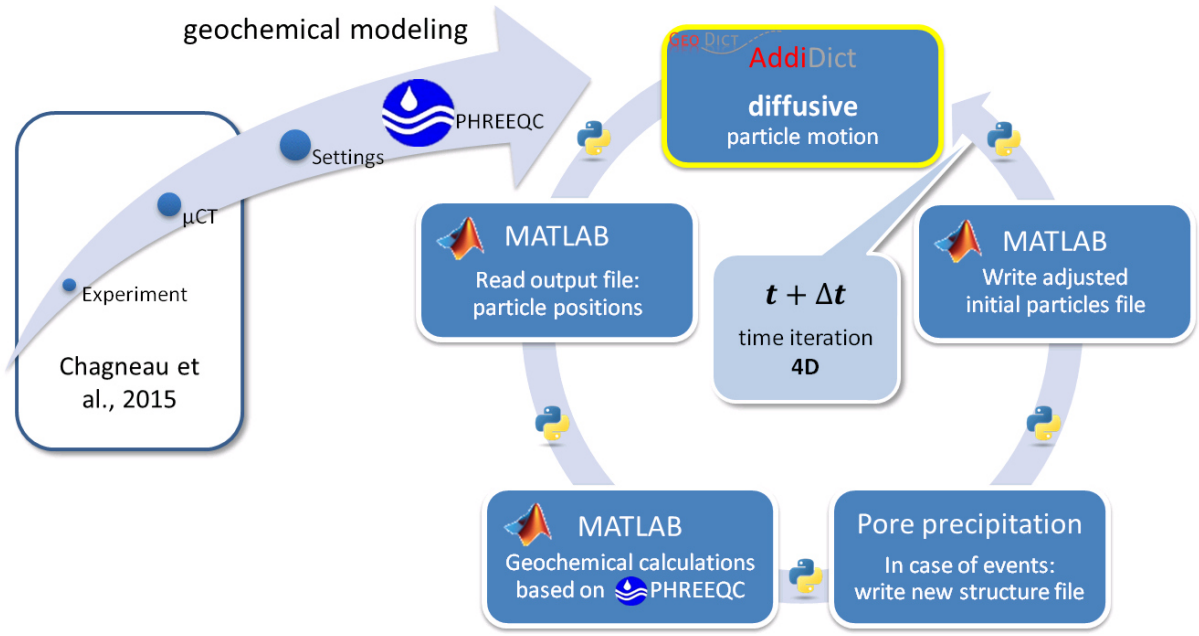

Fig. 15. Prototype workflow for celestite precipitation
This image summarizes the prototype model for simulating the experiment performed by Chagneau et al. (2015).

For performance reasons, the aforementioned prototype (Fig. 15) was coded in C++ and then extended according to the model presented in Fig. 8. The first simulations aimed at celestite ($SrSO_4$) precipitation following the experiments that were performed by Chagneau et al. (2015). In principal, any increase in temporal and spatial resolution requires higher system specifications in order to maintain the computational time. Therefore, as a first approach, an OpenMP (Open Multi-Processing) parallelization was implemented for geochemical calculations, which is applicable due to the available shared memory environment. However, the performance speed-up was limited to a factor of four for the parallelized parts. Thus, with a higher workload, a more promising parallelization routine was scripted using MPICH, a high-performance implementation of the Message Passing Interface (MPI) standard supporting the MPI-3 standard (*www.mpich.org*). Reactions were performed only at voxels hosting multiple particles and, thus, no pore fluid was considered at these simulations. However, these simulations showed celestite precipitation in the pore space without connection to solid surfaces. As a consequence, additional (optional) conditions were implemented into the code, so that precipitation can be limited to appear exclusively at solid surfaces. The development of

the porosity-permeability relationship could be obtained for that approach, but a realistic temporal relationship was not given. Therefore, both geochemical boundary conditions that are more comparable to the cm-scale of the experiment and the nucleation theory would have been required and should be considered at future efforts in programming reactive flow.

Calcite dissolution simulations could be performed kinetically without having the above restrictions. For code optimization purposes, this scenario is favorable. However, in order to have continuous kinetic reactions at reactive surfaces, a pore fluid was set up as explained previously. The gradual equilibration of inflow and pore fluid could be observed. In early code builds, the kinetically-controlled geochemical calcite dissolution approach resulted in hardly visible dissolution or quite unfavorable computational requirements. In order to solve this problem, an alteration factor was introduced increasing the amount of pore alteration due to precipitation and dissolution. Then the kinetic dissolution of the calcite phase could be simulated with an appropriate computational time.

More complex calcite dissolution scenarios could finally be simulated including the handling of multiple reactive mineral phases and increasingly complex structures. With increasing complexity, the number of particles increased significantly and, thus, the required computational time once again had to be improved. Therefore, multiple particles occurring at the same voxel and same time were combined after equilibration to one particle with increased aqueous volume. This increased volume is considered at each pore equilibration to change the pore fluid more significantly and, thereby, to accelerate pore alterations. The amount of tracked particles and necessary IPhreeqc calls is thus reduced by up to two orders of magnitude.

The MPI-C++ code can be compiled on an up-to-date Linux workstation. Therefore, the additional source files have to be connected to each other by setting proper path and file names at the beginning of three source files. If compiler (GCC) and MPI are installed and up to date, compilation is initialized from the shell by executing:

```
mpicxx –std=c++1y –L/usr/local/lib –Wl,-rpath,/usr/local/lib –liphreeqc –o ReacDict
/SourceFilePath/ReacDict.cpp
```

The ReacDict executable is thereby written in the actual folder. The additional library paths are added to the compiler for finding the IPhreeqc library *liphreeqc*.

3.3.4 Code workflow

The workflow of ReacDict can be divided into three main parts (Fig. 7). These are automatically executed based on the individual input parameters. The parameters are written in a parameters file, which is called upon execution of ReacDict. On Linux workstations, the code is called as:

```
[mpiexec –n X] /home/users/./ReacDict /home/users/Parameters.txt [-restart N] [-skipGD]
```

Square brackets contain optional possibilities for initializing ReacDict. Depending from the workstation, by using the *mpiexec* or *mpirun* command, ReacDict may be set to run in parallel with X cores, which is highly recommended. An optional restart command is given as a possibility to quickly restart the code at a certain time step. Additionally, at first execution, the GeoDict modules may be skipped, which is useful in the case of restarting an aborted code execution at the geochemical part.

Once initialized, ReacDict threads process the input file and set up global variables, data vectors, directories and log files independently for each core. The original parameters file is copied to the project directory to store the input parameters. Several important input parameters are checked while for some critical combinations error messages are prepared together with code aborts to inform the user. Then, the GeoDict structure file is read, and each process is assigned an average structure volume split up along the X-axis. In case of pure diffusion scenarios, processes distribute equal amounts of particles randomly in the assigned permeable pore space. Particle positions are subsequently communicated to the root process that assigns solutions according to pore fluid(s) and reservoirs. Then, the initial particle positions file is created.

Once preparations are finished, the main loop starts as depictured in Fig. 7 and in more detail in Fig. 16. At first, if a flow field has to be computed, the control file is created and, subsequently, FlowDict (*LIR*) is executed from shell according to the parameters within that file:

```
FlowDictExecutable Directory/run0000/FileNaming_run0000.pde
```

Until FlowDict is finished, the processes are set asleep to be available for GeoDict. The resulting flow field is processed to obtain the Z-axis velocity values for the inflow voxels.

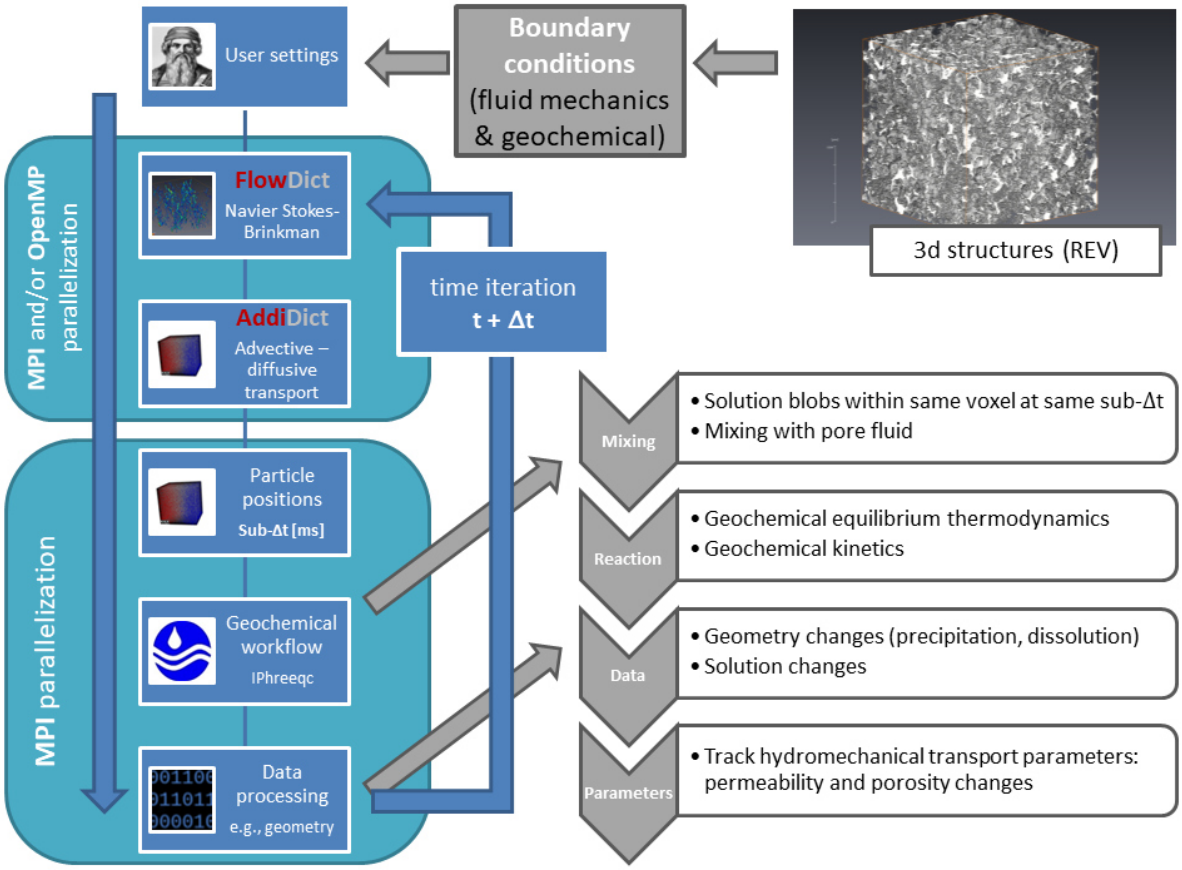

Fig. 16. Detailed workflow

This figure illustrates the functionality of the code in a higher degree of detail. The code execution is based on the user input that comprises the 3D structure and boundary conditions including the fluid mechanics and the geochemical system. The GeoDict modules FlowDict and AddiDict compute the flow and subsequently, the species transport. The particles act as solution blobs realizing the geochemical transport while following both advection and Brownian motion. The thus moving aqueous solutions equilibrate with the pore fluid at voxel resolution according to the particle positions, which are available at sub-time steps that are furthermore called the geochemical interval. Reactions are performed at reactive surfaces according to geochemical equilibrium thermodynamics and reaction kinetics if defined. The data processing includes the adaption of the matrices in memory such as geometry changes due to precipitation and dissolution. Also, all files in working memory are written to the disc while transport parameters such as permeability and porosity are tracked continuously (Hinz et al., 2019).

At the particle processing routine, inactive particles are searched in order to (re)move them. Trapped particles are moved to a random pore or permeable voxel nearby. Particles are removed from the model, if their volume was passed to another particle. Even though the reflective inflow barrier prevents particles from leaving the domain, the possibility is considered by removing the affected IDs and increasing the overall probability for new particles. Particles breaking through the outflow plane are removed while their chemistry is added up for storage in the log file. Afterwards, new particles are created in parallel based on the user parameters with homogeneously distributed starting times and the according inflow solution. The MPI processes communicate the previous, corrected and new positions to the root process that writes

these to the initial particles file. Then, based on user parameters, the AddiDict control file is created before initializing the tracker (e.g., *GD2018Tracker64*) from shell:

```
AddiDictExecutable Directory/run0000/tracker.pde
```

However, if an MPI version of the tracker is passed (e.g., *GD2018Tracker64Mpich3*), an additional file (*machines.txt*) is created containing the given number (e.g., *NumberOfProcesses 32*) of *PCname* lines before calling AddiDict:

```
mpiexec –machinefile Directory/run0000/machines.txt –n 32 AddiDictExecutable
Directory/run0000/tracker.pde
```

The parameter *mpiexec* may be used to change the MPI command including a certain path if necessary. Again, the processes are set asleep for being available to the GeoDict module.

In the first run and then every X runs (*DataDistributionEveryXdt*), the data is distributed among the processes according to the number of IPhreeqc calls expected during the actual time step. Therefore, the root process accumulates the number of particle positions (*Trajectories.gpt*) and non-equilibrated voxels (*KinPoreFluidReac1d.rd*) sorted in 1D along the X-axis. With the minimum number of three X-axis slices, the processes get assigned volumes in order to achieve a maximum of computational performance. Accordingly, the parallel cores process the above mentioned 3D data with halo areas wherever necessary. This includes the structure, the pore fluids, the reactive mineral phase fractions, the pCO_2 data and the tracked species molalities. At the first run, the latter four data sets are calculated and created from user data. Subsequently, the final particle positions are read into working memory from the according file to prepare the particle processing of the next time step.

The geochemical workflow runs progressively from the first interval to the last. For each interval and each voxel, the code looks for the necessity to execute IPhreeqc. In each case, the aqueous solutions are equilibrated, taking into account both the solutions carried by active particles and those inherent in the corresponding voxel. If a solid surface is available, then the (kinetic) geochemical equilibrium reaction is performed between defined reactive mineral phases and the equilibrated aqueous solution. Using the IPhreeqc keyword for passing only selected output, the resulting geochemical data can be processed automatically with optimized performance. The resulting solution is omitted to the corresponding voxel and particle solutions. Multiple particles are combined by default. The resulting passive particles are neglected at later

occurrences during the geochemical intervals. The eventually resulting mineral-specific Δmoles are transformed to a Δvoxel-fraction. This fraction is added or subtracted from the material fraction in the corresponding voxel. Since the six direct voxel neighbors are considered for reaction calculations, also neighbored voxel fractions may be altered if necessary. Thus, if the corresponding voxel reaches the alteration capacity, the available and reactive neighbors are altered with an equal distribution of the remaining Δvoxel-fraction. Material phase changes in halo areas have to be communicated with corresponding processes during the geochemical intervals. Thus, a blocking MPI communication is initialized to send and receive a minimum amount of material changes, when the code processes new X-axis slices at the rear halo area. These changes are then processed to update the corresponding phase vector and, subsequently, the structure. At the end of each geochemical interval, the particle solutions are updated for each process using blocking MPI communication. Nevertheless, MPI communication is carried out with minimal effort and only whenever necessary, whereby the parallel efficiency achieved by the data distribution procedure is maintained.

After the geochemical workflow, the next loop-run has to be prepared. If the structure was not changed at all during the time step, the geometry, flow tensor and flow resistivity files are copied to the next run directory. Eventually predefined closed pore voxels are examined for accessibility to become open pore space. The code then searches for porous voxels that are not connected to any solid voxel. These are removed from the simulation and stored as *VoxelError* in the log file while being considered as undissolved and outflowing. The data at the working memory is stored as new files in the directory of the next time step. The particle solutions file is directly created by the main process. Distributed data is collected by the main process and written to the new directory (reactive material phase fractions, compacted geometry, pore solutions, pCO_2, tracked species and non-equilibrated voxels). The root process updates the total geometry, which remains in the working memory. From the material fractions, the flow resistivity is calculated, communicated and written to memory. In case of pure diffusion, final particle positions are processed while particle types are updated according to reservoirs. Based on the resulting vectors, the new initial particles file is created. From the actual data, the total porosity is calculated, which is stored along other tracked parameters in the log file that is written to the actual and copied to the next directory and the *Summaries* folder. The results file of the FlowDict run is copied to the *FDResults* directory. These files enable a quick access to transport and geochemical parameters to post-process the resulting data.

Before the next time step begins, the code checks whether the run directory shall be stored at the *Saveruns_Xs* directory. Finally, excess data is deleted as stated by user parameters. Although produced data can rather quickly reach several TB, it is thus reduced to a fraction.

3.4 Post-processing

For the post-processing, flexible Matlab scripts are employed to calculate and plot results. Several Matlab functions are available for reading the various types of data files. In addition, the data can be automatically extracted from the project directory to produce a desired type of plot. In this work, all plots have been produced with such scripts. This includes diagrams and 2D plots, which can be resolved in time in order to produce animations. The open-source video editor Shotcut (*https://shotcut.org/*) has been used for creating animations from continuously created pictures. Some animated results may be watched at the authors YouTube channel (Fig. 17). There, results are shown as 2D and 3D visualizations. For continuous 3D images, GeoDict was utilized. Python macro scripts were employed for automation and consistent settings. Further information on Matlab tools and post-processing possibilities are available at the appendix (Table 25).

Fig. 17. YouTube channel QR-code
This QR-code links to a YouTube channel, at which several calcite dissolution animations may be watched (*https://www.youtube.com/channel/UCLxJs-vOl-OOX9tpptUDJCg*).

3.5 Limitations

Several features relevant to reactive transport are not considered by the presented workflow. Sorption is one of these. In addition, the alteration factor has to be checked manually and might be statistically inconvenient before reaching a steady state in the pore fluid.

In general, an important limitation is the computational time required to perform reactive transport simulations. The code limits the number of MPI cores to a third of the voxels in X

direction. However, the GeoDict software modules do not have this restriction. Table 3 specifies further performance increases achievable by increasing the alteration factor, decreasing the various time step parameters, reducing the number of inflow particles and the average particle velocity or by adjusting the FlowDict convergence parameters. However, changing the various parameters for performance reasons should be considered carefully, since it might have a crucial effect on the accuracy of the simulation.

Table 3. Performance increases by parameter changes

This table shows the parameters, which significantly reduce the runtime of the code or some modules. Here, reduced ReacDict runtime means more effective reactions and, therefore, reduced computational effort onto reaching a certain state of the system.

Parameter		**Performance change**	**Effect**
AlterationFactor	**× X ⇒**	ReacDict runtime	**/ X** (approx.)
AD.Trajectories.Timestep	**× X ⇒**	AddiDict runtime	**/ X**
GeochemTimestep	**× X ⇒**	geochemical runtime	**/ X**
SkipVoxel	**= X ⇒**	AddiDict, Geochemistry	inflow particles **/ X^2**
FD.PressureDifference, DiffusionCoefficient	**⇒**	AddiDict runtime	(individually)
FD.Equation (NSB, SB)	**⇒**	FlowDict runtime	(SB is faster)
FD.ErrorBound	**× X ⇒**	FlowDict runtime	(decreases)
FD.UseLateral	**= 0 ⇒**	FlowDict runtime	(decreases)
Material.SurfaceRoughnessFactor	**× X ⇒**	ReacDict runtime	**/ X** (approx.)

The geochemical possibilities are limited by hydrogeochemical knowledge. Several databases are available for PhreeqC, thus, already many applications are possible considering mainly non-kinetic geochemical modeling even at high temperature-pressure conditions and high salinity (Appelo, 2015). For additional capabilities, experienced geochemists may adjust and extend available PhreeqC databases to enhance the range of scenarios that may be simulated.

Reactions at the pore scale still have unknown variables such as the heterogeneity of dissolution locations at the sub-micron scale, which depends strongly on the local mineral structure (Fischer et al., 2012; Singh et al., 2018). This is tackled by the constant surface roughness factor that however, does not account for local differences whose impact is still unpredictable.

According to Menke et al. (2018), the definition of REVs for reactive flow is not yet sufficiently examined. Accordingly, a suitable multi-scale approach for numerical reactive flow models seems to be the topic for future research in order to cover phenomena at various scales. Nevertheless, the presented workflow is a powerful tool for modeling reactive flow in various geochemical systems at the pore scale.

4 Simulation setups and results

For code debugging, several different benchmark studies and dozens of test simulations have been performed while sequentially building ReacDict. This chapter describes the different simulation models and their results in a chronological order so that the development and increasing capabilities of ReacDict can be followed continuously. The following sub-chapters illustrate the progressively increasing code complexity while aiming at reactive interactions of cement at reservoir conditions in reservoir rocks. The geochemical systems are celestite ($SrSO_4$) precipitation and calcite dissolution, which is also combined with halite precipitation. The simulations were performed in different µCT-generated structures. The first models rely on diffusion-controlled conditions while later setups use continuous flow with varying inflow chemistry as numbered and listed in Table 4.

Table 4. List of simulation models
The models are numbered according to the sub-chapters with an alphabetical order of the models.

	Description
Model 1a	Diffusion-controlled $SrSO_4$ precipitation
Model 1b	Diffusion-controlled $SrSO_4$ precipitation only at grain surfaces
Model 2a	Halite precipitation on calcite grains upon NaCl inflow
Model 2b	Halite precipitation on calcite grains upon inflow equilibrated with respect to C-S-H jennite
Model 2c	Calcite grain matrix dissolution upon acidic inflow at pH 3
Model 2d	Diffusion-dominated calcite grain matrix dissolution
Model 3	Calcite matrix dissolution upon acidic inflow at pH 5.5 (Kreuznach structure)
Model 4	Kinetic dissolution of calcite pore cements upon acidic inflow in a reservoir sandstone

Code adaptions due to model requirements are explained in this chapter. However, some results also indicate necessary steps in code development. These are extracted from additional post-processing results as presented in the discussions chapter.

4.1 Celestite precipitation

The first test models rely on celestite precipitation experiments performed by Chagneau et al. (2015). $NaSO_4$ and $SrCl_2$ solutions diffuse from opposite sides of a sand grain structure towards each other. At the center of the structure, these solutions react resulting in the precipitation of celestite ($SrSO_4$). Non-kinetic geochemical equilibrium calculations were applied due to the

fast precipitation kinetics of $SrSO_4$. From a 600^3 ROI a rather small geometry of 128^3 voxels was chosen for performance reasons.

Chagneau et al. (2015) measured the original grain structure at a resolution of 6 μm^3/voxel using an X-ray device (CT-alpha 160, Procon, Germany). Reconstructions were performed by applying the Octopus Code (Inside Matters, Ghent, Belgium). The obtained 3D volume was segmented using Avizo (FEI Visualization Sciences Group, Bordeaux, France) with and without a non-local means filter (Buades et al., 2005). According to µCT data, the celestite precipitates reduce the porosity from 0.40 ± 0.03 to 0.30 ± 0.03 at the precipitation front (Fig. 6). With a thickness of ≤ 350 µm, this volume occupies 0.7 % of the total column length (Chagneau et al., 2015).

Semivariograms were created by A. Jacob (University of Mainz) in order to determine the existence and size of REVs in the geometry (Fig. 18) according to Jacob et al. (2019). The diagrams show a plateau and thus a homogeneous pore and flow distribution in flow direction for the ROI with 600 voxels in each direction. Although the transversal axes show a decreasing variance with increasing size, the structure is especially in flow direction representative for the sand column. Plateaus at semivariograms indicate REV sizes. Accordingly, the extracted geometry of 128^3 voxels is at REV size.

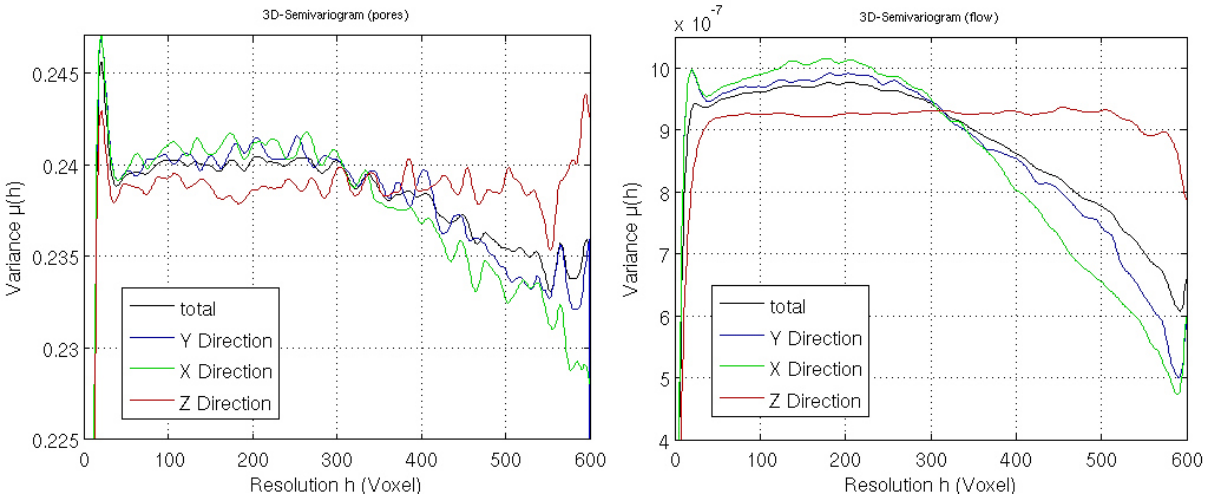

Fig. 18. Semivariograms for the celestite grain structure

The images show the statistic approach for determining the applicability of the ROI as an REV. The semivariograms show the pore-solid variances of voxel comparisons over increasing distance (left) and the variances of flow velocities (right). Flow direction is the Z-axis.

4.1.1 Simulation models

Two models are presented for simulating the experiment. For both, similar input parameters were chosen listed in Table 5. The difference is the mechanism of possible precipitation locations. The first model allows for reactions at any accessible pore space, calculating geochemical equilibrium reactions whenever multiple particles are found within the same voxel. The second model required additional coding for extending the possibilities of the workflow. Reactions were limited to quartz grain surfaces for preventing precipitations within the free pore space while thus allowing for more realistic results. The celestite reactions were performed under diffusion-controlled conditions based on data from Chagneau et al. (2015).

Table 5. Celestite precipitation simulation parameters – models 1a,b

	Δt [s]	**Δt (geochem) [s]**	**Voxel length [m]**	**Alt. factor**	**Solver**	**Reservoirs [voxel]**	**Particles**
Model 1a	10	0.041	$6 \cdot 10^{-6}$	4	NSB Simple-FFT	5 x 128^2	50,000
Model 1b	10	0.041	$6 \cdot 10^{-6}$	1	SB LIR	10 x 128^2	100,000

Initially, particles were randomly distributed in the entire geometry. The opposite reservoirs were each defined at a thickness of 5 and 10 voxels respectively. Particles within these initially carry the according fluid composition. The predominant amount of solution carriers was placed in between and was thus given an aqueous solution according to the background electrolyte as listed in Table 6. A voxel-wise pore fluid data was not yet included in these simulations. Instead, reactions considered an equilibration with the background fluid before performing equilibrium calculations.

Table 6. Celestite precipitation fluid chemistry – models 1a,b

Fluid data is extracted from Chagneau et al. (2015). Diffusion coefficients follow the relevant species and water in case of the background fluid.

	pH	**T [°C]**	**Na [M]**	**SO_4^{2-} [M]**	**Sr [M]**	**Cl [M]**	**D [$m^2\ s^{-1}$]**
NaSO4 reservoir	5.5	25	1	0.5	0	0	$1.29 \cdot 10^{-9}$
SrCl2 reservoir	5.5	25	0	0	0.5	1	$6.6 \cdot 10^{-10}$
Background fluid	5.5	25	0.001	0	0	0.001003	$2.2999 \cdot 10^{-9}$

During the simulation, carried solutions are equilibrated whenever particles are positioned in the according reservoirs including inherent particle diffusivity changes whenever necessary. The 128^3 ROI was encased with solid boundaries to prevent the particles from leaving the structure through the edges and thereby maintaining the fixed amount of particles. The

geochemical calculation interval was calculated based on Eq. (8). Therefore, the higher diffusion coefficient was considered while for Δx the voxel diagonal was chosen.

4.1.2 Celestite precipitation results

The simulations were performed until the reactivity nearly ceased. Both results show a total precipitation amount of above 100,000 voxels (Table 7), which are partly distributed on multiple porous voxels. This corresponds to 5.2 % of the entire structure. At the center, model 1a has 8.3 % of non-porous celestite voxels and 1.1 % of free pore space. 35.7 % are occupied by porous voxels containing varying amounts of celestite. On the contrary, in model 1b more than 30 % of the structure are occupied by solid celestite with an open pore space of 6.5 % and 8 Vol-% of porous voxels. Depending from the different alteration factor and half the number of particles, the first model required less simulation time explaining the lower computational time. The amount of core hours is caused by (1) the high temporal resolution and (2) the amount of performed IPhreeqc calculations (Table 7). The unproportional discrepancy between flow time and core hours is a result of the different amounts of particles that is nearly doubling the computational time.

Table 7. Celestite precipitation simulation results – models no 1a,b

	t (flow) [min]	**Total alteration [voxel]**	**Core hours [h]**	**Reactions**
Model 1a	430	$1.03 \cdot 10^5$	3,000	$> 10^{10}$
Model 1b	600	$1.09 \cdot 10^5$	7,600	$1.28 \cdot 10^{10}$

The first model shows a quite homogeneous precipitation front (Fig. 19). The celestite fraction within single pores is visualized increasingly in colors from yellow to dark green. The amounts of precipitate clearly increase onto the center, where solid celestite voxels dominate within a thin volume. Fig. 19 shows the geometrical development with a temporal resolution of 100 min per visualization and thus a reaction time of 400 min. The last picture shows the final state after 430 min.

The temporal development of the second model is illustrated in 3D in Fig. 21 showing the difference of the setup limiting reactions to surfaces. The purple celestite precipitates take the shape of the quartz grains. In comparison, the precipitation front is thicker in this model. This clearly is the result of the improved reaction conditions reducing the number of reaction spots.

The images show visualizations for every 50 min of flow and reaction time from initial to final geometry at 500 min.

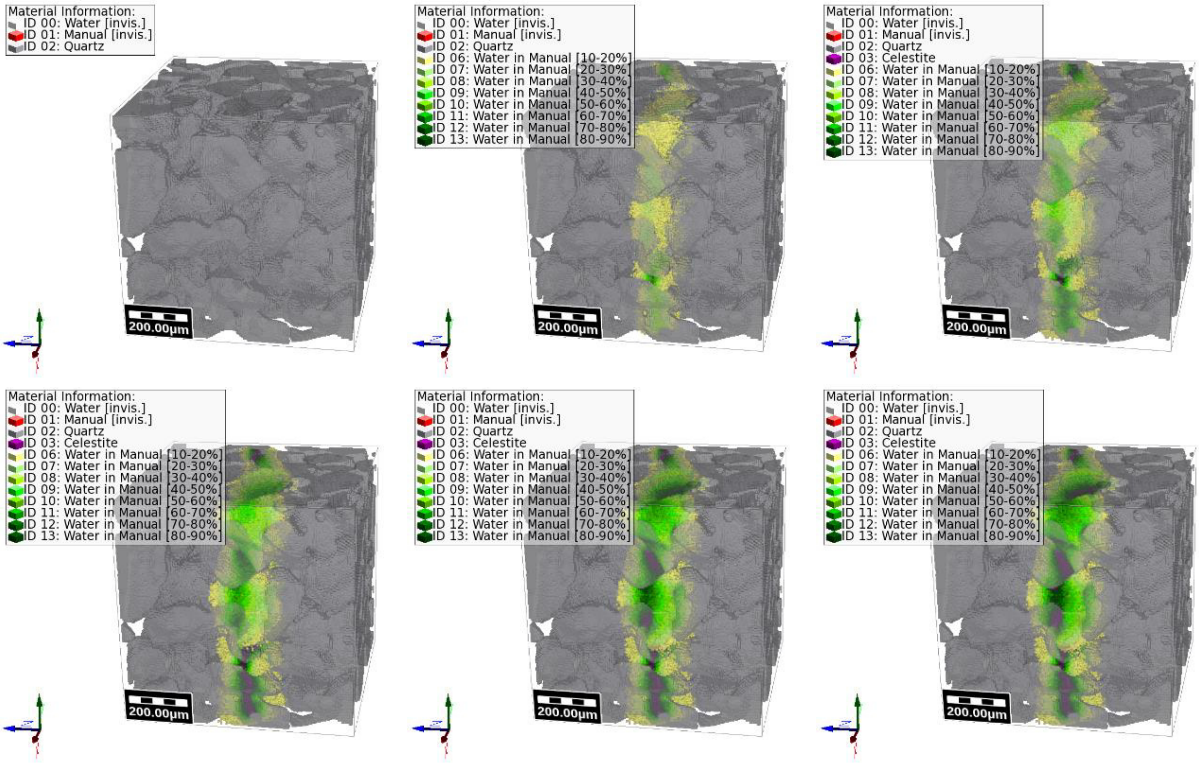

Fig. 19. 3D celestite precipitation results – model 1a

The images show the structure at time steps no 0, 600, 1200, 1800, 2400 and 2580 ordered from left to right and top to bottom. According to time steps of 10 s, 100 min of flow time and 400 min of reaction time are visualized including the final time step at 430 min ($t_{reaction} = 28.7\ h$).

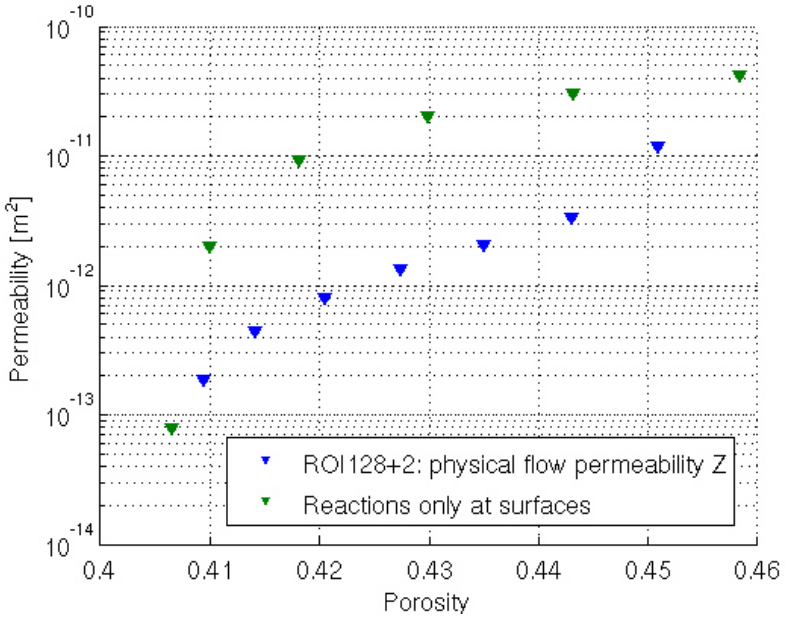

Fig. 20. Porosity-permeability diagram of celestite precipitation simulations

The resulting non-linear porosity and permeability reductions show a quite different relationship depending on the chosen reaction model. The curve for model 1b (green triangles) shows a more realistic development.

Considering the visualizations it is expectable that the permeability decreases slower at the second model. This estimation is proven true in Fig. 20 showing the porosity-permeability development for both simulations. The precipitations change the total porosity by less than 6 % while the permeability decreases by more than two orders of magnitude from $4 \cdot 10^4$ mD to $8 \cdot 10^1$ mD. These significantly reduced permeability values result from the high amount of clogged pore space at the precipitation zone. Thus, the permeability development is not directly correlated to the total porosity, but rather to the maximum porosity perpendicular to the reservoir zones and thus the flow direction of the permeability computations.

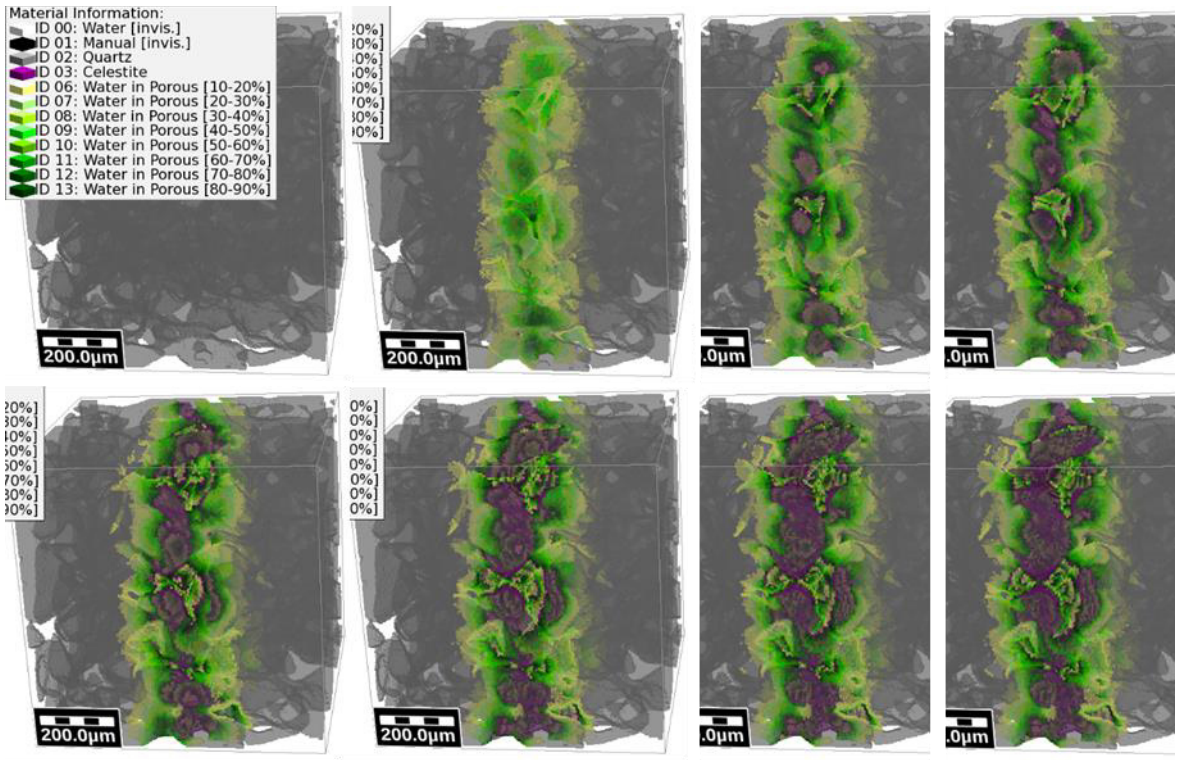

Fig. 21. 3D celestite precipitation results – model 1b

Images are shown from initial to final state from left to right and top to bottom. The visualizations are chosen at simulation times of 0 min, 50 min, 100 min, 150 min, 200 min, 300 min, 400 min and 500 min, which corresponds to up to 3000 time steps.

In Fig. 20, Model 1a (blue triangles) shows strong permeability reductions at the beginning and at the end. At model 1b (green triangles), the permeability decreases exponentially with time. With the surface precipitation setup, it takes longer to clog the pore space. Accordingly, the high permeability reduction begins later considering time and porosity. Considering the rather homogeneous pore distribution in a sand column and thus comparable pore throat sizes, the clogging of pore throats is not only expected, but also found to happen rather simultaneously.

4.2 Calcite grain matrix

For benchmark studies and code debugging, dozens of test runs were performed in the sand grain structure of Chagneau et al. (2015) with a constantly inflowing fluid. The quartz grains in the geometry were assigned to calcite grains. This approach enabled efficient calcite dissolution simulations. In this subchapter, simulation results for different geochemical systems are presented. For models 2a and 2b, the given pore fluid was used for equilibrating carried solutions before performing reactions at solid surfaces. This rather rough approach was then revised for implementing the voxel-wise representation of pore fluids. Thereby, new geochemical visualization possibilities were created, some of which are presented at the results for reaction model 2c and 2d.

4.2.1 Simulation models

In first continuous inflow simulations, the calcite grain matrix should be dissolved upon acidic inflow. Results showed that even equilibrium reactions didn't dissolve entire voxels in a decent computational time. But, when using reservoir fluid data an oversaturation of halite could be observed. Consequently, different calcite dissolution simulations were performed with regard to halite equilibrium reactions. Models 2a and 2b belong to these simulations. Both use different inflow fluids, but rather comparable further parameters except of the structure size. General input parameters are listed in Table 8.

Table 8. Calcite grain matrix input parameters – models 2a,b,c,d
FlowDict convergence is defined as error bound (EB) or permeability tolerance (tol) while only EB is providing an accuracy as given.

	Δt [s]	**Δt (geochem) [s]**	**Alt. factor**	**Solver**	**FlowDict convergence**	**FlowDict ΔP [Pa]**	**Particles per sec**	**Size [voxel]**
Model 2a	2	0.1	1	SB LIR	Tol 0.01	0.1	10,000	128^3
Model 2b	10	0.1	10	SB LIR	Tol 0.01	1	10,000	256^3
Model 2c	1	0.1	86400	SB LIR	EB 0.01	2	10,000	128^3
Model 2d	1	0.1	86400	SB LIR	EB 0.01	0.1	Based on Q	128^3

In first kinetically-controlled simulation approaches, the calcite grain matrix was continually dissolved upon inflow of a hydrochloric acid at a low pH value of 3.014 (Table 9). In difference to previous simulations, model 2c introduces the pore fluid approach at voxel resolution. Solutions in equilibrium with respect to calcite were initially defined in each voxel of the pore space. After performing additional parameter studies, an appropriately high alteration factor was chosen for achieving significant calcite dissolution amounts. For model 2c, it was thus

increased so that one second of flow time corresponds to one day of reaction time (Table 8). Model 2d uses an aqueous inflow solution at a lower acidity. It is equilibrated at the pH value of 5.5 (Table 9), whereby reactions are slowed down. Thus, the flow velocity was also reduced by setting the pressure gradient to 0.1 Pa (Table 8).

Model 2a uses an inflow fluid in halite equilibrium at high pressure and temperature according to reservoir conditions (Table 9). At reactions, the carried solutions were equilibrated with a reservoir solution that is additionally at a high salinity and in equilibrium with halite and calcite. Triggered by these equilibrations, the adjacent solid calcite becomes undersaturated and will be dissolved at minor amounts. The resulting marginal change in the fluid chemistry potentially affects the halite equilibrium as presented in the results.

Table 9. Calcite grain matrix fluid chemistry – models 2a,b,c,d

Pore fluids of models 2a and 2b are defined with reference to fluid data from the Rotliegend formation, kindly provided by S. Flesch, FSU Jena. The fluids are at equilibrium with respect to the mineral phases listed at column "equ.".

Fluids	**equ.**	**pH**	**T [°C]**	**P [atm]**	**Ca [M]**	**C [M]**	**Na [M]**	**Cl [M]**	**Si [M]**	**D [m^2 s^{-1}]**
Inflow 2a	halite	5.78	125	197.4	0	0	7	7	-	$1.5 \cdot 10^{-9}$
Pore 2a	calcite, halite	5.922	125	197.4	2.049	$3.648 \cdot 10^{-6}$	3.929	8.026	-	-
Inflow 2b	C-S-H jennite	10.389	100	197.4	$2.44 \cdot 10^{-2}$	0	0	0	$9 \cdot 10^{-7}$	$1.5 \cdot 10^{-9}$
Pore 2b	calcite, halite	5.92	100	197.4	2.049	$3.498 \cdot 10^{-6}$	3.629	7.726	0	-
Inflow 2c	-	3.014	12	1	0	0	-	0.001	-	$2.3 \cdot 10^{-9}$
Pore 2c,d	calcite	9.907	25	1	$1.23 \cdot 10^{-4}$	$1.23 \cdot 10^{-4}$	-	0	-	-
Inflow 2d	-	5.5	12	1	0	0	-	$3.168 \cdot 10^{-6}$	-	$2.3 \cdot 10^{-9}$

The inflow fluid of model 2b was equilibrated with the calcium silicate hydrate (C-S-H) phase jennite by applying the Empa CEMDATA07 database (e.g., Lothenbach et al., 2006; Lothenbach et al., 2008; Matschei et al., 2007) in PhreeqC. The simulation itself was performed using the Pitzer database published by Appelo (2015). This database improves calculations of hydrogeochemical equilibrium reactions in saline waters at temperatures up tp 200 °C and pressures up to 1000 atm. Model 2b was constructed for investigating the general possibility of modeling a contact zone between borehole cement and a reservoir rock at according reservoir conditions.

4.2.2 Halite precipitation results

The geochemical setups of models 2a and 2b resulted in high amounts of halite precipitation in a rather short simulation time. Both simulations used 32 cores resulting in a runtime of several hours as listed in Table 10.

Table 10. Halite precipitation simulation results – models 2a,b

	t (flow) [min]	t (reaction) [min]	Total alteration [voxel]	Core hours [h]	Reactions
Model 2a	9.2	9.2	$5.65 \cdot 10^5$	160	$6.8 \cdot 10^7$
Model 2a	22	220	$3.46 \cdot 10^6$	312	$3.9 \cdot 10^8$

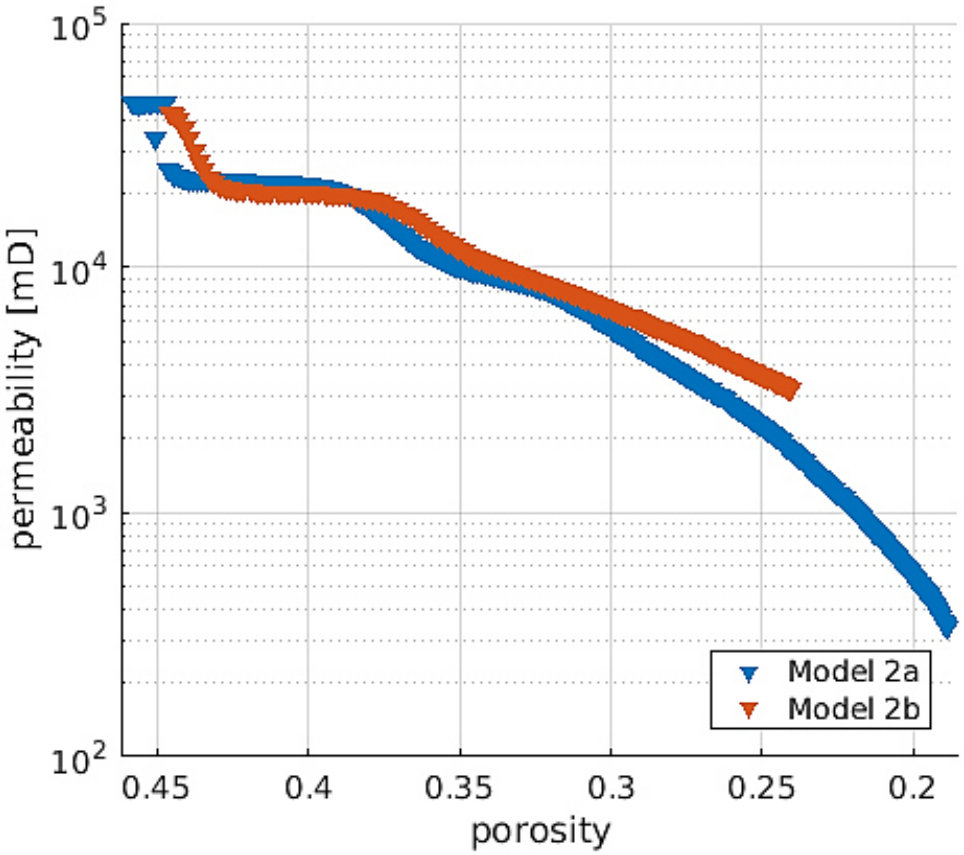

Fig. 22. Porosity-permeability diagram – models 2a,b

The plot shows the developments of the porosity-permeability relationship upon precipitation of halite. The curve decreases monotonously and slightly non-linear.

In model 2a, the halite precipitations were induced by minor amounts of calcite dissolution slightly increasing the SI of halite above 0. Initial reactions at calcite grain surfaces result in calcite dissolutions in the order of 10^{-7} voxel while halite precipitates at a fraction of 10^{-3} voxel in order to obtain a halite-fluid equilibrium. In average, 0.8 voxel-% are precipitated at each reaction as extracted from the ratio of reactions to total alteration (Table 10). That value is

higher than the amount calculated from values of the initial setup. Accordingly, the amount of precipitated halite increases during continuous equilibrations and reaction calculations. On the contrary, the porosity intervals in the porosity-permeability diagram in Fig. 22 are higher in the beginning compared to the end of the simulations. Two intervals of steeper curves are visible: (1) at the beginning starting with 46 % porosity and (2) at a porosity of 38 %.

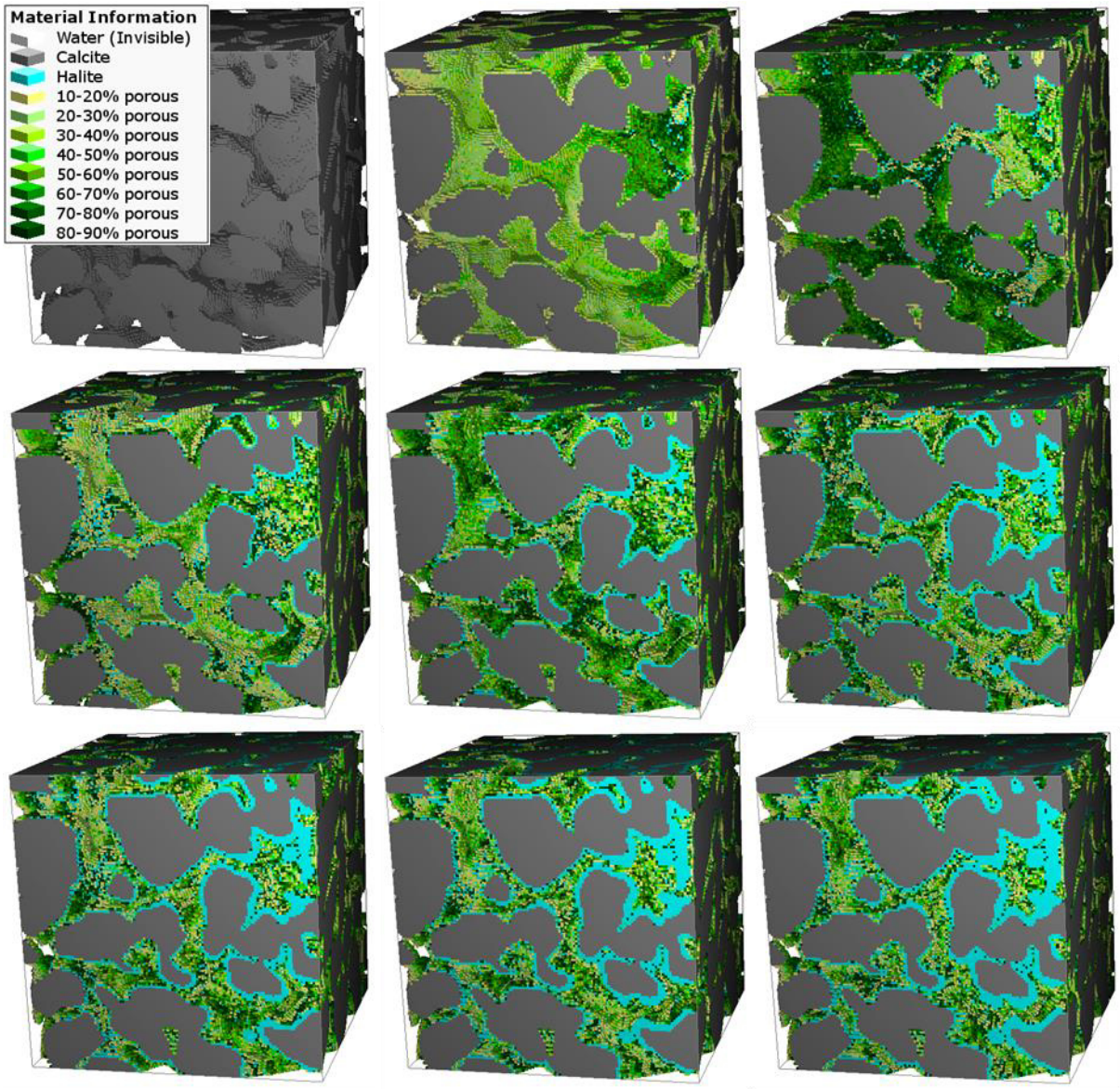

Fig. 23. Continuous halite precipitation in ROI 128³ visualized in 3d

Images are shown in intervals of one minute simulation time from initial geometry to the structure at 8 minutes. Halite is visualized in cyan, calcite in grey and porous voxels with increasing local porosity from yellow color to dark green. A decreasing halite gradient from the inflow region at the right-hand boundary to the outflow region is clearly visible.

The continuous formation of precipitates at calcite grains can be observed in Fig. 23 showing the structure in 3D at reaction time intervals of one minute. The inflow region is located on the

right-hand boundary, from which a pore alteration gradient is observable onto the outflow region at the left side. This gradient results from continuous decreases in the species concentrations carried by the virtual particles whereby less amounts of halite are precipitated.

The gradient of halite precipitates is plotted in Fig. 24 showing the highest halite fraction at the inflow region with a delay of 5 voxels, which were used for placing new particles. For half the structure at model 2a, halite precipitates occupy 29 % to 38 % of the geometry thus reducing open pore space up to a minimum of 7 % perpendicular to the flow direction. Calcite fractions were not changed visibly during the course of the simulation. Precipitates are reduced significantly near the outflow region indicating depleted aqueous solutions with respect to halite precipitation potential.

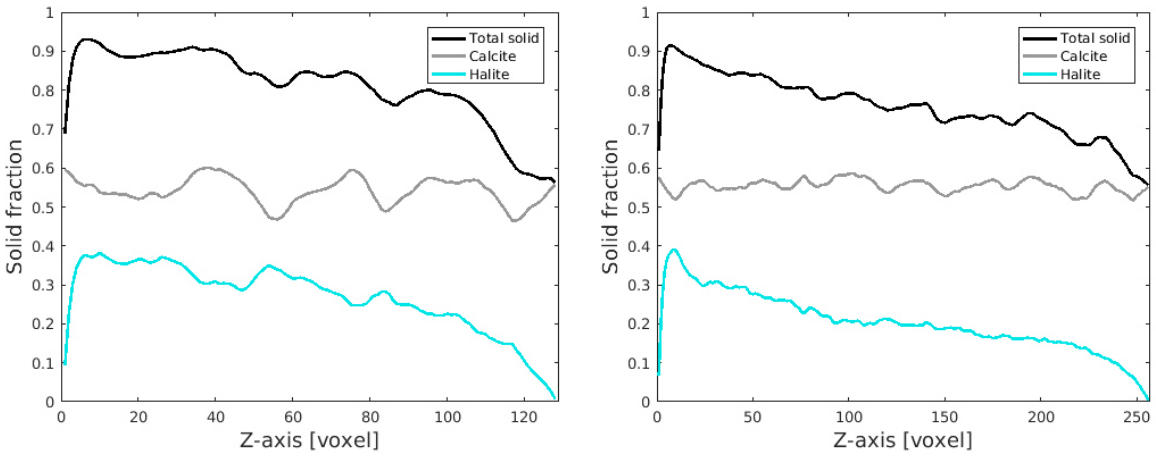

Fig. 24. Halite and calcite distribution in flow direction
The diagrams show the distribution of solid fractions on the Z-axis at the final time steps for models 2a (left) and 2b (right).

In model 2b, initial fluid equilibrations and subsequent reaction calculations result in the dissolution of calcite. Continuous changes in carried fluid solutions progressively induce an increase of the halite saturation index until an oversaturation with respect to halite is reached and the salt precipitates. In average, 0.9 voxel-% are clogged at each reaction. However, in consideration of the alteration factor that value would be 0.09 % in average per reaction. At a total flow time of 22 minutes, more than three million pore voxels were clogged by halite. With a comparably small amount of 312 core hours, hundreds of millions of PhreeqC calculations were performed (Table 10) while a maximum amount of 200,000 active particles were tracked simultaneously.

In Fig. 22, model 2b also shows two decreases in the permeability values compared to the porosity. Then the curve decreases less steep compared to model 2a. In Fig. 25, the development of the geometry is visualized in reaction time intervals of 25 minutes. The locations of halite precipitates show a slight gradient from the inflow to the outflow region.

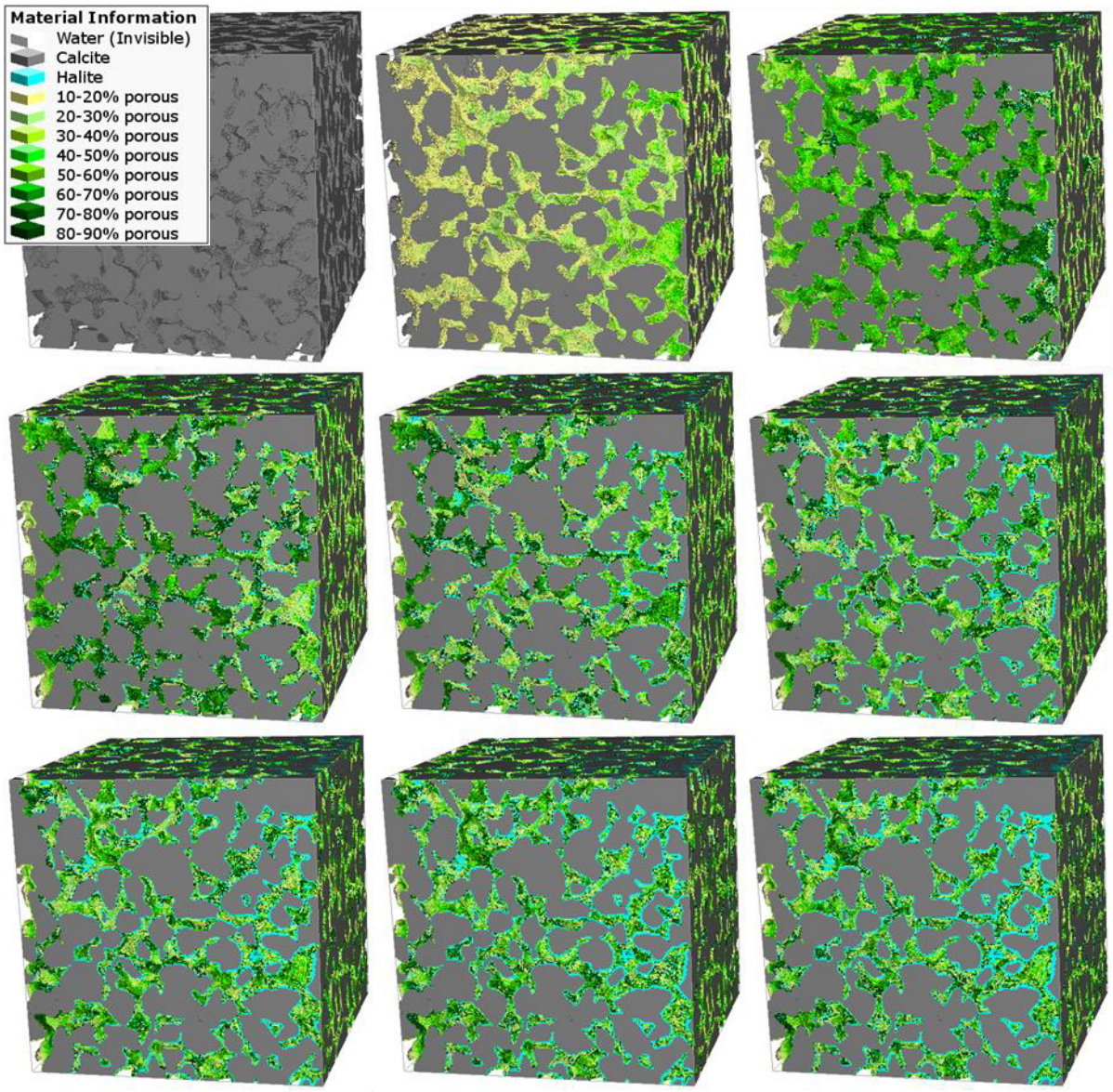

Fig. 25. Continuous halite precipitation in ROI 256³ visualized in 3d

Images are shown in reaction time intervals of 25 minutes from initial geometry to the structure at 200 minutes. Flow direction is from the right-hand to the left-hand boundary. Colors are displayed in the same manner as in Fig. 23 while also showing the halite gradient, but with a weaker intensity.

Fig. 24 shows a halite fraction peak near the inflow region with values from 30 % to 39 %. Then the curve decreases smoothly to approx. 15 % before a steep interval indicates a halite reduction onto 0 % at the outflow plane. However, the velocity increases above the resolution of the geochemical calculation interval. Accordingly, the curve steepness is explained by a

combination of both, a reduced probability for reaction calculations and a depleted reaction potential with respect to halite.

During development stage for individual pore fluid solutions at each voxel, an active tracking of the fluid chemistry was coded and tested on the geochemical system of model 2b. Thus, results for pH and pCO_2 values could be visualized as shown in Fig. 26. Initial pCO_2 values are set to zero. Accordingly, only most recent values were stored at places wherever IPhreeqc calculations were performed. At porous voxels, low values are tracked while at the precipitates, values up to $5.6 \cdot 10^{-3}$ are visible as a result of the reactions. This implies an increasing amount of carbon due to calcite dissolution while an anti-correlation is visible concerning the pH values. Tracked pH values are initially at pore fluid pH and approx. 7.4 at the precipitates as a result from the simultaneous reactions. Near the outflow region carried solutions are nearly depleted with respect to reaction potential. There, high pH values are observed that face low pCO_2 values. Concerning the visualized 2D slice, the halite gradient differs from the one visible in Fig. 25 probably due to slightly different input parameters.

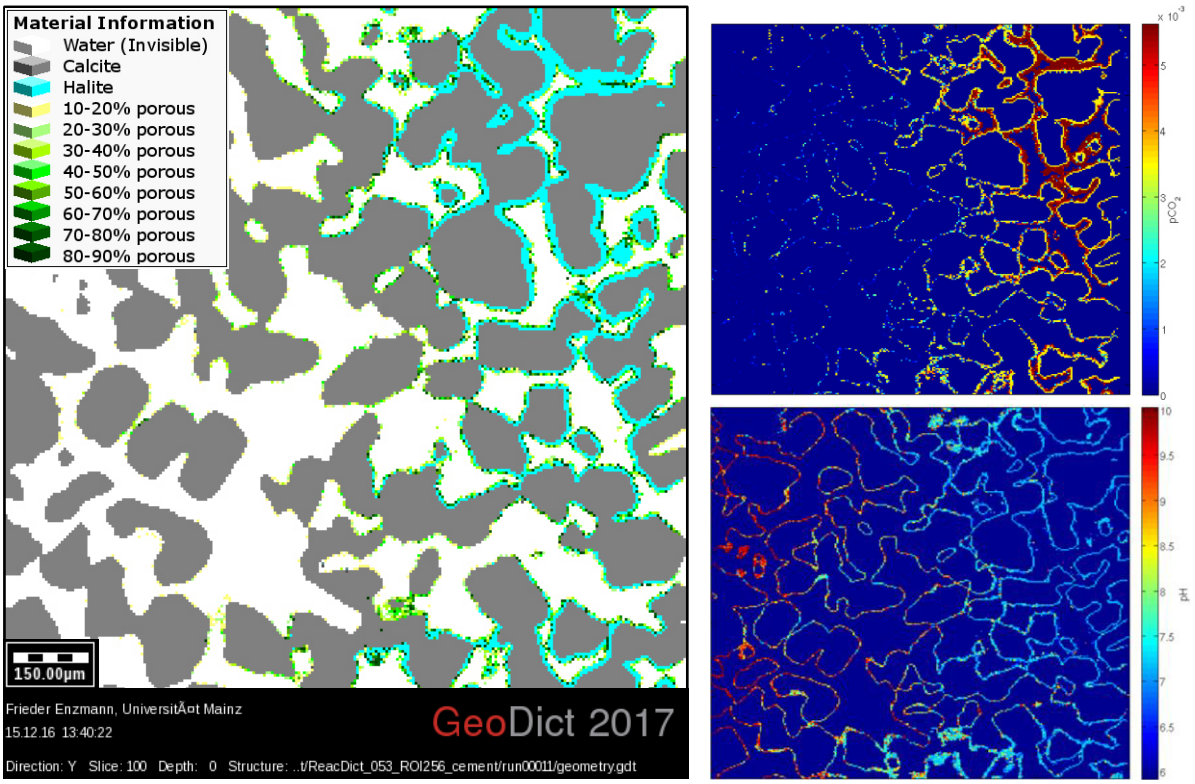

Fig. 26. 2d slices: structure, pCO2 and pH parameters, CSH jennite equilibrium scenario

Images show the cyan halite precipitates on calcite grains (left) with the according pCO_2 (top right) and pH values (bottom right) of a representative 2D slice. pCO_2 values range from 0 atm for non-reacting locations to $5.6 \cdot 10^{-3}$ atm, pH values from the initial 5.9 to 10.1. Flow direction is from the right-hand boundary to the left. At the inflow an offset appears that is related to the definition of the inflow region at a volume with five voxels thickness.

At the outflow region of the 2D slice in Fig. 26 (left-hand boundary), less precipitates can be observed compared to Fig. 25 while significantly higher amounts of precipitate are near the inflow region. Slightly different initial parameters were applied indicating the importance of carefully considered input values for simulating reactive fluids.

4.2.3 Calcite dissolution results

The kinetic dissolution of the calcite grain matrix was performed until the available calcite was nearly completely dissolved. This benchmark study highlights the possibilities of the implementation of pore fluids at the voxel scale. In a straight forward simulation at a total flow time of 35 minutes, a reaction time of 5.75 years was modeled (Table 11).

Table 11. Calcite grain matrix dissolution results – model 2c

	t (flow) [min]	t (reaction) [a]	Total alteration [voxel]	Core hours [h]	Reactions	Ca outflow Σ [M]
Model 2c	35	5.75	$1.07 \cdot 10^6$	1,400	$1.8 \cdot 10^9$	734.559

With above a billion geochemical calculations and a computational time of 1,400 core hours, the homogeneously distributed calcite grains were continuously dissolved upon the inflow of a hydrochloric acid. The initial pore fluid was gradually replaced by the inflowing fluid and the products of dissolution as visualized in Fig. 27.

The images in Fig. 27 show the development of the grey calcite grain matrix in relation to the propagation of the inflow fluid, which is represented by the chloride concentration that acts as a conservative tracer. Whenever the inflow solution reaches a calcite grain, it begins to dissolve continuously, which can be observed in a 3D animation following the QR-code in Fig. 17. The simulation shows homogeneous dissolution throughout the structure with a slight gradient in flow direction.

The porosity-permeability plot in Fig. 28 (blue triangles) shows a quite linear development. The permeability increases by a factor of five while the porosity increases by 50 %. However, the permeability increases in the order of two magnitudes in a synthetic dissolution approach (red triangles) also shown in Fig. 14. To explain this discrepancy, the calcite distribution along the Z-axis is plotted in Fig. 28. Several observations can be extracted from that diagram: (1) a dissolution gradient as expected from input parameters, (2) an increased amount of remaining calcite fraction at inflow and (3) outflow regions and (4) a remaining calcite fraction. New particles are created in a volume of five voxels thickness, thus inducing a reduced reaction

probability within that region and accordingly a decreased porosity. At the outflow region, the ratio of particle velocity versus geochemical calculation interval becomes increasingly unfavorable. As a consequence, less particles can be tracked at the outflow plane resulting in a decreased number of reactions and thus an increased amount of calcite having a significant effect on the permeability. In model 2c, reactions were performed exclusively at solid voxels and thus the remaining porous voxels of dissolved single grains could not be regarded. As a consequence, 2-4 % of calcite remain in the structure predominantly defined as porous voxels. The assigned flow resistivity at porous voxels has a significant impact on the flow field computation and subsequently on the resulting permeability.

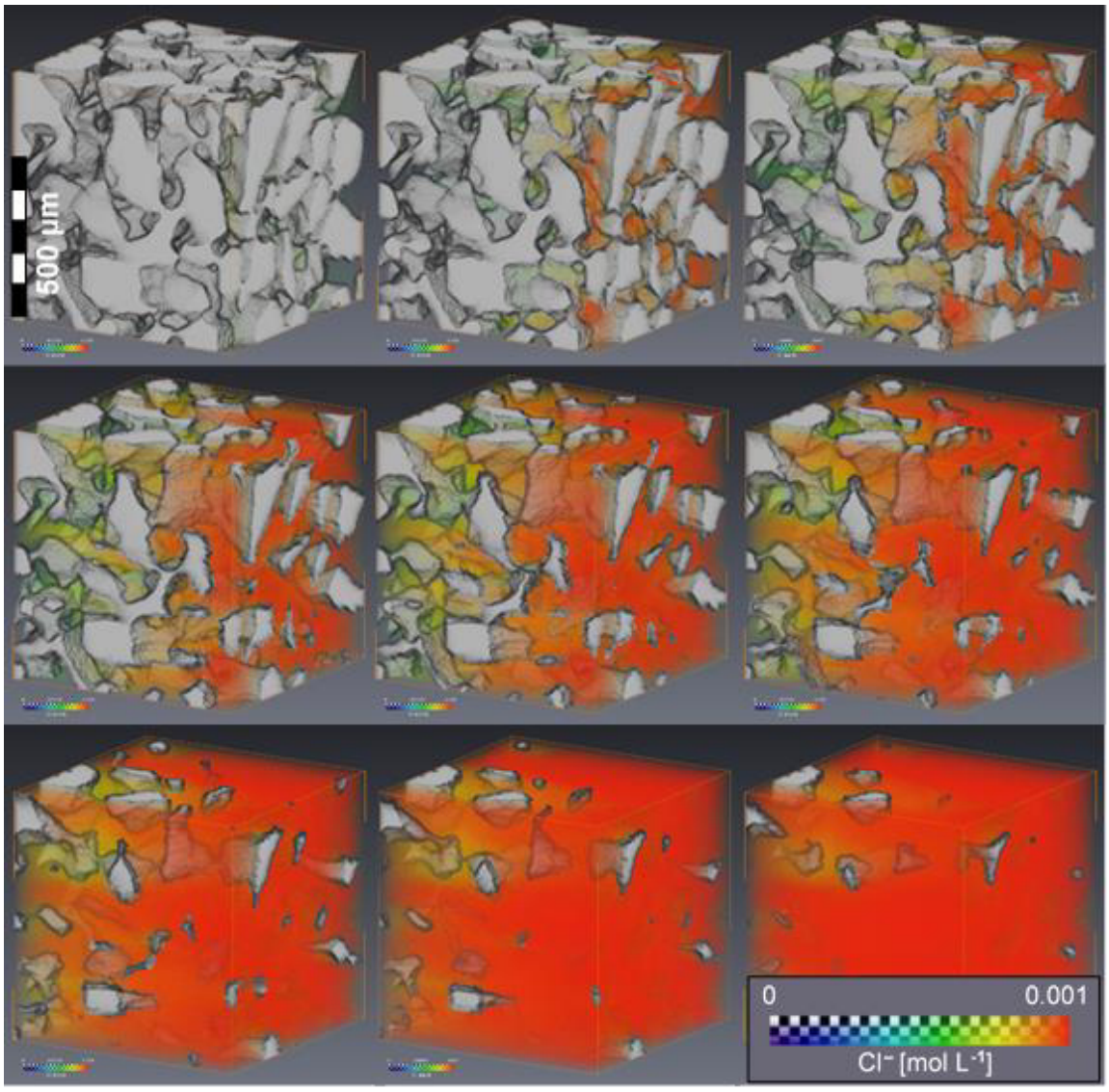

Fig. 27. 3d visualization of continuous kinetic calcite dissolution and Cl^- distribution

The continuously dissolved calcite grain matrix is visualized in grey at flow time intervals of 200 s and reaction time intervals of 0.5 a from left to right and top to bottom. The chloride concentration acts as a tracer for the inflow solution. An animation is available via Fig. 17.

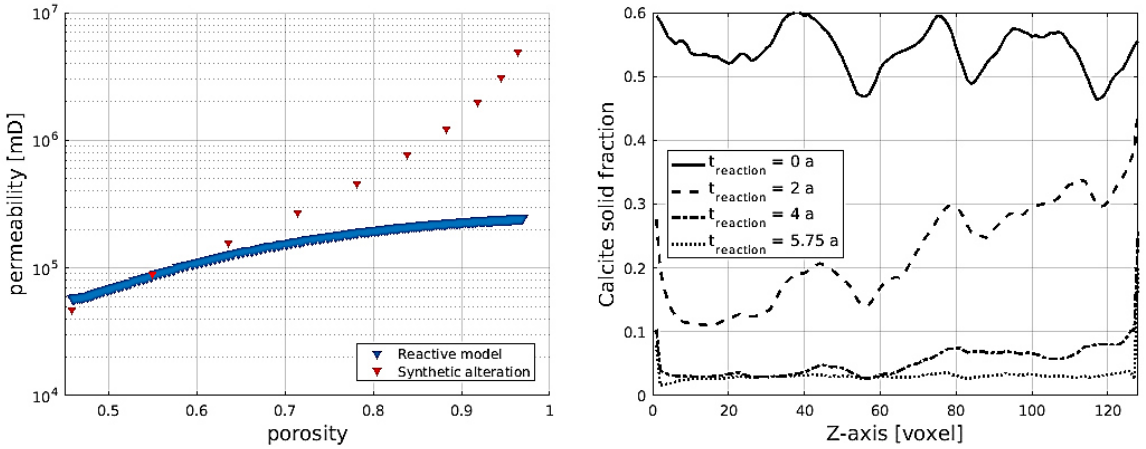

Fig. 28. Kinetic calcite grain matrix dissolution results

The porosity-permeability development of model 2c is compared to synthetic pore alteration showing a significant discrepancy in permeability values (left). The distribution of the calcite solid fraction in flow direction is shown at different time steps (right) from initial to final structure.

The development of the pCO_2 values in a representative 2D slice is shown in Fig. 29. Slightly preferred flow paths can be observed controlling the local reaction rates or the propagation of the pH values (Fig. 30). Dissolution products are visible as increased CO_2 partial pressure behind reacting calcite grains with regard to the flow direction. Thus, the pCO_2 values act as a reactive tracer.

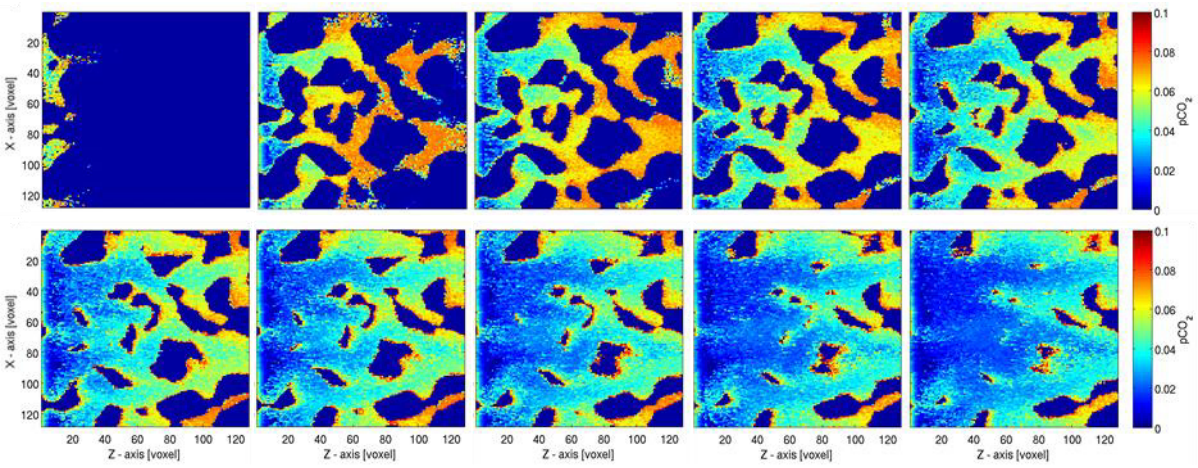

Fig. 29. 2D slices of pCO_2 parameters during continuous kinetic calcite dissolution

The pCO_2 values are shown in a representative 2D slice with inflow region at the left-hand boundary. Values increase from 0-0.1 atm in blue to red color. Calcite grains and the initial pore fluid have a pCO_2 of 0 atm. Visualizations were created in flow time intervals of two minutes onto a corresponding reaction time of three years. Images are aligned in chronological order from left to right and top to bottom.

In principal, all geochemical fluid properties can be stored and visualized. Another example is the pH value. Fig. 30 shows the development of the pH values that act as a reactive tracer. The continuous equilibration of the pore fluid and the inflow fluid and subsequently a replacement

can be observed. A predominant flow path develops in the upper half of the images highlighting the advantages of a reactive fluid model in relation to the synthetic approach.

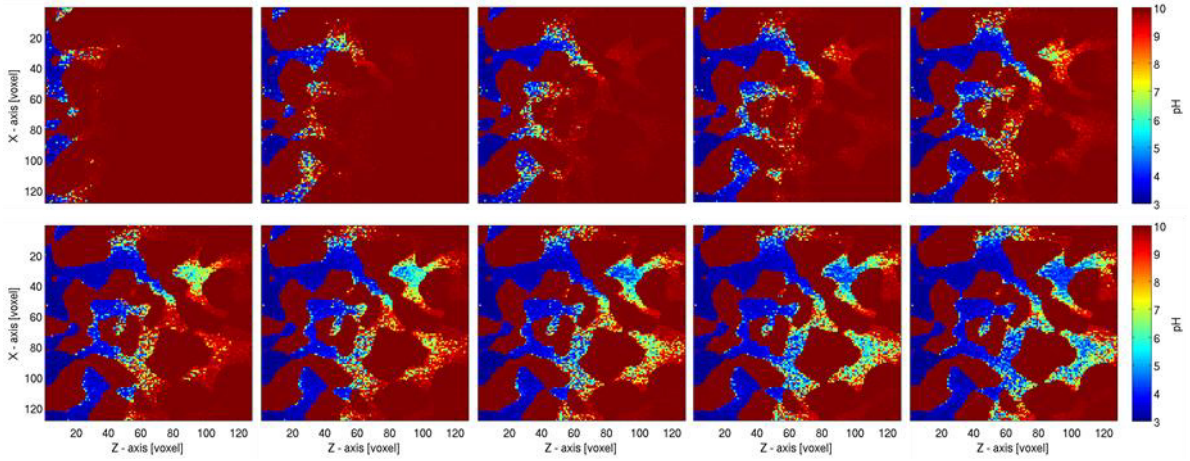

Fig. 30. 2D slices of pH parameters during continuous kinetic calcite dissolution
The pH values are shown in flow time intervals of 10 s onto the distribution at 100 s. Initial pH values for pore fluid and calcite grains are at 10. The images are arranged from left to right and top to bottom.

4.2.4 Diffusion-dominated calcite dissolution results

Declared as model 2d, additional simulations were performed based on model 2c to simulate calcite dissolution in a diffusion-dominated system. Various code adaptions were hereby tested as a consequence of the above described scenarios. The possibility of performing dissolution reactions on porous voxels was implemented into the code. In addition, particle creation was limited to the inflow plane, which required the construction of a solid inflow barrier in the geometry and also the flow field. Thereby, particles are prevented from leaving the structure at the inflow boundary. However, GeoDict releases starting with 2018 support reflective boundaries, so that the solid boundary option was afterwards replaced by that feature. The number of particles created at the inflow region is now calculated from the volume flow rate and not given as input parameter. The solutes are divided homogeneously at the inflow area. The possibility of simulating the motion of a strongly increasing number of particles implies the implemented possibility of both limiting the number of tracked particles and combining these when observed at the same voxel.

The accuracy of the geochemical calculation interval was increased due to few parameter changes listed in Table 8 and Table 9. Thus, the code adaptions could be tested at favorable conditions while expecting an improvement in the permeability development. Fig. 31 shows time-resolved 2D slices of the continuous calcite grain matrix dissolution with tracked chloride

concentration acting as a conservative tracer for the inflow solution. The included porosity-permeability development shows the permeability increase also in the order of two magnitudes, however induced by a jump in tracked parameters. This might be explained by an effect of the limited amount of particles. The aim of increased permeability values is anyway reached validating the applied approach in this point and for this rather favorable setup. The propagation of a dissolution front is observable in Fig. 31, which is typical for the face dissolution regime.

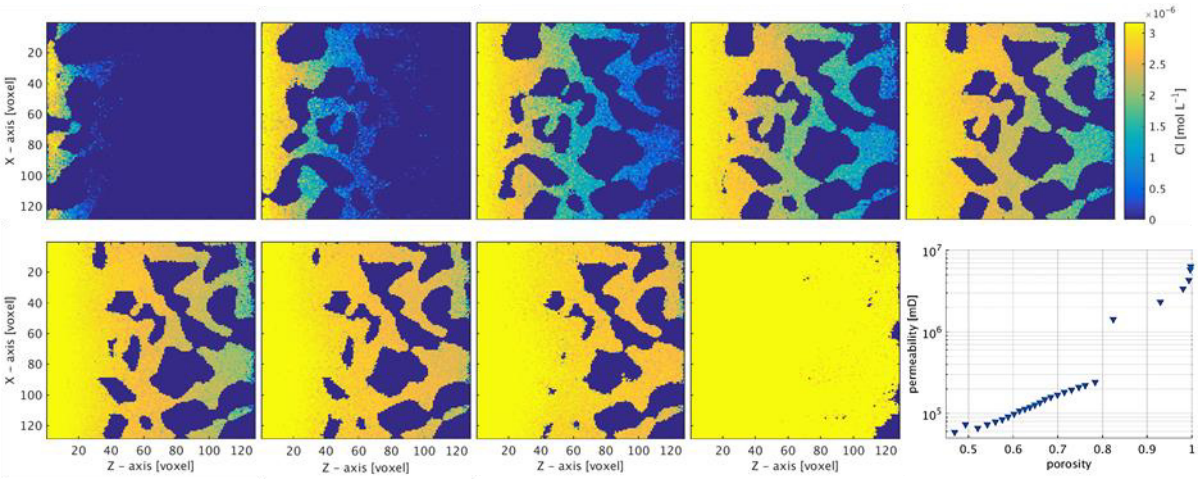

Fig. 31. 2D slices of Cl^- concentration upon acidic inflow and kinetic calcite dissolution
Increasing chloride concentration is shown in colors from blue to yellow. Initial pore fluid and calcite grains are depicted at 0 M Cl^-.

As a result of the parameter changes compared to model 2c, the dissolution regime can be clearly classified as face dissolution. The decreased pressure gradient results in a slower flow and thus an increased Péclet number of initially 2.6. A dissolution front can be observed migrating onto the outflow region. However, when the reaction front reaches approx. the center of the geometry, the reaction rate increases about an order of magnitude proportionally to the flow rate (Fig. 32). Accordingly, the jump in porosity and permeability is not observable in the Damköhler numbers. After a reaction time of 7 months, the porosity is at 93 %. Accordingly, the reaction rate decreases significantly until all calcite is dissolved. This simulation model was especially designed for code debugging and thus uses rather favorable parameters concerning the above mentioned discrepancies. Nevertheless, it validates the code adaptions at least for scenarios with appropriate time resolution or considerably slow flow in the face dissolution regime.

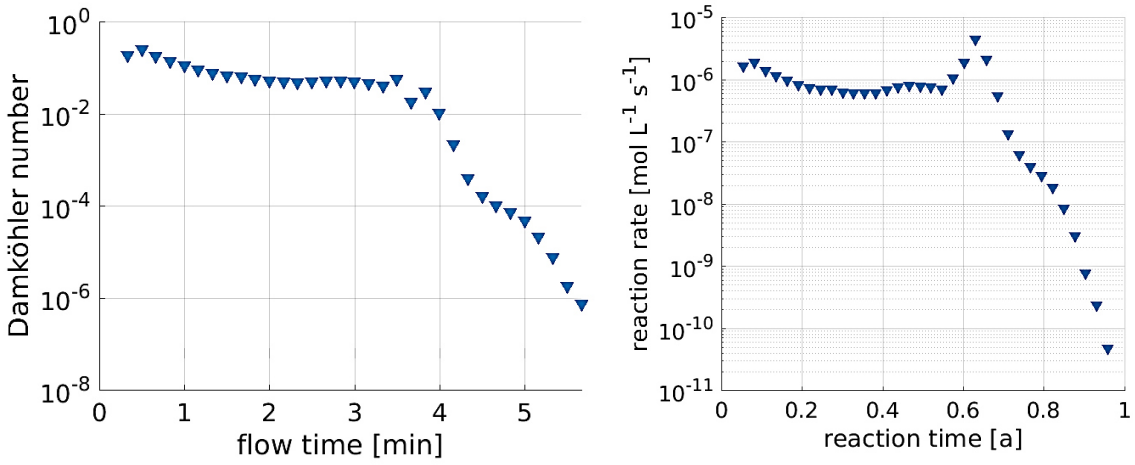

Fig. 32. Damköhler number and reaction rate plot

The Damköhler number development (left) is calculated in consideration of the continuously changing reaction rate (right).

Another test simulation shows continuous flow field changes as visualized exemplary with grid Péclet numbers in Fig. 33. Small variations are visible in comparison of 2nd and 3rd image representing successive data points and resulting in a reduced permeability (Fig. 34). The 4th and 5th visualizations show quite different flow fields and represent the permeability variances at an approx. porosity of 0.7 (Fig. 34).

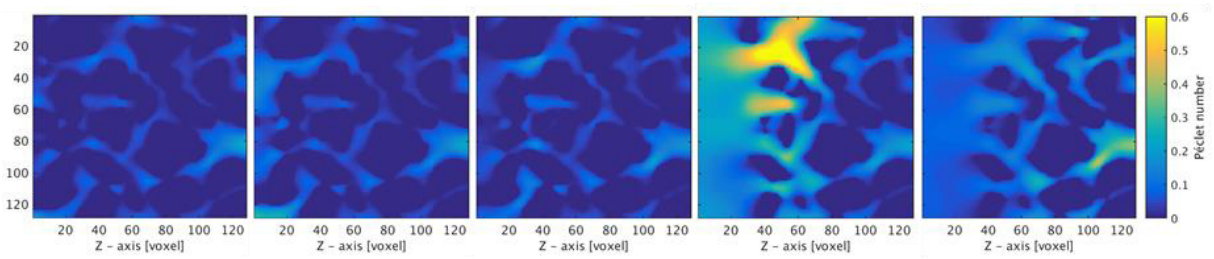

Fig. 33. 2d slices of grid Péclet numbers

The grid Péclet numbers of a 2D slice are given in a chronological order from left to right and top to bottom beginning with the initial values. The 2nd and 3rd image in the upper row show a first flow field change. 4th and 5th visualization depict a significant flow field difference. These discrepancies are also visible in the porosity-permeability plot and have a visible effect on the Damköhler number development.

The flow field variations affect the permeability and hence, have an impact on the Damköhler number development (Fig. 34). In this model, restart files were not used for the computation of flow fields. According to computation runtimes of several seconds, the convergence parameters appear to have been chosen too low. Although, flow field changes are possible, the effect on the permeability should not occur and thus unfavorably set parameters seem to be the cause. This model highlights the sensitivity of user-defined input parameters on the development of a reactive transport simulation.

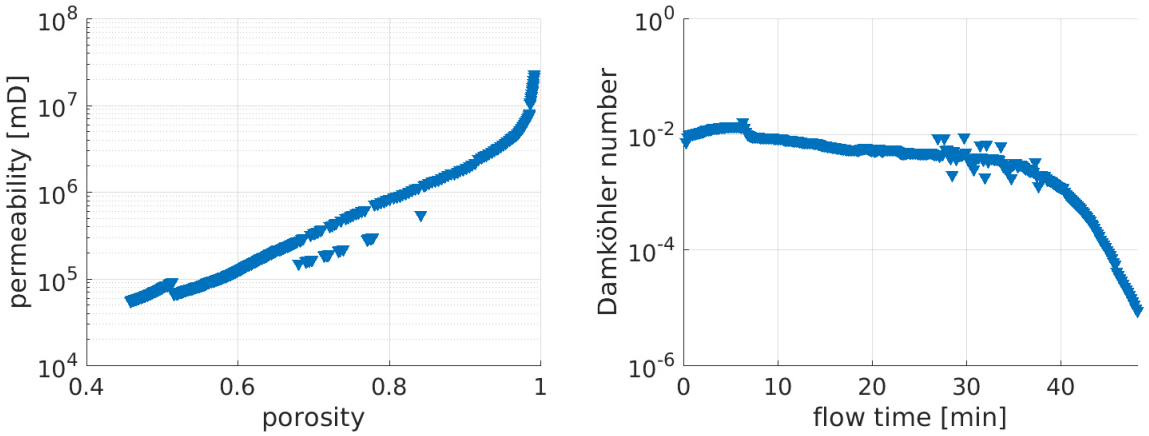

Fig. 34. Porosity-permeability and Da plot
The plot shows the effect of flow field changes on the permeability and Damköhler numbers.

4.3 Calcite solid matrix

The next step was to test the kinetic calcite dissolution workflow in a more complex geometry. Therefore, a Rotliegend sandstone structure of the Kreuznach formation (Saar-Nahe Basin, Germany) was used. For simplification of the geochemical system, the solid matrix of a 512^3 ROI was assigned to calcite. The pore space was increased by one voxel in each direction in order to make the pore throat diameter suitable for flow computations. The resulting initial accessible pore space occupied 20.74 %, which significantly improved the performance of the flow field computations. The structure was measured at the Swiss Light Source (SLS) of the PSI Villigen (Switzerland) resulting in a raw data set at a resolution of 350 nm as shown in Fig. 35. The reconstructed 3D geometry was at a resolution of 700 nm per voxel.

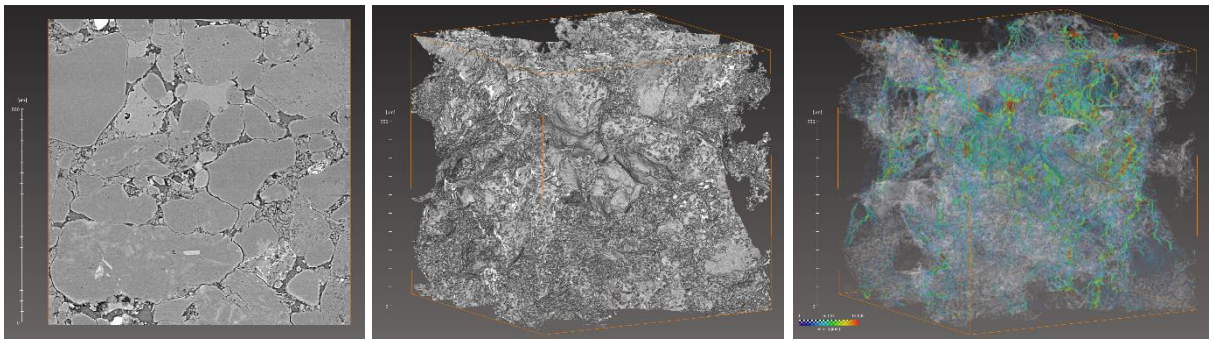

Fig. 35. Kreuznach structure grayvalues, pore distribution and flow field
The images show raw data based on measurements at the TOMCAT beamline of the synchrotron facility at the PSI Villigen (Switzerland). *Left:* A slice through the nano SRCT dataset with 2048^3 voxels at a resolution of 350 nm. *Center:* The 3D reconstruction of the segmented and connected pore space and (right) that pore space in transparent combined with the flow field computed according to the LBM Navier Stokes solver of GeoDict 2010.

This benchmark study examines the applicability of the presented workflow for this more complex structure consisting of small grains in a solid matrix. The fluid pathways are located between these small grains with a few voxels in diameter and larger grains with diameters up to 200 µm.

4.3.1 Simulation model

The structure is 64 times larger than the calcite grain matrix that was dissolved in a comparable geochemical system. The thus induced increase in computational runtime was avoided by further increasing the alteration factor by the factor of 30 (Table 12). Accordingly, one second of flow time corresponds to 30 days of reaction time. As a consequence, the time step had to be reduced to 0.1 s to limit dissolution reactions to the sub-voxel scale. The applied pressure gradient of 50 Pa results in an initial average physical velocity of 10.5 µm/s. Consequently, the geochemical calculation interval was reduced to 0.05 s to maintain a minimum accuracy. The average physical velocity is thus 0.75 voxels per time step, which corresponds to an initial average velocity in the pore space of 3.75 voxels per time step. The Stokes-Brinkman LIR solver was applied tolerating an error bound value of 0.1 in order to accelerate the computation. The input parameters are thus optimized for performance while maintaining a reasonable accuracy for this study.

Table 12. Kinetic Kreuznach calcite matrix dissolution – model 3

	Δt [s]	**Δt (geochem) [s]**	**Alt. factor**	**Solver**	**FlowDict convergence**	**FlowDict ΔP [Pa]**	**Size [voxel]**	**Size [µm]**
Model 3	0.1	0.05	2,592,000	SB LIR	EB 0.1	50	512^3	358^3

The geochemical parameters are used according to model 2d. The pH value was increased to 5.5, which in turn reduced the chloride concentration. The pore fluid composition remained the same.

Table 13. Kinetic Kreuznach calcite matrix dissolution fluid chemistry – model 3
Geochemical model parameters are according to model 2d (Table 9).

Fluids	**equilibrium**	**pH**	**T [°C]**	**P [atm]**	**Ca [M]**	**C [M]**	**Cl [M]**	**D [$m^2 s^{-1}$]**
Inflow	-	5.5	12	1	0	0	$3.168 \cdot 10^{-6}$	$1 \cdot 10^{-9}$
Pore	calcite	9.907	25	1	$1.23 \cdot 10^{-4}$	$1.23 \cdot 10^{-4}$	0	-

4.3.2 Calcite dissolution results

This simulation was performed with a total flow time of approx. five minutes and a reaction time of 25 years (Table 14). Tens of millions of calcite voxels were dissolved in 3050 time steps. The computational demand was rather high with 60,000 core hours that were required for tracking up to 650,000 particles at the same time resulting in several billion geochemical calculations.

Table 14. Kinetic Kreuznach calcite matrix dissolution results – model 3

	t (flow) [min]	t (reaction) [a]	Total alteration [voxel]	Core hours [h]	Reactions	Particles (up to)	Ca outflow Σ [M]
Model 3	5.08	25.07	$3.62 \cdot 10^{7}$	60,000	$2.4 \cdot 10^{10}$	$6.5 \cdot 10^{5}$	8914.61

The development of the flow field and the solid matrix is visualized in Fig. 36. The solid matrix is continuously dissolved, which is at first visible in regions with small grains and at the pore throats. At the latter, the velocity shows the highest values with a maximum of 1.9 mm/s. During the simulation, the velocity increases throughout the structure due to the constant pressure gradient and the increasing flow path diameters.

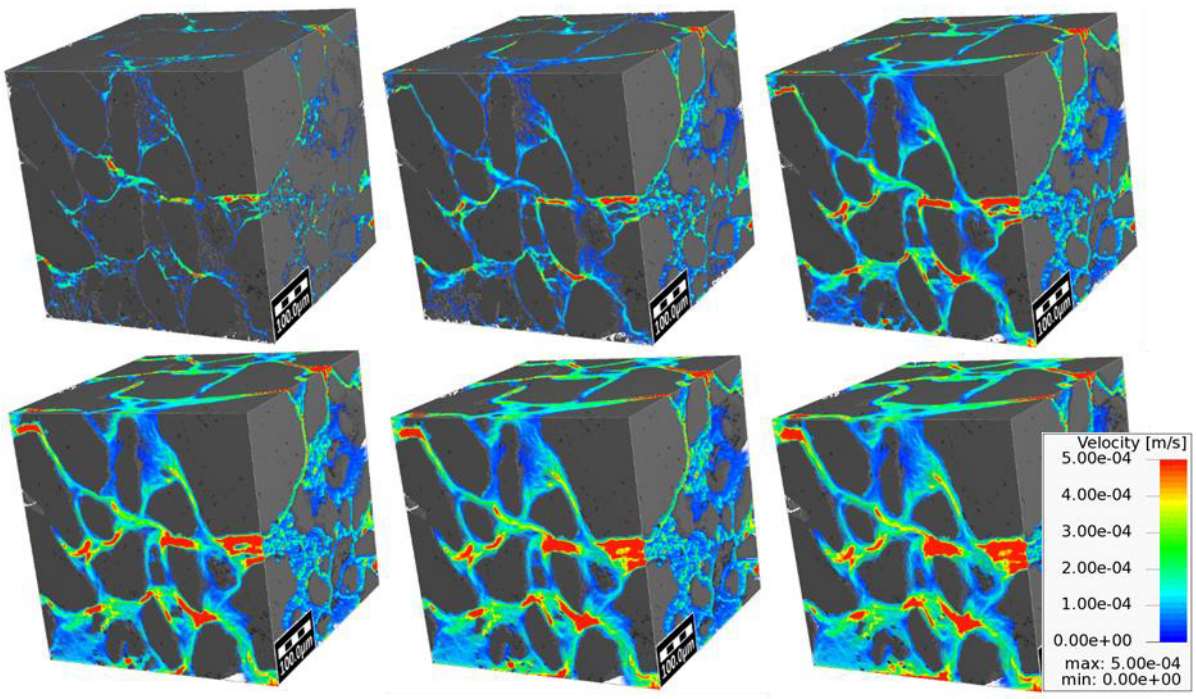

Fig. 36. Flow field development, Kreuznach structure

The images show the solid calcite matrix in grey and the Z-axis velocity according to the color bar. The visualizations are arranged from left to right and top to bottom beginning with the initial setup and continuing with flow time steps of one minute or reaction time steps of five years. Flow direction is from the right-hand boundary to the left side. An animation is available via Fig. 17.

The porosity-permeability diagram in Fig. 37 shows two non-linear effects. In the beginning the curve increases slowly until the total structure begins to dissolve and all relevant pathways become extended by the kinetic reactions. At a porosity of 30-35 %, small grains dissolve completely, which causes the curve to bend. The Damköhler number curve increases until particles are distributed throughout the structure. The inflow fluid continuously replaces the pore fluid implicating an increasing reaction rate, which is in the order of 10^{-8} mol/Ls. After that peak, the curve decreases monotonously due to (1) ongoing reductions in the available reactive surface area and (2) the general velocity increase proportional to the permeability.

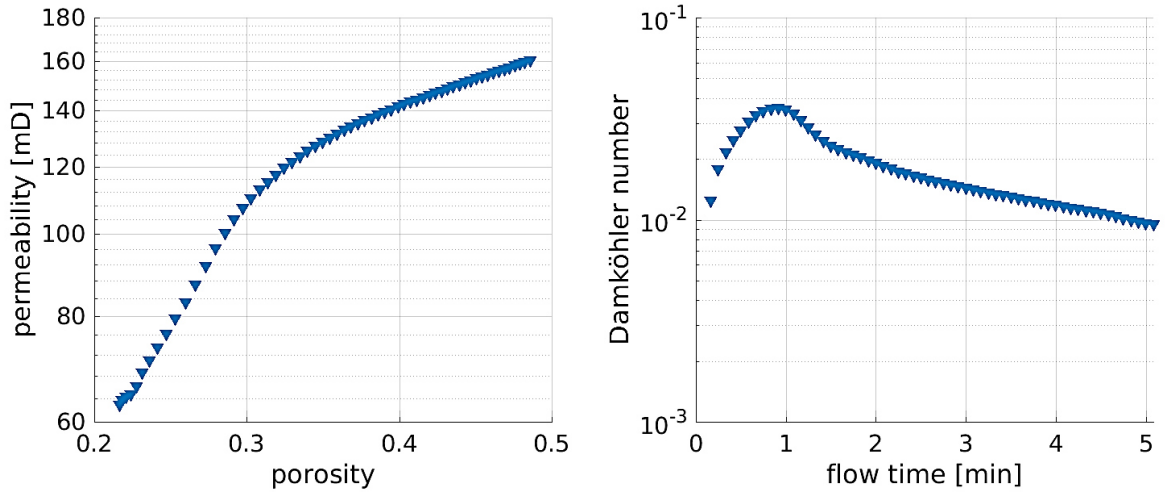

Fig. 37. Kreuznach structure dissolution results – model 3
The porosity-permeability development (left) and the Damköhler numbers plotted against the flow time (right).

Some geochemical parameters are visualized in Fig. 38 at different flow times of a few minutes. The pH values constantly show a gradient from inflow to outflow region. However, this gradient is gradually decreasing while pore fluids near the outflow region continually acidify. The chloride concentration again acts a conservative tracer. Clearly visible in the 2D distribution, the entire pore fluid has chloride concentrations according to the inflow solutions after few minutes of flow time. The temperatures of the individual pore fluids show a relatively slow adaption to the colder inflow water thus implying temperature to act as a non-conservative tracer.

The frequency of particles tracked within single voxels needs to be sufficiently high to accurately simulate the reactive transport. This frequency has been summed up based on the trajectories files and is visualized for increasing flow times in Fig. 39. Low frequency spots correlate to high velocities. Particles remain longer at regions with low Péclet number.

Accordingly, there is a higher frequency. The outflow region shows a lower frequency, because particles cannot diffuse backwards once they reach the outflow.

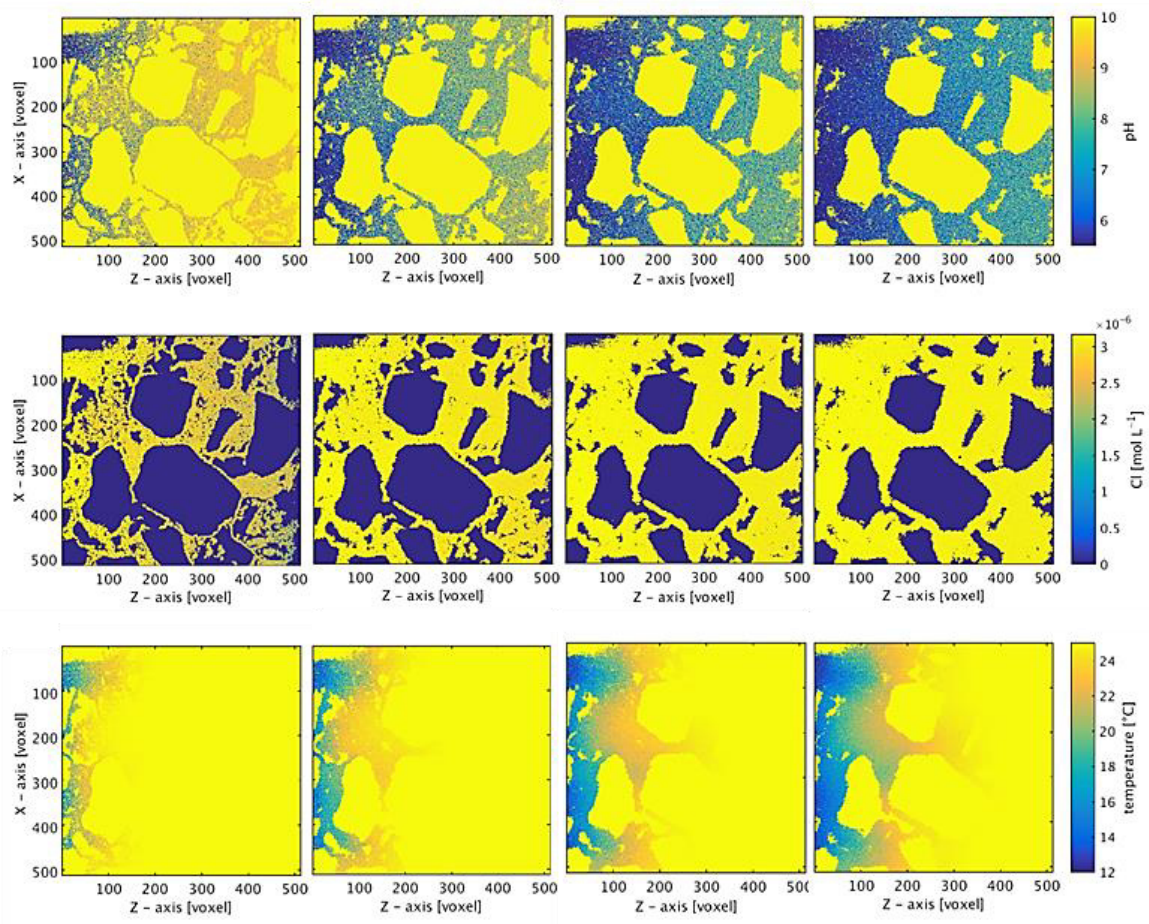

Fig. 38. 2D slices of geochemical parameters in the Kreuznach structure

The images show the pH value (upper row), the chloride concentration (center row) and the temperature (bottom row) of the pore fluid in a representative 2D slice at flow times of 1, 2, 3 and 4 minutes arranged from left to right. The inflow region is located at the left-hand boundary.

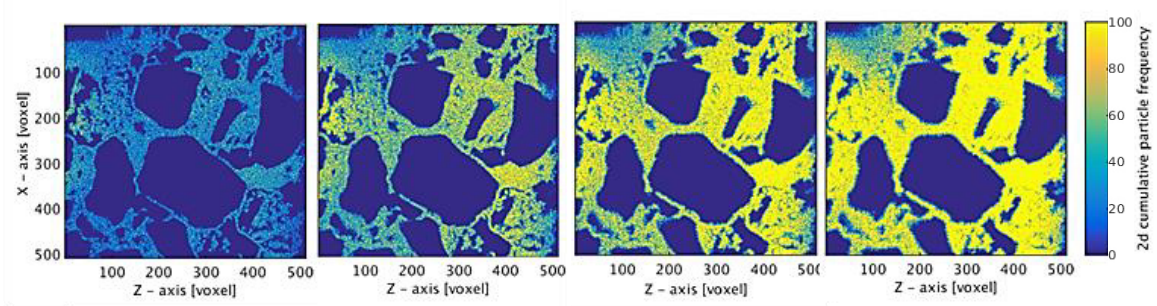

Fig. 39. 2D slices of the particle frequency in the Kreuznach structure

The images show the total particle frequency at flow times of 1, 2, 3 and 4 minutes arranged from left to right.

4.4 Calcite pore cement dissolution

The microstructure and geochemical system for the digital rock physics experiment was chosen so as to represent reactive flow in a typical geological reservoir. The calcite dissolution simulations were therefore performed in a µCT generated pore geometry of a reservoir sandstone sample. The sample plug was derived from the Rotliegend geological formation in Altmark region of Germany. The µCT scans were measured at the new P05 imaging beamline (Wilde et al., 2016) of PETRA III synchrotron facility (DESY, Hamburg, Germany). With a circumference of 2.3 km, PETRA III is the biggest and most brilliant storage ring light source in the world. The spatial resolution of the reconstructed geometry was as high as 1.27991 µm with an unprecedently brilliant phase contrast. Composition of the pore fluid is based on the highly saline formation fluid. Inflow of a hydrochloric acid causes an undersaturation with respect to the calcite mineral phase. The thus continuously induced dissolution reactions will open additional pathways and connect non-accessible pore voxels (Hinz et al., 2019).

4.4.1 ROI extraction

For the simulation runs, a ROI of 400^3 voxels was chosen yielding in a cuboid sample volume of just about 0.5 mm edge length. It was extracted from the segmented 3d image visualized in Fig. 40. The flow computation in a cuboid at maximum extent resulted in a dominant pathway. From that region, the chosen ROI was extracted as visualized in Fig. 40. Phase segmentation in that ROI using the materials property simulation code GeoDict revealed beside the dominating quartz content an initial open porosity fraction of 0.033, a calcite cement volume fraction of 0.168 and a minor barite volume of 0.0037.

Fig. 41 shows the initial calcite and open porosity distribution from the opposite side. Not visualized is the closed porosity fraction of 0.010, which is expected to become accessible during calcite pore cement dissolution.

Although the existence of an REV seems doubtful when looking at the flow field in Fig. 40, a semivariogram was created to obtain insights on a potential REV size. This work was conducted by Arne Jacob (University of Mainz, Germany) according to Jacob et al. (2019). Results are shown in Fig. 42 describing the spatial variance of solid and pore. In the semivariogram, plateaus typically indicate potential REV sizes. However, reduced data points close to maximum lengths result in boundary effects, thus the existence for REVs at lengths >350 voxel

is not given within this particular sample. Accordingly, also the plateau at smaller REV lengths cannot inhibit structures representing the entire digital rock sample or the corresponding reservoir rock formation. The increasing variance for X- and Y-axes at lengths beyond 350 voxels might correlate to the dominating flow paths and the implicated increased local porosity visible in Fig. 40. In contrast, the slice-wise calculated variance does not reproduce this effect. Since an REV is not given considering the pore-solid distribution, any considerations for REV in a reactive flow model are thus redundant.

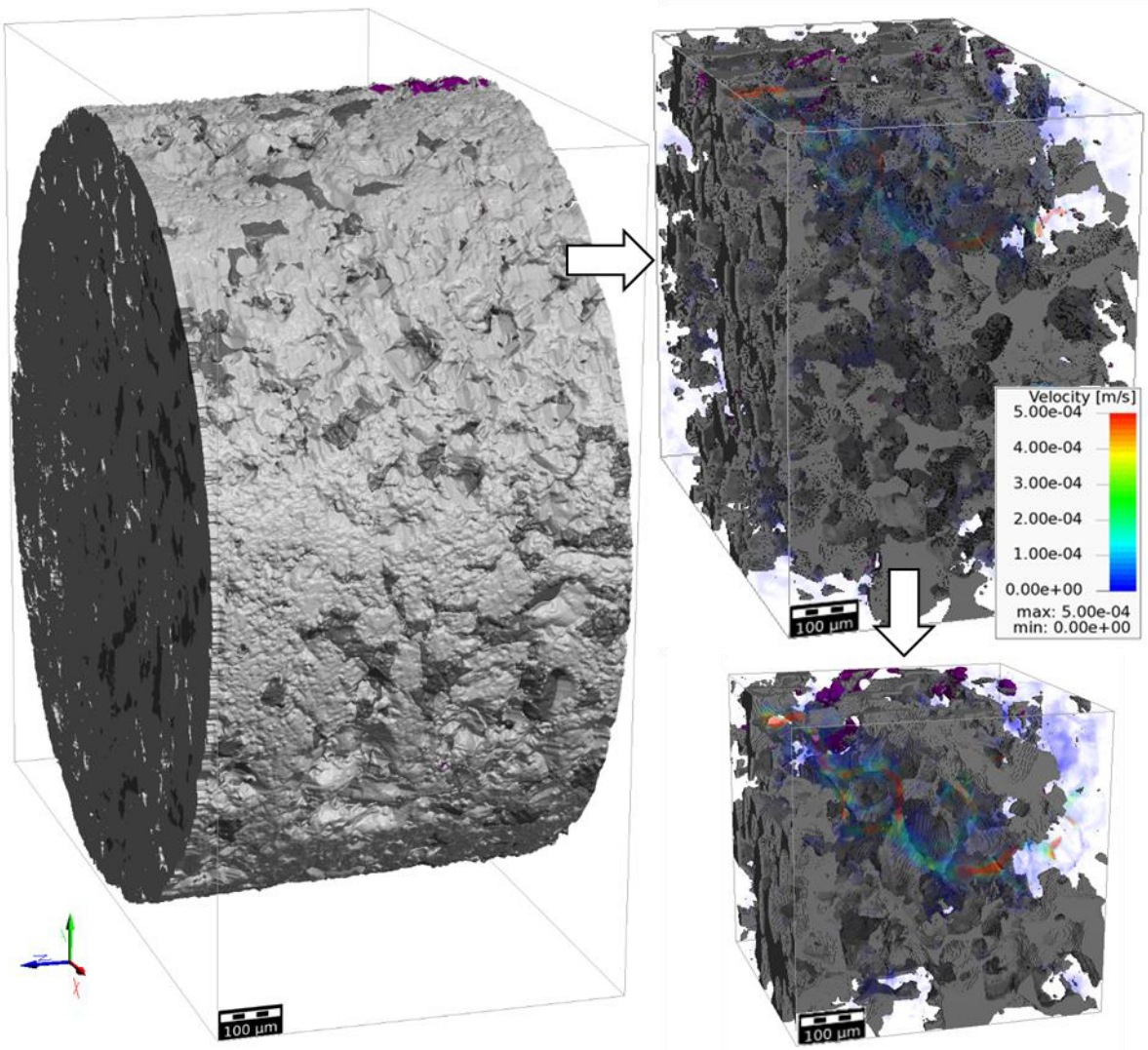

Fig. 40. Rotliegend formation structure

The images show (1) the full µCT structure, (2) the cuboid extracted from the sample and (3) the applied ROI. The quartz matrix is shown in light gray, calcite pore cements in dark gray and barite grains in purple. The flow fields of the extracted geometries are calculated at similar parameters and thus visualized with the same color bar.

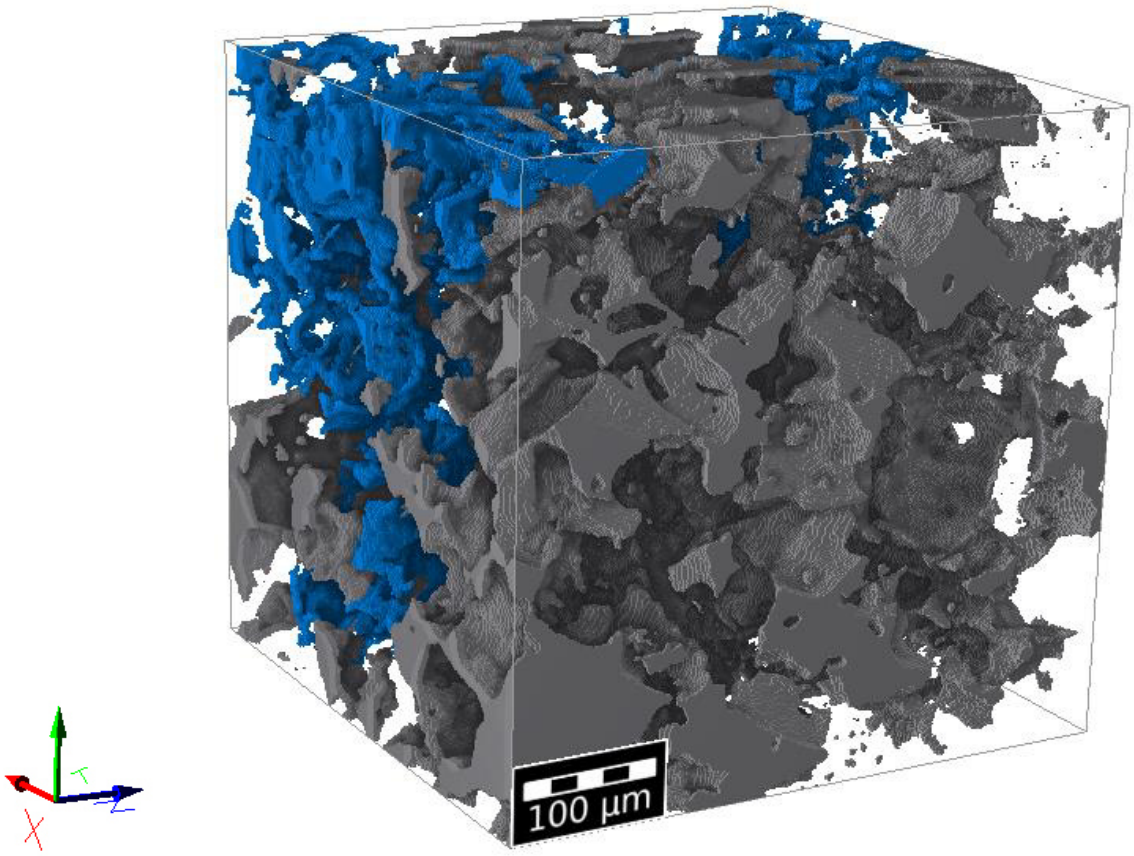

Fig. 41. Calcite pore cement and accessible pore space

The visualization of the simulation ROI shows the initial calcite pore cement distribution in grey, and the open porosity in blue.

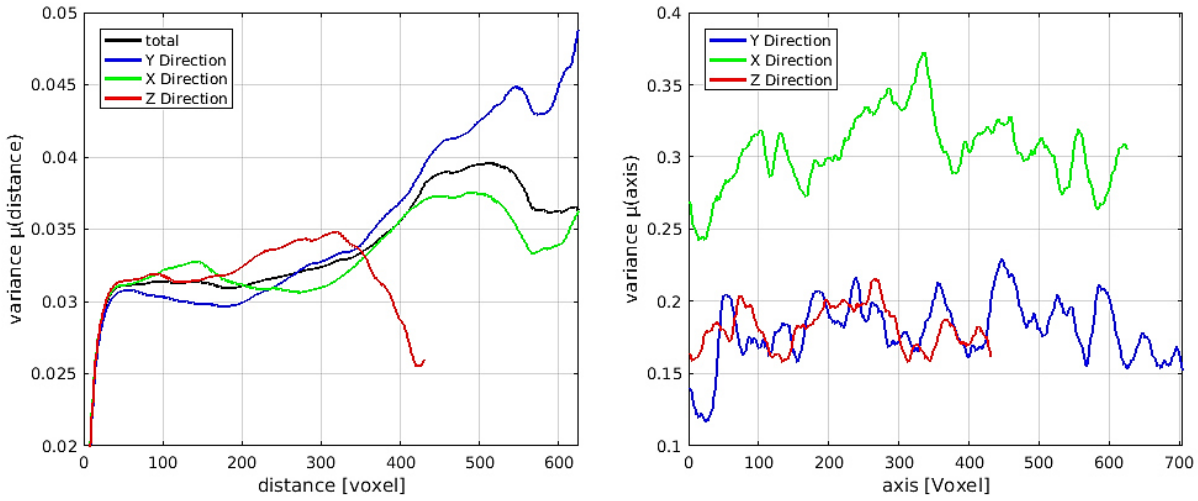

Fig. 42. Semivariogram and slice variations for REV determination

The semivariogram shows the pore-solid variances of voxel comparisons over increasing distance (left). The slice-related variances are plotted as the mean value of all voxel variances within a single slice (right).

4.4.2 Simulation model

Declared as model 4, kinetic calcite pore cement dissolution was simulated at an even higher alteration factor while still limiting pore alterations at kinetic reaction time steps of 1 s to the sub-voxel scale even though that time corresponds to 30 days of real reaction time. Flow was solved with the SB solver at an accuracy of 99.9 %. The computational cost is decreased when neglecting the Navier term at the flow solver, which is here fairly reasonable considering the initial average velocity of 24.8 µm/s. According to this value, solutes initially move approx. one fifth of a voxel far per geochemical calculation interval. This high temporal resolution results from parameter studies of previous simulation models.

Table 15. Calcite pore cement dissolution input parameters – model 4

	Δt [s]	**Δt (geochem) [s]**	**Alt. factor**	**Solver**	**FlowDict convergence**	**FlowDict ΔP [Pa]**	**Size [voxel]**	**Size [µm]**
Model 4	1	0.01	2,592,000	SB LIR	EB 0.001	50	400^3	512^3

The formation fluid data was kindly provided by Dr. S. Flesch (institute for geosciences, Jena, Germany). It was measured using Inductively Coupled Plasma Optical Emission Spectrometry (ICP-OES). Composition of the highly saline fluid is compiled in Table 16. For the simulation runs, the fluid composition was reduced to the main components of interest and equilibrated with calcite at atmospheric pressure but elevated temperature of 60 °C by employing respective PhreeqC script modules. The pH of the inflow fluid was adjusted at 5.5 by adding respective amount of hydrochloric acid to induce calcite dissolution reactions. Per geochemical calculation interval, the kinetic reaction calculations thus result in calcite dissolutions of less than 0.14 Vol-% in each reacting voxel containing calcite volume fraction.

Table 16. Calcite pore cement dissolution fluid chemistry – model 4
The pore fluid is based on the highly saline Rotliegend formation fluid. The inflow fluid is a hydrochloric acid.

Fluids	**Calcite phase**	**pH**	**pe**	**T [°C]**	**C [M]**	**Ca [M]**	**Cl [M]**	**Na [M]**	**D [$m^2 s^{-1}$]**
Pore	equilibrium	6.3	-1.5	60	$3.4 \cdot 10^{-4}$	2.05	8.99	4.89	$1 \cdot 10^{-9}$
Inflow	undersaturated	5.5	4	60	0	0	$3.1 \cdot 10^{-6}$	0	-

4.4.3 Kinetic reactions results

Due to the acidic inflow solution, calcite dissolution was initiated at sub-voxel scale leading successively to opening and extending of flow paths, which could be followed in time and space at high resolution. With a simulation run time of about 45 min, a real kinetic reaction time of 222 years could thus be simulated and visualized in form of a time lapse movie (Fig. 43).

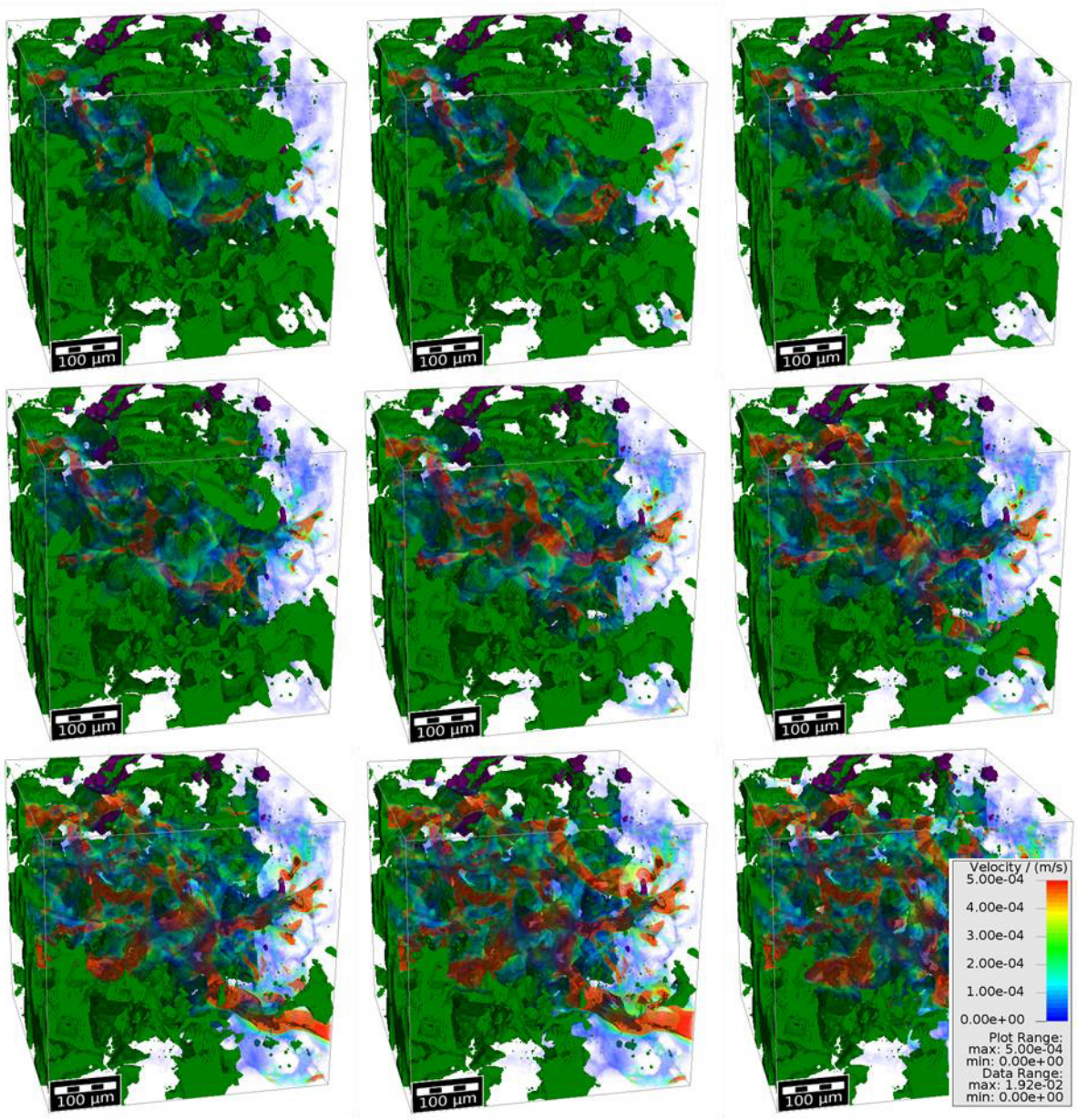

Fig. 43. Calcite pore cement and flow field development

The visualizations show from left to right and top to bottom the development of the green calcite pore cement distribution and the flow field with barite grains colored in purple. Images are shown at flow time intervals of 2 min ranging from 0 to 16 min with a maximum reaction time of 79 a. For automation and consistent settings, a Python macro script was employed to visualize the continuously changing flow fields with GeoDict. An animation for a reaction time of 82 a is available via Fig. 17.

Notably, 13,350 CPU hours were necessary for such a simulation run with up to $1.6 \cdot 10^7$ solution blobs moving in the 400^3 voxel space, while performing $5.9 \cdot 10^9$ single PhreeqC calls resulting in $1.2 \cdot 10^8$ individual calcite dissolution events at the sub-voxel scale (Table 17).

The thus induced continuous porosity increase effects the permeability development as shown in Fig. 44, but the relationship was intriguingly non-linear. Dissolution reactions in diffusion-

controlled sub-ROI regions of low local Péclet numbers had a negligible effect on the overall permeability evolution of the sandstone microstructure. While the porosity changes are directly linked to the reaction rate, the permeability change depends also on the local flow field. Jumps in the curve can be related to opening of flow paths during dissolution. Related to the reactive surface area determined from the 3D CT scan and multiplied by a factor of 20 to account for surface roughness, the average calcite reaction rate is determined at $1.5 \pm 0.6 \cdot 10^{-5}$ mol/m^{2}s. The rate curve in Fig. 44 shows a rather small scatter induced by local transport effects. Accordingly, dissolution reactions are dominantly controlled by kinetics at reactive surfaces.

Table 17. Kinetic calcite pore cement dissolution results – model 4

Up to 46,000 particles were simultaneously moving in the 400^3 ROI while representing a multiple amount of solution carriers up to three magnitudes higher, which results in a faster adaption of the pore fluid to the inflow fluid.

	t (flow) [min]	t (reaction) [a]	Total alteration [voxel]	Core hours [h]	Reactions	Particles (up to)	Particles represent
Model 4	45	222	$1.9 \cdot 10^5$	13,350	$5.9 \cdot 10^9$	$4.6 \cdot 10^4$	$1.6 \cdot 10^7$

The development of the Damköhler number with reaction time was calculated from the ratio of the calcite volume change including the alteration factor to the volume flow rate in flow direction (Fig. 45). The non-linear curve starts with a slight increase reflecting rather equivalent increases of the reaction rate and the velocity. After 7 min simulation time ($t_{reaction}$ = 33 a), the Damköhler curve starts to decrease monotonously up to three orders of magnitude at 45 min flow time ($t_{reaction}$ = 222 a), when the accessible calcite is nearly completely dissolved.

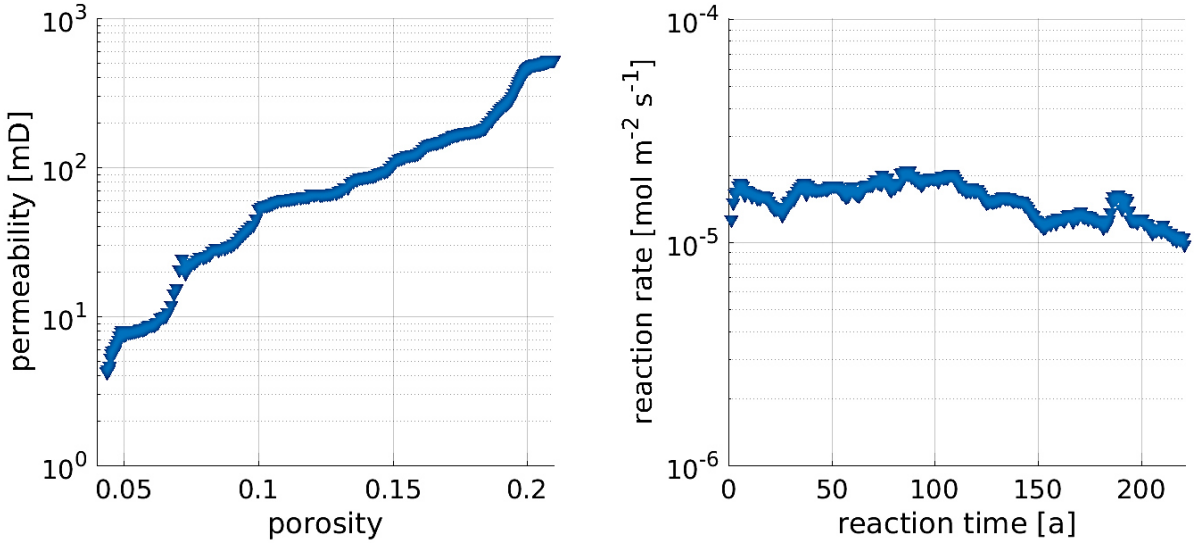

Fig. 44. Calcite pore cement dissolution results

The diagrams show the development of the porosity-permeability relationship (left) and the reaction rate (right) for the calcite cement dissolution in the sandstone matrix (Hinz et al., 2019).

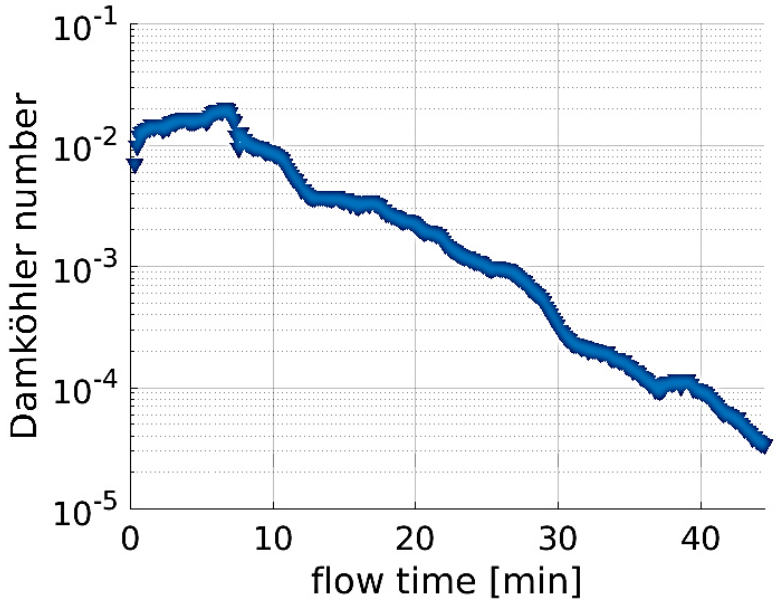

Fig. 45. Damköhler number development

The diagram shows the Damköhler number plotted versus the flow time. Once the peak is reached, the curve decreases up to three orders of magnitude.

5 Discussion

The code was continuously developed based on simulation results. Accordingly, results are discussed for limitations and disadvantages of applied code approaches. Necessary code adaptions are implicated, thus explaining the development of the presented algorithm. Calcite dissolution model results are classified concerning the dissolution regime. In addition, some results are compared with each other and the synthetic dissolution approach. The synthetic approach however shows disadvantages of the applied local flow resistivity calculations (Fig. 14) and thus implies the need for further improvements. For 2D models, Pape et al. (1982) introduced a pigeon hole model for relating permeability to specific surfaces. Latief et al. (2010) presented the 3D pigeon hole model capable of describing more complex structures. As an idea for future work, implementations of this model into reactive transport codes might be promising concerning local permeability calculations without the need of numerical approaches.

5.1 Celestite precipitation

The simulations can reproduce the development of a precipitation front at the center of the structure. The two precipitation mechanisms show a quite different behavior, which is highlighted by the visualization of 2D slices in Fig. 46. Visualizations are illustrated at the same slice and time. For model 1a, pathways between reservoirs are already restricted to porous voxels while model 1b still allows colloid transport at free, non-porous particle paths. Model 1b shows clogging of pore throats. At model 1a, the blocking of pathways is more related to the structure center no matter if there are pore throats or larger pores. In addition, the surface-related precipitation mechanism results in a significantly lower amount of porous voxels.

Though the precipitation front could be reproduced, there is a high discrepancy between the maximum amounts of precipitate in slices at this zone when comparing the experiment to the simulations. Considering the total length difference of 0.768 mm in the simulation to 50 mm in the experiment, it is clear that simulations cannot entirely reproduce the experimental results. This is especially true when concerning the temporal development and the additional precipitates in distance to the center. Restricting the precipitations to solid surfaces in model 1b clearly is more realistic than the approach of model 1a, but the model still needs the implementation of the nucleation theory. This could be realized with a probabilistic approach

that is also considering the mineral-specific nucleation kinetics (e.g., He et al., 1995). In addition, the rate of spontaneous precipitation of $SrSO_4$ might also be considerable. According to Yeboah et al. (1994), the precipitation rate depends from concentrations and ionic strength, which would need consideration for capturing experimental results at a greater extent. Slower precipitation kinetics have been observed by He et al. (2014) and might also contribute to close the gap between experiment and simulation. In contrast to the experiment of Chagneau et al. (2015), the simulation continued to precipitate celestite until all pathways between reservoirs are blocked. The consideration of reaction and nucleation kinetics could solve this discrepancy.

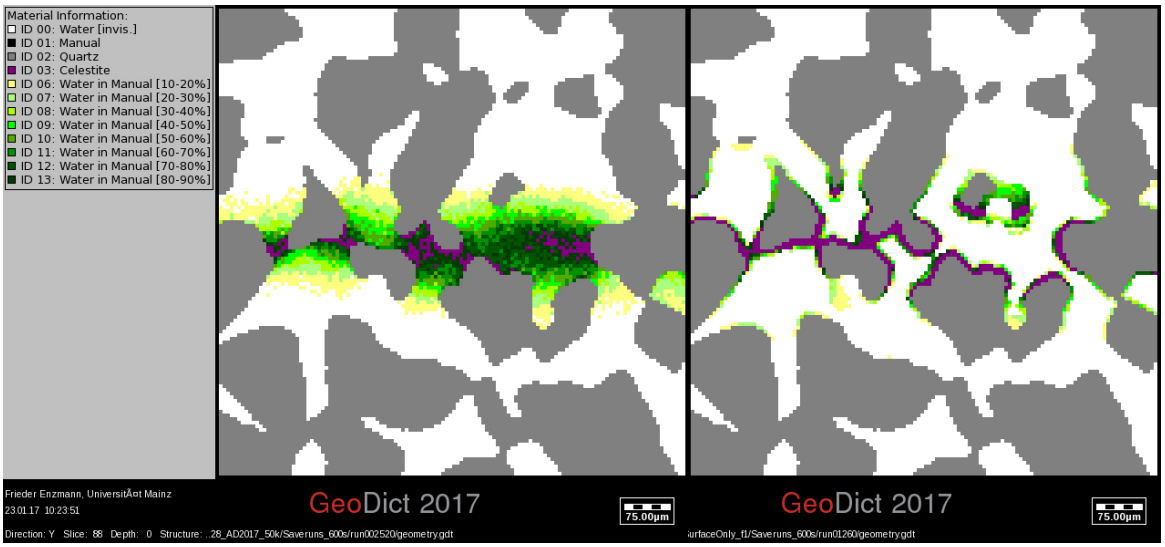

Fig. 46. 2D slices of different celestite precipitation mechanisms

The celestite precipitation patterns are illustrated from porous to solid voxels for the free precipitation of model 1a (left) and for the surface-related precipitation of model 1b (right).

Prasianakis et al. (2017) modeled celestite dissolution and subsequent barite precipitation according to the experiment performed by Poonoosamy et al. (2015). The classical nucleation theory was implemented in a modeling approach using the lattice Boltzman method. Thereby, the development of the system could be explained thus allowing for a general prediction under different conditions (Prasianakis et al., 2017). However, the pore-level modeling required a fitting of transport and kinetic parameters in order to reproduce the experimental results. The cross-scale modeling approach combines pore scale transport and sub-micron nucleation kinetics (Prasianakis et al., 2017) and thus offers great potential for increasing the capabilities of ReacDict in future code adjustments.

5.2 Halite precipitation

Both halite precipitation models show two intervals of steeper curves in the porosity-permeability plot (Fig. 22). These regions correlate well with the development of the first two layers of halite on the calcite grains. As shown in Fig. 14, the inaccuracy of the local flow resistivity in porous voxels results in permeability jumps. In models 2a and 2b, the underlying local permeability was calculated with the simplified cubic law (Fig. 14c) thus explaining the irregularities in curve steepness. Model 2a shows a steep decrease of permeability values starting from a porosity of 32 %. This correlates to the formation of a third halite layer and a subsequent clogging of pathways near the inflow region.

The permeability correlates with the flow velocity that is in turn used for the calculation of Damköhler numbers. Accordingly, the observations in Fig. 22 are also visible in the Da plot (Fig. 47).

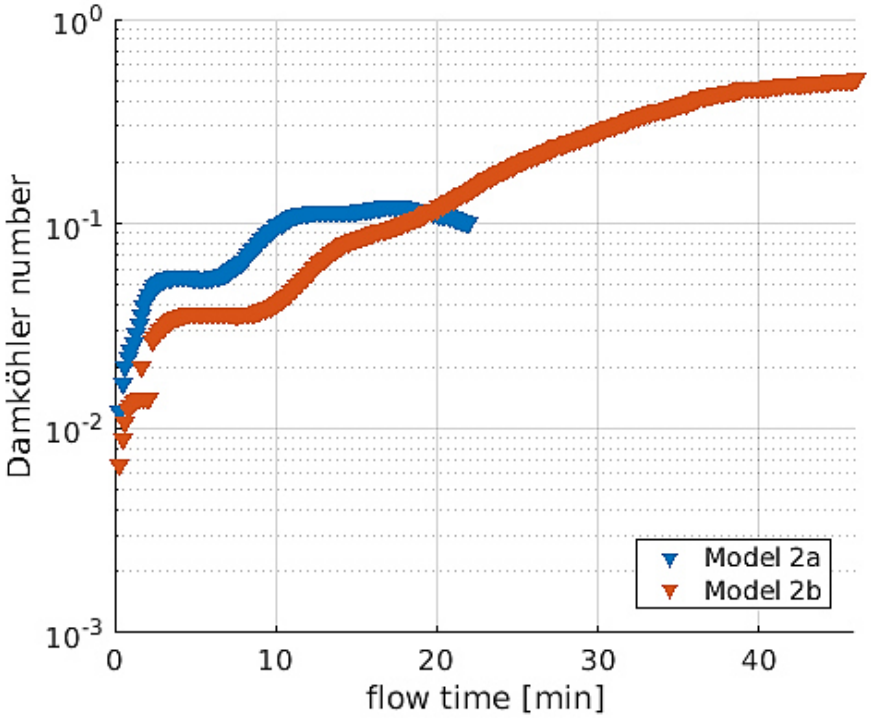

Fig. 47. Damköhler number plot – models 2a,b
The plot shows the development of the Damköhler numbers versus the flow time. Model 2b has an alteration factor of 10 and thus, the curves are comparable in shape, but not in time.

Model 2b shows a halite precipitation gradient (Fig. 25) with a lesser intensity compared to model 2a (Fig. 23). Accordingly, total porosity decreases have a comparably smaller impact on the permeability of the structure explaining the difference in permeability curve steepness at lower porosity (Fig. 22).

As shown in Fig. 24, the gradient of halite precipitates has a delay of a few voxels at the inflow region due to the region for placing new particles. Accordingly, this region was reduced to the inflow plane for models beyond 2c. However, particles might leave the ROI by this inflow plane, which has made the implementation of a solid barrier obligatory.

5.3 Calcite grain matrix dissolution

The various visualizations of model 2c data show continuous dissolutions at all calcite grains (e.g., Fig. 27). Fig. 28 shows the development of a solid fraction gradient in flow direction while Fig. 29 shows an increased dissolution rate at the center that is however specific for the chosen slice. A reaction front is not observable. According to 3D visualizations, the dissolution locations initially develop according to ramified wormholes. Once the injected acid reaches the outflow regions from the various pathways, the calcite grains dissolve homogeneously according to the uniform dissolution regime. An unambiguous classification of a dissolution regime is difficult, since the development of the rock-fluid system strongly depends from the pore scale structure and because the transitions from one regime to another are indistinct.

Once, particles reach the outflow region at approx. 2 minutes flow time, the Damköhler numbers in Fig. 48 show a monotonously decreasing curve. The values decrease up to two orders of magnitude. Considering and transforming the Da-related dissolution regimes (Maheshwari et al., 2013) to smaller Da values, Fig. 48 indicates a trend from wormholing towards uniform dissolution. In contrast, the permeability changes only by a factor of 5. Considering Eq. (16) and the proportionality of permeability and physical velocity, the reaction rate or ΔV_{phase} decreases significantly with simulation time as expectable from the continuously reducing grain surface area during ongoing dissolution reactions.

The minor drawback of the alteration factor is clearly visible in Fig. 48 showing the transport-related Da increase in the first minutes of flow time scaled to a few months in reaction time. Thus, reaching a steady state is not properly scalable with this approach and should be considered in reaction time results.

As discussed previously for models 2a and 2b, the particle handling of model 2c also has a drawback at the inflow region as visible in Fig. 28 and is thus taken care of for the following simulations.

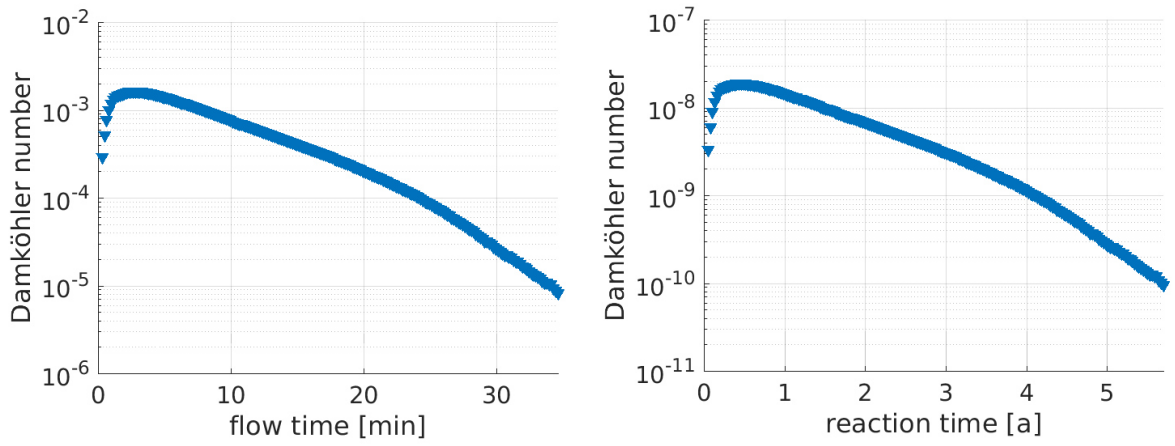

Fig. 48. Damköhler numbers – model 2c
The diagrams show the Da development in relation to flow (left) and reaction time (right).

The implementation of pore fluid tracking at the voxel scale has shown new visualization potential. However, the calcite distribution in Fig. 28 shows the problem of porous remains throughout the structure. The new capabilities thus imply new problematics that have to be taken care of. At first, the dissolution of porous voxels without any connected solids has been implemented and proven to work out at model 2d. For that matter, Fig. 34 shows an increase in permeability values up to three orders of magnitude. However, the face dissolution regime is quite favorable for validating that code adjustment. In addition, the geochemical calculation interval of model 2c was set relatively high. At an initial Pe of 50.1, advection is clearly dominating with an average velocity of $3.7 \cdot 10^{-4}$ m s^{-1} indicating a temporal resolution of 0.016 s instead of 0.1 s. At the suggested value, the solution carriers would move one voxel in average per sub-time step. In model 2d, that problem is avoided due to a decreased velocity.

5.4 Calcite solid matrix dissolution

The permeability increases by the factor of 2.5, which is rather low considering the porosity increase from 20-50 %. Several examinations were carried out in order to understand the discrepancy between expected and modeled values that occur despite the code adjustment concerning the dissolution of porous voxels. At first, the synthetic approach was used to see results for a homogeneous dissolution. Fig. 49 shows a slight comparability of simulated and synthetically produced porosity-permeability curves with respect to the shape. As expected, the permeability values differ widely.

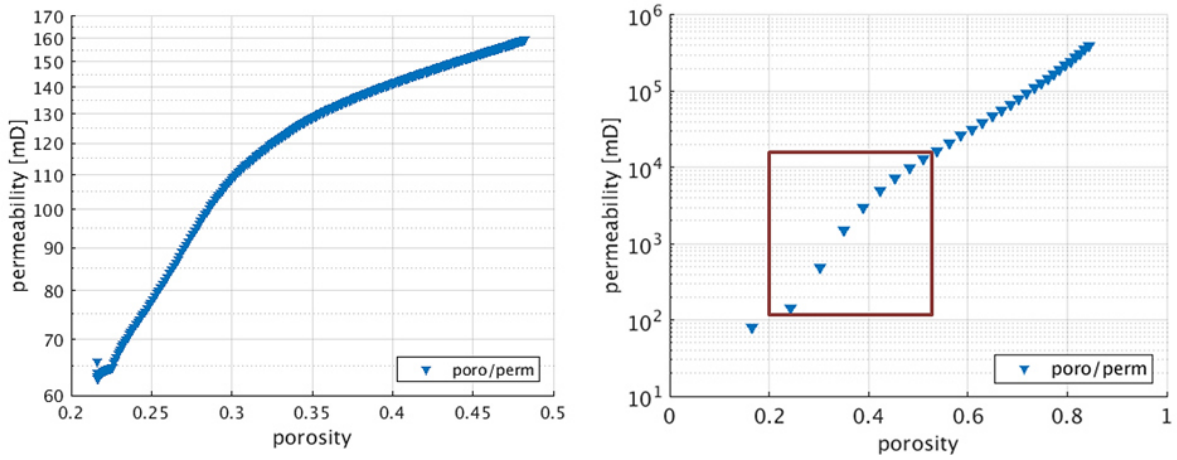

Fig. 49. Comparison of simulated and synthetic dissolution
The diagrams show the porosity-permeability development for the reactive transport simulation (left) and the synthetic approach (right). The red square frames the comparable porosity.

A permeability difference at the same total porosity can be related to a strong reactivity gradient along the flow axis. Fig. 50 shows that gradient, but also variations at inflow and outflow regions. At the inflow region, these variations are related to increased particle frequency due to the reflection of particles at a solid barrier and thus a slowdown of these. Accordingly, the acidic solutions have a higher probability to remain there and dissolve the calcite grain surfaces. At the outflow region, less particles (reduction of approx. 65%) are tracked. This is explainable by the relatively high geochemical calculation step of 50 ms in relation to the small voxel length of 0.7 µm and velocities above 500 µm s-1. As observed with previous simulation models, the discrepancy in porosity values near the outflow region strongly limits the computed permeability to smaller values. Considering the values, either the geochemical calculation interval should be reduced by a factor of at least 10 or the pressure gradient should be accordingly smaller to reduce the velocity.

Previously, porous voxels were another reason for reduced permeability values (Fig. 28). Examinations show that these porous voxels again occur significantly as visualized in Fig. 51. At previous small grain positions, porous voxels remain without being connected to any solid material. This effect crucially influences the computed hydromechanical transport parameters. Porous voxels appear also at larger grains and prevent faster flow at some pore throats. In addition, the closed pores material is observable in connection to the pore space. This interface should not occur, so the code has been updated accordingly.

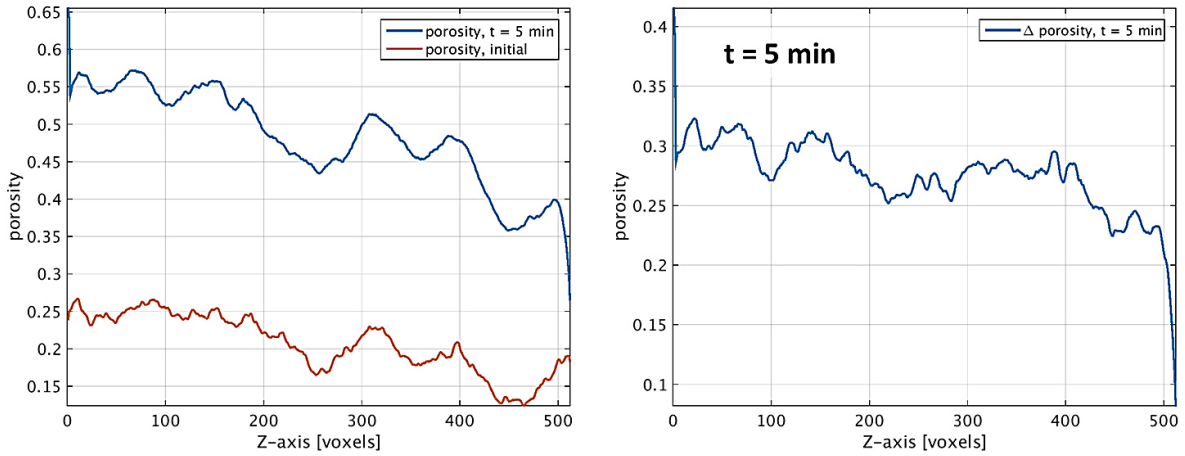

Fig. 50. Porosity results in flow direction in the Kreuznach structure

The porosity along the Z-axis is plotted in red for the initial geometry and in blue for the final geometry (left) at a flow time of 5 minutes ($t_{reaction}$ = 25 a). The difference between these two curves shows a slight gradient and strong effects at inflow and outflow region (right).

For a comparison, porous voxels and the closed pores material were transformed into new pore space without any flow restrictions. A permeability value of 16,332.1 mD results from the according flow field computation at a total porosity of 56.5 %. These values are in the range of the synthetic approach (Fig. 49). A slice is visualized with according flow field for both geometries with and without porous voxels and shows a velocity difference in the order of two magnitudes (Fig. 51). The minimum porosity perpendicular to the flow direction is 39 %, which is much greater than the values presented in Fig. 50. The two flow fields differ completely. Faster velocities are located partly at other regions and they diverge by two orders of magnitude.

The obtained insight was crucial to improve the quality of the later performed simulation of kinetic calcite pore cement dissolution. The code was adapted to prevent the existence of porous voxels unconnected to any solid by using a mechanical approach.

However, Singh et al. (2018) showed that both partially dissolved regions and sharp solid-pore interfaces may well develop during dissolution of carbonate rocks that contain intra-granular micro-porosity. By adapting the code, ReacDict either (1) dissolves unconnected porous voxels completely in a mechanical manner or (2) shows the tendency towards remaining clusters of porous remains that have a significant impact on the porosity and permeability. Thus, further research in this topic might increase the predictability of numerical models concerning the handling of surfaces.

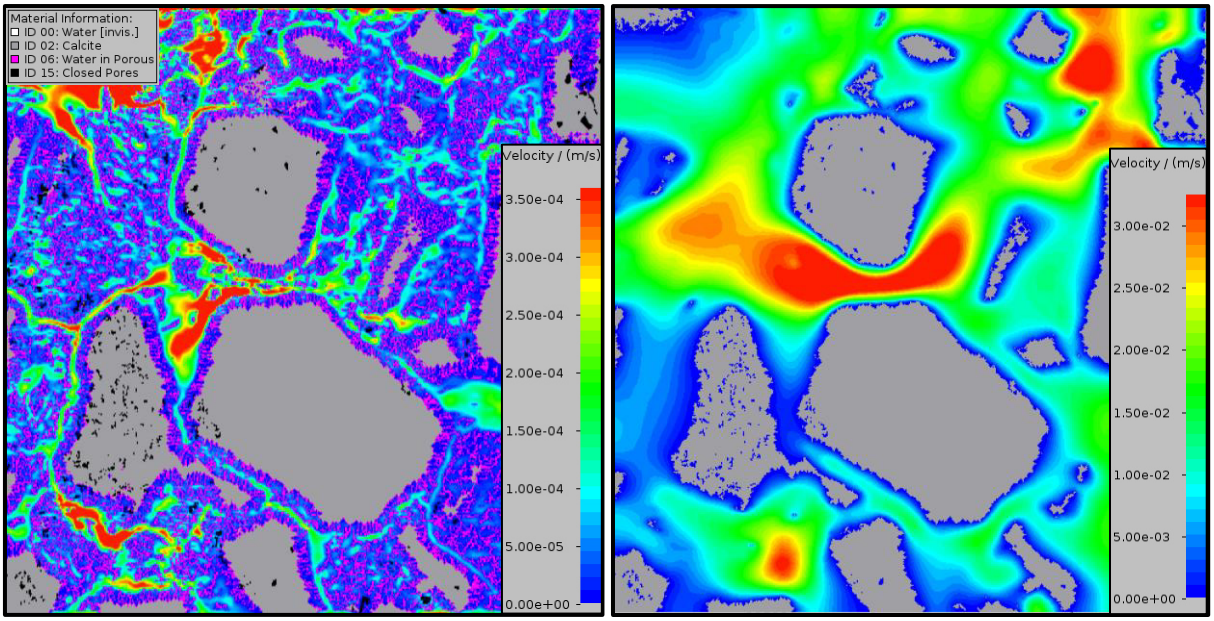

Fig. 51. Influence of porous voxels on the flow field in the Kreuznach structure

At previous calcite voxel positions still many porous remains are visible in purple (left). The rather significant influence on the flow field at the reaction time of 25 years is shown by comparison with a flow field computed without consideration of porous voxels (right). The 2D slices are connected to the visualizations in Fig. 38 and Fig. 39.

5.5 Calcite pore cement dissolution

According to the formulation of Da-related dissolution regimes (Maheshwari et al., 2013; Golfier et al., 2002), the Damköhler number plot (Fig. 45) shows various dissolution regimes. However, the proposed Da-relation is related to continuum models with a single mineral phase. The transformation of that proposition to pore scale models is a critical approach, since multiple dependencies have to be considered. Nevertheless, visualizations might indicate dissolution regimes while dynamic Da changes also imply changes for the dissolution regime. According to Menke et al. (2016), the visible dissolution regimes strongly depend from the structure especially in the applied heterogeneous system. It is thus more convenient to classify a dissolution regime from the development of the transport parameters in comparison to the synthetic approach.

At the first quarter of the simulation, the Da curve indicates dissolution in the canonical wormhole regime while diffusion is dominating the solute transport as expected. The curve then enters the wormholing regime and finally approaches uniform dissolution. In Fig. 52, the comparison with synthetic dissolution results supports these considerations. In general, the synthetic model follows uniform dissolution. Accordingly, wormhole formations principally

show a steeper increase of the porosity-permeability curve. In contrast, face dissolution results in a rather flat curve until the dissolution front reaches the outflow region. Consequently, the simulation results indicate dissolution according to a wormholing regime, which is already implicated by the visualizations in Fig. 43. However, the initially dominating flow path and the corresponding dissolution locations close to that path are also comparable to channeling (Menke et al., 2016). Thus, a distinction between canonical wormholes and channeling is rather difficult for the presented results.

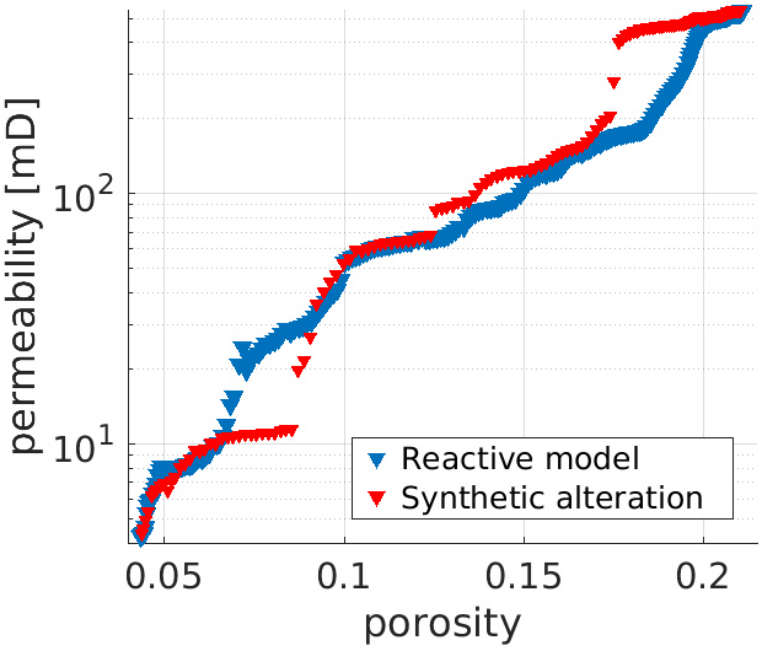

Fig. 52. Synthetic porosity-permeability plot – model 4
The diagram compares the developments of the hydromechanical transport parameters resulting from the reactive flow model and the synthetic alteration approach.

The synthetic porosity-permeability plot in Fig. 52 shows a good comparability to the reactive simulation. However, it does not correlate perfectly due to the different approach. In contrast to the reactive model, a few jumps in the permeability are observable with a factor of up to 2. The simulation results on the contrary show a relatively smooth increase in values. Nevertheless, the curves partly match exactly, and the final permeability is effectively equal thus validating the code adaptions related to mechanical dissolution.

Fig. 53 shows the calcite distribution at different reaction time intervals throughout the simulation. In comparison of the curves, a gradient appears showing higher amounts of dissolved calcite near the inflow area. Thus, the plot additionally validates the proposition of a wormholing regime at the beginning of the simulation. The comparison of the curves for

reaction times of 100-150 a indicates uniform dissolution, which is in contrast to the according Da numbers that imply the general wormholing regime before approaching the uniform dissolution. This supports the classification of dissolution according to channeling. At a reaction time of 150 a, accessible calcite is completely dissolved in the first two-fifths of the structure.

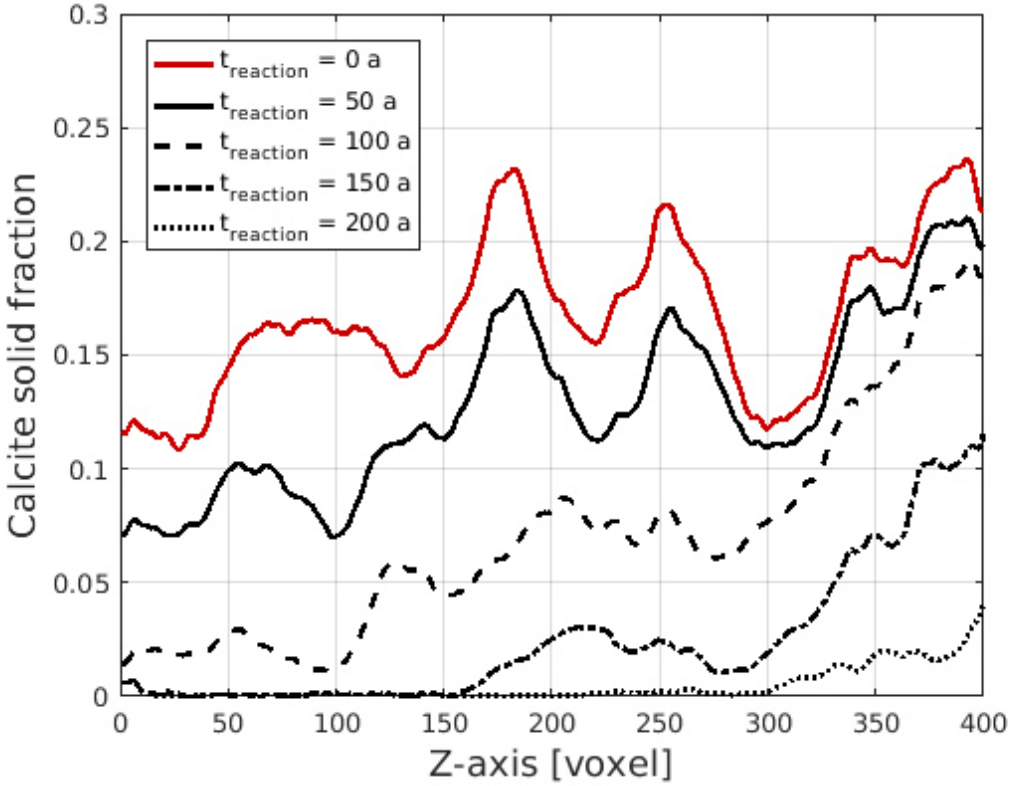

Fig. 53. Calcite distribution in flow direction – model 4
In reaction time intervals of 50 a, the calcite fraction is plotted along the flow direction. Onto 100 a of reaction time, a gradient develops showing a dissolution preference near the inflow region (left-hand boundary).

Dissolution throughout the structure is becoming incrementally homogeneous as Fig. 53 shows. Despite the simulation dynamics and even though the quartz matrix controls the accessibility of reactive calcite surfaces, the development of the structure can be determined to changing dissolution regimes. In addition to the plots of calcite distribution and Damköhler numbers (Fig. 45), that statement is supported by the 3D visualization of dissolved calcite voxels with a color gradient illustrating the relative time of dissolution (Fig. 54). The image shows a rather homogeneous calcite dissolution along the main flow path. This wormholing or channeling effect results in increased permeability values compared to uniform dissolution as illustrated in the left third of Fig. 52. At a reaction time of approx. 65 a, the previous dissolution region (blue colours in Fig. 54) has expanded to an extent rendering wormholing as being no more observable. Thus, when a porosity of 10 % is reached in approximation, the dissolution scheme

looks more uniform as observable e.g., in the diagram centre of Fig. 52. The accessible calcite areas are increasingly spread throughout the structure, so that dissolution appears more uniform with time.

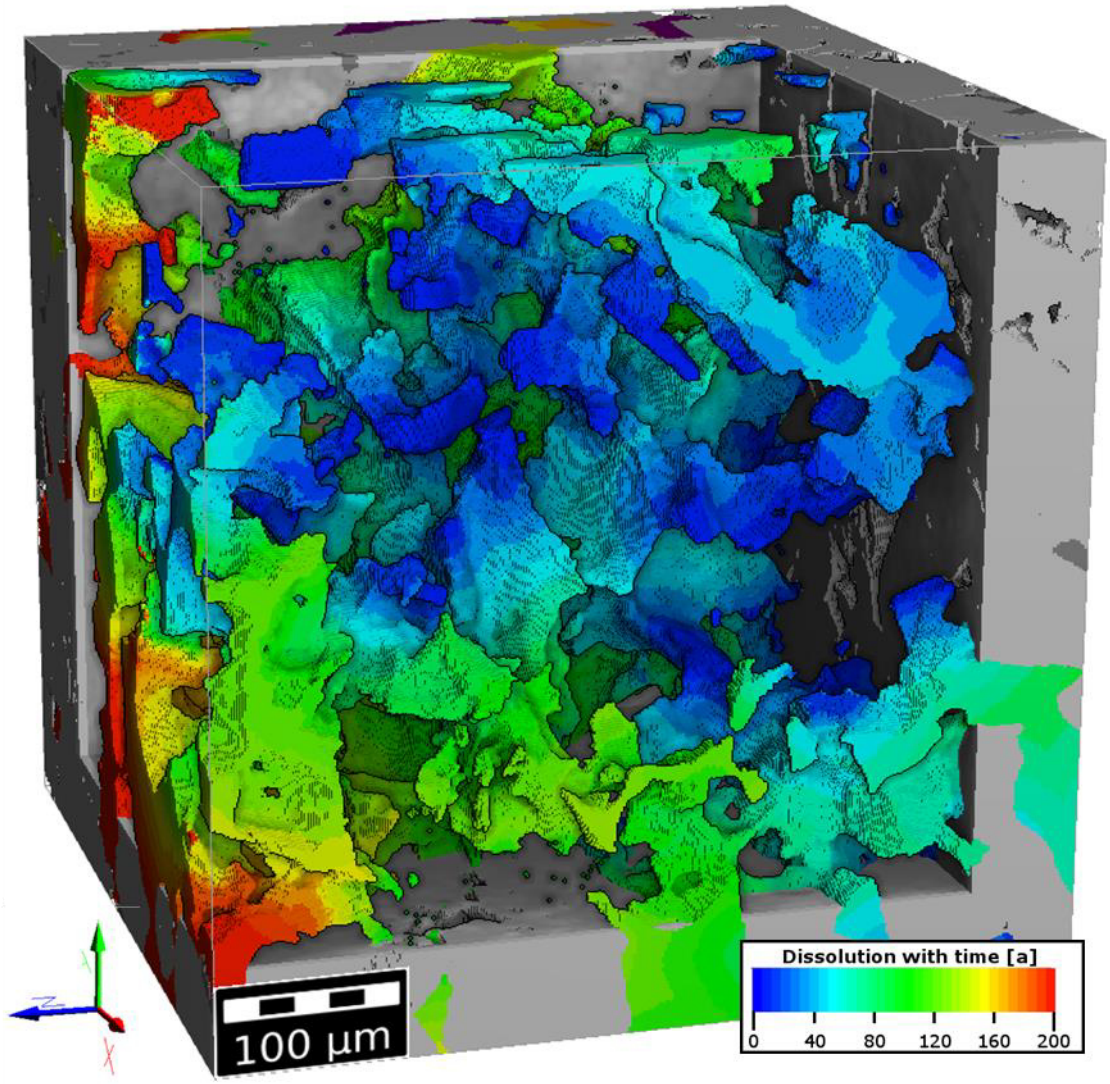

Fig. 54. 3D visualization of the time of dissolution
The image shows the dissolved calcite pore cements in colors from blue to red (see the color bar) indicating the time of dissolution with respect to the simulation begin. Inflow region is at the right-hand boundary.

In fact, the dissolution regimes of this simulation strongly depend from the accessibility of reactive surfaces. In this heterogeneous system, a regime is hard to tell just from visualization aspects. Clearly, a gradient develops at the beginning due to transport reasons and thus it appears like a canonical wormhole or channeling. After reaching a steady state in the pore fluid, the calcite dissolves homogeneously while inducing nonlinear permeability changes when opening certain flow paths. According to simulation results, it seems obvious that the

classification to dissolution regimes becomes rather obsolete when dissolving a non-dominating mineral phase in a heterogeneous geometry.

Fig. 53 and Fig. 54 imply delayed reactions at the outflow region. This effect is caused by both, transport and impeded accessibility due to an increased thickness of pore cements. In comparison to simulation results, the synthetic approach in Fig. 52 shows increased permeability values starting at a porosity of 17 %. Even though dissolution appears to be rather homogeneously distributed on the reactive surfaces, this discrepancy highlights the effect of transport on the results of the reactive transport simulation.

The results imply that the synthetic model is a potential substitution at a significantly reduced computational effort when expecting uniform dissolution throughout the entire simulation. Although Maheshwari et al. (2013) propose an estimation based on Damköhler numbers that concept is not directly transferrable to the pore scale as indicated by the presented results especially in presence of a strongly dominating flow path.

The reaction rate in Fig. 44 is higher by a factor of 15±6 than an experimentally obtained reaction rate for micritic calcite at $0.98 \pm 0.04 \cdot 10^{-6}$ mol/m^{2}s (Fischer et al., 2012), which is obviously due to the surface roughness factor of 20 taken into account. The discrepancy in reaction rates due to deviating concepts in reactive surface area assessment is known to be a critical point in experimental result interpretation (Fischer et al., 2012) and in comparison with numerical results (Haase et al., 2014).

6 Conclusion

This thesis presented a novel reactive fluids modeling approach coupling fluid dynamics and geochemical calculations. Reactive transport was realized by combining efficient modules of the GeoDict software package and the robust geochemical calculator IPhreeqc both embedded in an MPI-parallelized C++ script that was given the name ReacDict. The workflow comprises flow field computations, transport of virtual particles and kinetic geochemical equilibrium thermodynamics. This coupling was realized sequentially with the (Navier) Stokes-Brinkman equation, a Lagrangian transport approach and, principally, mineral-specific reaction rate equations that are interconnected with geochemical equilibrium thermodynamics. Simulations were performed in 3D voxel-geometries resulting in pore alterations at the sub-voxel scale. Voxel-related reaction calculations were performed at intervals smaller than the general time steps. Thus, the presented workflow offers a high temporal and spatial resolution in relation to the given µCT structures. Post-processing tools enable fast evaluation possibilities according to the DRP concept. For geochemically reactive systems, the development of the porosity-permeability relationship can automatically be obtained amongst other charts such as the development of Da or the reaction rate over simulation time.

Geochemical setups for celestite and halite equilibrium precipitation and kinetic calcite dissolution were simulated in different 3D geological geometries. The reaction locations depend from the geochemical transport and thus from the digital rock geometry. In contrast to a linear synthetic dissolution approach, the local reaction rates of the presented models may be strongly non-linear and imply different developments for the porosity-permeability relationship. Different input parameters showed significant differences in obtained results. Accordingly, it is difficult to choose suitable input parameters for the digital reactive flow experiments, which implies that the presented code is a tool for advanced geochemists. With adaptions of PhreeqC databases, the capabilities of the model may increase to an even wider range of reactive systems, especially when implementing kinetic rate laws for additional minerals.

The presented dissolution of specific components of a digital rock showed the incongruity with reactive flow models at the continuum scale and thus highlights the necessity of pore-scale reactive transport approaches. However, comparisons to experiments have yet to be performed in order to validate the reactive flow model. Nonetheless, the presented pore scale modeling

workflow offers promising potential and capabilities for the resimulation of experimental data or even the prediction of experimental results. Time-resolved hydromechanical transport parameters and reaction rates can thus be obtained directly from datasets of dynamic µCT studies.

7 Outlook

The description of more intuitive parameters and an increased support for geochemically unexperienced researchers and engineers is suggested as it might well accelerate the training curve of code users and thus a suitable handling of the reactive flow setup.

The workflow offers the possibility for reactive REV analyses. However, the definition of REVs for reactive fluid models and also the formulation of kinetic rate terms are limiting factors and require thus an increased focus in future research efforts.

At the sub-micron scale, heterogeneous surface reactions (Fischer et al., 2012) and nucleation kinetics (Prasianakis et al., 2017) as well as sorption processes and initial microporosity are potentially useful and necessary implementations for the model. Reactive flow models thus require a multi-scale approach to describe a maximum number of hydrogeochemical systems.

Runtime improvements and up-to-date high-performance computer systems are required to increase the code efficiency so that common structure sizes of 1024^3 or even 2048^3 voxels may be considered at reactive flow simulations with suitable runtimes. Dynamic adjustments of runtime-crucial parameters and a higher flexibility of data distribution onto more parallel processes are possibilities to further improve the code performance. In general, advancements in flow solvers efficiency and geochemical codes with machine learning approaches (e.g., Leal et al., 2014) reduce the computational cost of reactive transport models at the pore-scale and are thus a well-invested effort for increasing the efficiency of reactive flow approaches.

The effort of realizing a multi-scale approach directly coupling pore scale results to field scale models, directly leads to economic fields of application such as EOR and further borehole topics. This thesis provides an indispensable contribution to this applicability.

References

ANDRÄ, H., Combaret, N., Dvorkin, J., Glatt, E., Han, J., Kabel, M., Keehm, Y., Krzikalla, F., Lee, M., Madonna, C., Marsh, M., Mukerji, T., Saenger, E.H., Sain, R., Saxena, N., Ricker, S., Wiegmann, A., Zhan, X. 2013a. Digital rock physics benchmarks – Part I: Imaging and segmentation. Computers & Geosciences 50, 25-32, doi: 10.1016/j.cageo.2012.09.005

ANDRÄ, H., Combaret, N., Dvorkin, J., Glatt, E., Han, J., Kabel, M., Keehm, Y., Krzikalla, F., Lee, M., Madonna, C., Marsh, M., Mukerji, T., Saenger, E.H., Sain, R., Saxena, N., Ricker, S., Wiegmann, A., Zhan, X. 2013b. Digital rock physics benchmarks – part II: Computing effective properties. Computers & Geosciences 50, 33-43, doi: 10.1016/j.cageo.2012.09.008

APPELO, C.A.J. 2015. Principles, caveats and improvements in databases for calculating hydrogeochemical reactions in saline waters from 0 to 200 °C and 1 to 1000 atm. Applied Geochemistry 55, 62-71, doi: 10.1016/j.apgeochem.2014.11.007

BARTELS, W.-B., Rücker, M., Berg, S., Mahani, H., Georgiadis, A., Fadili, A., Brussee, N., Coorn, A., van der Linde, H., **Hinz, C.**, Jacob, A., Wagner, C., Henkel, S., Enzmann, F., Bonnin, A., Stampanoni, M., Ott, H., Blunt, M., Hassanizadeh, S.M. 2017. Fast X-Ray Micro-CT Study of the Impact of Brine Salinity on the Pore-Scale Fluid Distribution During Waterflooding. Petrophysics 58, 36-47, ISSN 1529-9074

BEAR, J. 1972. Dynamics of Fluids in Porous Media. American Elsevier Publishing Company, New York, 764 p.

BEAR, J., Cheng, A.H.-D. 2010. Modeling groundwater flow and contaminant transport. Springer, Dordrecht, 834 p.

BENSON, D.A., Aquino, T., Bolster, D., Engdahl, N., Henri, C.V., Fernàndez-Garcia, D. 2017. A comparison of Eulerian and Lagrangian transport and non-linear reaction algorithms. Advances in Water Resources 99, 15-37, doi: 10.1016/j.advwatres.2016.11.003

BLUNT, M.J., Bijeljic, B., Dong, H., Gharbi, O., Iglauer, S., Mostaghimi, P., Paluszny, A., Pentland, C. 2013. Pore-scale imaging and modelling. Advances in Water Resources 51, 197-216, doi: 10.1016/j.advwatres.2012.03.003

BONTE, M, Stuyfzand, P.J., van Breukelen, B.M. 2014. Reactive Transport Modeling of Thermal Column Experiments to Investigate the Impacts of Aquifer Thermal Energy Storage on Groundwater Quality. Environ. Sci. Technol. 48 (20), 12099-12107, doi: 10.1021/es502477m

BUADES, A., Coll, B., Morel, J.M. 2005. A non-local algorithm for image denoising. Proceedings of the 2005 IEEE Computer Society Conference on Computer Vision and Pattern Recognition, Vol. 2, 60-65, doi: 10.1109/CVPR.2005.38

CARMAN, P.C. 1937. Fluid flow through granular beds. Transactions, Institution of Chemical Engineers, London, 15, 150-166

CHAGNEAU, A., Claret, F., Enzmann, F., Kersten, Heck, S., M., Madé, B., Schäfer, T. 2015. Mineral precipitation-induced porosity reduction and its effect on transport parameters in diffusion-controlled porous media. Geochem Trans. 16:13, doi: 10.1186/s12932-015-0027-z

CHAUHAN, S., Sell, K., Enzmann, F., Rühaak, W., Wille, T., Sass, I., Kersten, M. 2018. CobWeb — a toolbox for automatic tomographic image analysis based on machine learning techniques: application and examples. arXiv: 1803.11046

CNUDDE, V., Silversmit, G., Boone, M., Dewanckele, J., De Samber, B., Schoonjans, T., Van Loo, D., De Witte, Y., Elburg, M., Vincze, L., Van Hoorebeke, L., Jacobs, P. 2009. Multi-disciplinary characterisation of a sandstone surface crust. Science of the Total Environment, 407 (20), 5417-5427, doi: 10.1016/j.scitotenv.2009.06.040

CNUDDE, V., Boone, M.N. 2013. High-resolution X-ray computed tomography in geosciences: A review of the current technology and applications. Earth-Science Reviews 123, 1-17, doi: 10.1016/j.earscirev.2013.04.003

CUNNINGHAM, E. 1910. On the velocity of steady fall of spherical particles through fluid medium (Published Conference Proceedings style). In Proc. Royal Soc. (London) A, vol. 83, 357-365

CVJETKOVIC, T., Schwarz, J.-O., Cheng, L., Becker, J., Linden, S., Wiegmann, A. 2018. Simulation of Reactive Transport Processes: Acidizing Treatments in Carbonate Reservoirs. Oil Gas European Magazine 44 (4), 190-193, doi: 10.19225/181204

DRIEßEN, J., Schöttler, M., Enzmann, F., Lakdawala, Z., Steiner, K., Popov, P., Iliev, O., Drews, M., Wieber, G., Kersten, M. 2015. Grundwasser 20 (3), 181-195, doi: 10.1007/s00767-015-0291-y

DVORKIN, J., Derzhi, N., Diaz, E., Fang, Q. 2011. Relevance of computational rock physics. GEOPHYSICS 76-5, E141-E153, doi: 10.1190/geo2010-0352.1

EINSTEIN, A. 1905. Über die von der molekularkinetischen Theorie der Wärme geforderte Bewegung von in ruhenden Flüssigkeiten suspendierten Teilchen. Annalen der Physik (in German). 322 (8), 549-560. doi: 10.1002/andp.19053220806

FELDKAMP, L.A., Davis, L.C., Kress, J.W. 1984. Practical cone-beam algorithm. Journal of the Optical Society of America. A, 1 (6), 612-619, doi: 10.1364/JOSAA.1.000612

FISCHER, C., Arvidson, R.S., Lüttge, A. 2012. How predictable are dissolution rates of crystalline material? Geochim Cosmochim Acta 98, 177-185, doi: 10.1016/j.gca.2012.09.011

FLESCH, S., Pudlo, D., Albrecht, D., Jacob, A., Enzmann, F. 2018. Hydrogen underground storage – Petrographic and petrophysical variations in reservoir sandstones from laboratory experiments under simulated reservoir conditions. International Journal of Hydrogen Energy 43 (45), 20822-20835, doi: 10.1016/j.ijhydene.2018.09.112

GAO, J., Xing, H., Tian, Z., Pearce, J.K., Sedek, M., Golding, S.D., Rudolph, V. 2017. Reactive transport in porous media for CO2 sequestration: Pore scale modeling using the lattice Boltzmann method. Computers & Geosciences 98, 9-20, ISSN 0098-3004, doi: 10.1016/j.cageo.2016.09.008

GLATT, E., Huber, F., Enzmann, F., Schaefer, T., Wiegmann, A. 2015. GeoDict Case Study – Nanoparticle migration in a natural granite fracture. Math2Market GmbH, Kaiserslautern. http://www.geodict.com

GOLFIER, F., Zarcone, C., Bazin, B., Lenormand, R., Lasseux, D., Quintard, M. 2002. On the ability of a Darcy-scale model to capture wormhole formation during the dissolution of a porous medium. J. Fluid Mech. 457, 213-254, doi: 10.1017/S0022112002007735

GUARRACINO, L., Rotting, T., Carrera, J. 2014. A fractal model to describe the evolution of multiphase flow properties during mineral dissolution. Advances in Water Resources 67, 78-86, doi: 10.1016/j.advwatres.2014.02.011

ENZMANN, F. 2000. Dissertation: Modellierung von Porenraumgeometrien und Transport in korngestützten porösen Medien. University of Mainz, Institute for Geosciences. 114 p., http://archimed.uni-mainz.de/pub/2000/0093/diss.pdf

HAGEMANN, B. 2018. Numerical and Analytical Modeling of Gas Mixing and Bio-Reactive Transport during Underground Hydrogen Storage. Cuvillier Verlag, Göttingen, 254 p., ISBN-13: 978-3-73699-714-1

HAMMOND, G.E., Lichtner, P.C., Lu, C., Mills, R.T. 2012. Pflotran: Reactive flow and transport code for use on laptops to leadership-class supercomputers. In: Groundwater Reactive Transport Models. F. Zhang, G.-T. Yeh, and J.C. Parker (eds.), Bentham Science, 141-159

HAYES, K.F., Redden, G., Ela, W., Leckie, J.O. 1991. Surface Complexation Models: An Evaluation of Model Parameter Estimation Using FITEQL and Oxide Mineral Titration Data. Journal of Colloid and Interface Science 142 (2), 448-469, doi: 10.1016/0021-9797(91)90075-J

HE, C., Li, M., Liu, W., Barbot, E. 2014. Kinetics and Equilibrium of Barium and Strontium Sulfate Formation in Marcellus Shale Flowback Water. Journal of Environmental Engineering 140 (5), doi: 10.1061/(ASCE)EE.1943-7870.0000807

HE, S., Oddo, J.E., Tomson, M.B. 1995. The Nucleation Kinetics of Strontium Sulfate in NaCl Solutions up to 6 m and 90°C with or without Inhibitors. Journal of colloid and interface science 174, 327-335, doi: 10.1006/jcis.1995.1398

HINZ, C., Enzmann, F., Kersten, M. 2019. Pore scale modelling of calcite cement dissolution in a reservoir sandstone matrix. E3S Web of Conferences 98, 05010, doi: 10.1051/e3sconf/20199805010

HÖLTING, B., Coldewey, W.G. 2005. Hydrogeologie. Einführung in die Allgemeine und Angewandte Hydrogeologie. Elsevier GmbH, München, 6th edition, 326 p.

HUNTER, R. J., 1981. Zeta Potential in Colloid Science. Academic Press, New York, 386 p., doi: 10.1016/C2013-0-07389-6

IASSONOV, P., Gebrenegus, T., Tuller, M. 2009. Segmentation of X-ray computed tomography images of porous materials: a crucial step for characterization and quantitative analysis of pore structures. Water Resour. Res. 45, W09415, doi: 10.1029/2009WR008087

ILIEV, O., Lakdawala, Z., Neßler, K.H., Prill, T., Vutov, Y., Yang, Y., Yao, J. 2017. On the Pore-Scale Modeling and Simulation of Reactive Transport in 3D Geometries. Mathematical Modelling and Analysis 22 (5), 671-694, doi: 10.3846/13926292.2017.1356759

JACOB, A., Enzmann, F., **Hinz, C.**, Kersten, M. 2019. Analysis of variance of porosity and heterogeneity of permeability at the pore scale. Transport in porous media, submitted

KOCH, A., Raven, C., Spanne, P., Snigirev, A. 1998. X-ray imaging with submicrometer resolution employing transparent luminescent screens. Journal of the Optical Society of America. A, Optics and Image Science 15 (7), 1940–1951, doi: 10.1364/JOSAA.15.001940

KOLDITZ, O., Bauer, S., Bilke, L., Böttcher, N., Delfs, J.O., Fischer, T., Görke, U.J., Kalbacher, T., Kosakowski, G., McDermott, C.I., Park, C.H., Radu, F., Rink, K., Shao, H., Shao, H.B., Sun, F., Sun, Y.Y., Singh, A.K., Taron, J., Walther, M., Wang, W., Watanabe, N., Wu, N., Xie, M., Xu, W., Zehner, B. 2012. OpenGeoSys: an open-source initiative for numerical simulation of thermo-hydro-mechanical/chemical (THM/C) processes in porous media. Environ. Earth Sci., 67 (2), 589-599, doi: 10.1007/s12665-012-1546-x

KOZENY, J. 1927. Über kapillare Leitung des Wassers im Boden. Sitzungsber Akad. Wiss., Wien, 136 (2a), 271-306

KULIK, D.A., Wagner, T., Dmytrieva, S.V., Kosakowski, G., Hingerl, F.F., Chudnenko, K.V., Berner, U. 2013. GEM-Selektor geochemical modeling package: revised algorithm and GEMS3K numerical kernel for coupled simulation codes. Computational Geosciences 17, 1-24, doi: 10.1007/s10596-012-9310-6

LATIEF, F.D.E., Fauzi U., Bijaksana, S., Bindar, Y. 2010. Pore structure characterization of 3D random pigeon hole rock models. International Journal of Rock Mechanics & Mining Sciences 47, 523-531, doi: 10.1016/j.ijrmms.2009.12.013

LAVENDA, B.H. 1985. Nonequilibrium Statistical Thermodynamics. John Wiley & Sons Inc., Chichester, 200 p.

LAUW, Y., Horne, M.D., Rodopoulos, T., Nelson, A., Leermakers, F.A.M. 2010. Electrical Double-Layer Capacitance in Room Temperature Ionic Liquids: Ion-Size and Specific Adsorption Effects. J. Phys. Chem. B 114 (34), 11149-11154, doi: 10.1021/jp105317e

LEAL, A.M.M., Blunt, M.J., LaForce, T.C. 2014. Efficient chemical equilibrium calculations for geochemical speciation and reactive transport modelling. Geochimica et Cosmochimica Acta 131, 301-322, doi: 10.1016/j.gca.2014.01.038

LEAL, A.M.M., Blunt, M.J., LaForce, T.C. 2015. A chemical kinetics algorithm for geochemical modelling. Applied Geochemistry 55, 46-61, doi: 10.1016/j.apgeochem.2014.09.020

LEAL, A.M.M., Kulik, D.A., Smith, W.R., Saar, M.O. 2017. An overview of computational methods for chemical equilibrium and kinetic calculations for geochemical and reactive transport modeling. Pure and Applied Chemistry 89 (5), 597-643, doi: 10.1515/pac-2016-1107

LEU, L., Berg, S., Enzmann, F., Armstrong, R.T., Kersten, M. 2014. Fast X-ray Micro-Tomography of Multiphase Flow in Berea Sandstone: A Sensitivity Study on Image Processing. Transp. Porous Med. 105, 451–469, doi: 10.1007/s11242-014-0378-4

LICHTNER, P.C., Kang, Q. 2007. Upscaling pore-scale reactive transport equations using a multiscale continuum formulation. Water Resour. Res. 43, W12S15, doi: 10.1029/2006WR005664

LINDEN, S., Hagen, H., Wiegmann, A. 2014. The LIR Space Partitioning System Applied to Cartesian Grids. In: Floater, M., Lyche, T., Mazure, M.L., Mørken, K., Schumaker, L.L. (eds). Mathematical Methods for Curves and Surfaces. MMCS 2012. Lecture Notes in Computer Science, vol 8177. Springer, Berlin, Heidelberg, doi: 10.1007/978-3-642-54382-1_19

LINDEN, S., Wiegmann, A., Hagen, H. 2015. The LIR space partitioning system applied to the Stokes equations. Graphical Models, 82, 58-66, doi: 10.1016/j.gmod.2015.06.003

LOTHENBACH B., Kulik, D., Matschei, D., Balonis, M., Baquerizo, L., Dilnesa, B., Miron, G.D., Myers, R.J. 2019. Cemdata18: A chemical thermodynamic database for hydrated Portland cements and alkali-activated materials. Cement and Concrete Research 115, 472-506, doi: 10.1016/j.cemconres.2018.04.018

LOTHENBACH B., Matschei T., Möschner G., Glasser F. 2008. Thermodynamic modelling of the effect of temperature on the hydration and porosity of Portland cement. Cement and Concrete Research 38 (1), 1-18, doi: 10.1016/j.cemconres.2007.08.017

LOTHENBACH B., Winnefeld F. 2006. Thermodynamic modelling of the hydration of Portland cement, Cement and Concrete Research 36 (2), 209-226, doi: 10.1016/j.cemconres.2005.03.001

MAES, J., Geiger, S. 2018. Direct pore-scale reactive transport modelling of dynamic wettability changes induced by surface complexation. Advances in Water Resources 111, 6-19, doi: 10.1016/j.advwatres.2017.10.032

MAHESHWARI, P., Ratnakar, R.R., Kalia N., Balakotaiah V. 2013. 3-D simulation and analysis of reactive dissolution and wormhole formation in carbonate rocks. Chemical Engineering Science 90, 258-274, doi: 10.1016/j.ces.2012.12.032

MARONE, F., Stampanoni, M. 2012. Regridding reconstruction algorithm for real-time tomographic imaging. J Synchrotron Radiat 19 (6), 1029-1037, doi: 10.1107/S0909049512032864

MATSCHEI T., Lothenbach B., Glasser F. 2007. Thermodynamic properties of Portland cement hydrates in the system CaO-Al2O3-SiO2-CaSO4-CaCO3-H2O, Cement and Concrete Research 37 (10), 1379-1410, doi: 10.1016/j.cemconres.2007.06.002

MENKE, H.P., Bijeljic, B., Andrew, M.G., Blunt, M.J. 2015. Dynamic three-dimensional pore-scale imaging of reaction in a carbonate at reservoir conditions, Environ. Sci. Technol., 49 (7), 4407-4414, doi: 10.1021/es505789f.

MENKE, H., Andrew, M.G., Blunt, M.J., Bijeljic, B. 2016. Reservoir condition imaging of reactive transport in heterogeneous carbonates using fast synchrotron tomography – Effect of initial pore structure and flow conditions. Chemical Geology 428, 15–26, doi: 10.1016/j.chemgeo.2016.02.030

MENKE, H., Bijeljic, B., Blunt, M.J. 2017. Dynamic reservoir-condition microtomography of reactive transport in complex carbonates: Effect of initial pore structure and initial brine pH. Geochimica et Cosmochimica Acta 204, 267-285, doi: 10.1016/j.gca.2017.01.053

MENKE, H., Reynolds, C.A., Andrew, M.G., Pereira Nunes, J.P., Bijeljic, B., Blunt, M.J. 2018. 4D multi-scale imaging of reactive flow in carbonates: Assessing the impact of heterogeneity on dissolution regimes using streamlines at multiple length scales. Chemical Geology 481, 27-37, doi: 10.1016/j.chemgeo.2018.01.016

NARDI, A., Idiart, A., Trinchero, P., deVries, L.M., Molinero, J. 2014. Interface COMSOL-PHREEQC (iCP), an efficient numerical framework for the solution of coupled multiphysics and geochemistry. Computers & Geosciences 69, 10-21, doi: 10.1016/j.cageo.2014.04.011

NOIRIEL, C., Madé, B., Gouze, P. 2007. Impact of coating development on the hydraulic and transport properties in argillaceous limestone fracture. Water Resour. Res. 43, W09406, doi:10.1029/2006WR005379

NOROUZI RAD, M., Shokri, N., Sahimi, M. 2013. Pore-scale dynamics of salt precipitation in drying porous media. Physical Review E 88, 032404, doi: 10.1103/PhysRevE.88.032404

PEREIRA NUNES, J.P., Blunt, M.J., Bijeljic, B. 2016. Pore-scale simulation of carbonate dissolution in micro-CT images, J. Geophys. Res. Solid Earth 121, 558-576, doi: 10.1002/2015JB012117.

PAPE, H., Riepe, L., Schopper, J.R. 1982. A Pigeon-hole Model For Relating Permeability To Specific Surface. Society of Petrophysicists and Well-Log Analysts, The Log Analyst 23, ISSN 0024-581X

PARKHURST, D.L., Appelo, C.A.J. 1999. User's guide to PHREEQC (version 2)—A computer program for speciation, batch-reaction, one-dimensional transport, and inverse geochemical calculations. Water-Resources Investigations Report 99-4259, 326 p., doi: 10.3133/wri994259

PARKHURST, D.L., Appelo, C.A.J. 2013. Description of input and examples for PHREEQC version 3—A computer program for speciation, batch-reaction, one-dimensional transport, and inverse geochemical calculations. U.S. Geological Survey Techniques and Methods, book 6, chap. A43, 497 p., doi: 10.3133/tm6A43

PARKHURST, D.L., Wissmeier, L. 2015. PhreeqcRM: A reaction module for transport simulators based on the geochemical model PHREEQC. Advances in Water Resources 83, 176-189, doi: 10.1016/j.advwatres.2015.06.001

POONOOSAMY, J., Kosakowski, G., Van Loon, L.R., Mäder, U. 2015. Dissolution–precipitation processes in tank experiments for testing numerical models for reactive transport calculations: Experiments and modelling. Journal of Contaminant Hydrology 177-178, 1-17, doi: 10.1016/j.jconhyd.2015.02.007

PRASIANAKIS, N.I., Curti, E., Kosakowski, G., Poonoosamy, J., Churakov, S.V. 2017. Deciphering pore-level precipitation mechanisms. Scientific Reportsvolume 7, 13765, doi: 10.1038/s41598-017-14142-0

PROMMER, H., Post, V.E.A. 2010. PHT3D, A Reactive multicomponent transport model for saturated porous media. User'sManual v2.10. http://www.pht3d.org

SAENGER, E.H., Enzmann, F., Keehm, Y., Steeb, H. 2011. Digital rock physics: Effect of fluid viscosity on effective elastic properties. J. Appl. Geophys. 74, 236-241, doi: 10.1016/j.jappgeo.2011.06.001

SAXENA, N., Hofmann, R., Alpak, F.O., Berg, S., Dietderich, J., Agarwal, U., Tandon, K., Hunter, S., Freeman, J., Wilson, O.B. 2017. References and benchmarks for pore-scale flow simulated using

micro-CT images of porous media and digital rocks. Advances in Water Resources 109, 211-235, doi: 10.1016/j.advwatres.2017.09.007

SCHWARZ, J.-O., Enzmann, F. 2012. Simulation of Fluid Flow on Fractures and Implications for Reactive Transport Simulations. Transport in Porous Media 96 (3), 501-525, doi: 10.1007/s11242-012-0103-0

SELL, K., Enzmann, F., Kersten, M., Spangenberg, E. 2013. Microtomographic Quantification of Hydraulic Clay Mineral Displacement Effects During a CO2 Sequestration Experiment with Saline Aquifer Sandstone. Environ. Sci. Technol. 47, 198-204, doi: 10.1021/es3013358

SINGH, K., Anabaraonye, B.U., Blunt, M.J., Crawshaw, J. 2018. Partial dissolution of carbonate rock grains during reactive CO_2-saturated brine injection under reservoir conditions. Advances in Water Resources 122, 27-36, doi: 10.1016/j.advwatres.2018.09.005

SMOLUCHOWSKI, M. 1906. O średniej drodze cząsteczek gazu i o związku jej z teoryą dyfuzyi (Sur le chemin moyen parcouru par les molécules d'un gaz et sur son rapport avec la théorie de la diffusion). Mémoire présenté par M. Lad. Natanson, m. t.. Bulletin International de l'Academie des Sciences de Cracovie, 202-213

STEEFEL, C. I. and Lasaga, A.C. 1994. A coupled model for transport of multiple chemical species and kinetic precipitation/dissolution reactions with application to reactive flow in single phase hydrothermal systems. Am. J. Sci. 294, 529-592, doi: 10.2475/ajs.294.5.529

STEEFEL, C.I., DePaolo, D.J., Lichtner, P.C. 2005. Reactive transport modeling: An essential tool and a new research approach for the Earth sciences. Earth and Planetary Science Letters 240, 539-558

STEEFEL, C.I., Appelo, C.A.J., Arora, B., Jacques, D., Kalbacher, T., Kolditz, O., Lagneau, V., Lichtner, P.C., Mayer, K.U., Meeussen, J.C.L., Molins, S., Moulton, D., Shao, H., Šimůnek, J., Spycher, N., Yabusaki, S.B., Yeh, G.T. 2015. Reactive transport codes for subsurface environmental simulation. Computational Geosciences 19 (3), 445-478, doi: 10.1007/s10596-014-9443-x

STOLL, M., Huber, F.M., Trumm, M., Enzmann, F., Meinel, D., Wenka, A., Schill, E., Schäfer, T. 2018. Experimental and numerical investigations on the effect of fracture geometry and fracture aperture distribution on flow and solute transport in natural fractures. Journal of Contaminant Hydrology, doi: 10.1016/j.jconhyd.2018.11.008

WEI, L. 2012. Sequential Coupling of Geochemical Reactions With Reservoir Simulations for Waterflood and EOR Studies. SPE Journal 17 (2), doi: 10.2118/138037-PA

WIEGMANN, A., Iliev, O., Schindelin, A. 2010. Computer Aided Engineering of Filter Materials and Pleated Filters. In: Global Guide of the Filtration and Separation Industry. VDL-Verlag, Rödermark, 191-198

WILDE, F., Ogurreck, M., Greving, I., Hammel, J.U., Beckmann, F., Hipp, A., Lottermoser, L., Khokhriakov, I., Lytaev, P., Dose, T., Burmester, H., Müller, M., Schreyer, A. 2016. Micro-CT at the Imaging Beamline P05 at PETRA III. AIP Conference Proceedings 1741, 030035, doi: 10.1063/1.4952858

XIE, M.L., Kolditz, O., Moog, H.C. 2011. A geochemical transport model for thermo-hydro-chemical (THC) coupled processes with saline water. Water Resour. Res. 47, doi: 10.1029/2010WR009270

XIONG, Q., Joseph, C., Schmeide, K., Jivkov, A.P. 2015. Measurement and modelling of reactive transport in geological barriers for nuclear waste containment. Phys. Chem. Chem. Phys. 17, 30577-30589, doi: 10.1039/C5CP05243B

XU, T., Sonnenthal, E., Spycher, N., Zhang, G., Zheng L., and Pruess, K. 2012. TOUGHREACT: A simulation program for subsurface reactive chemical transport under nonisothermal multiphase flow conditions. In: Groundwater Reactive Transport Models. F. Zhang, G.-T. Yeh, and J.C. Parker (eds.), Bentham Science, 74-95, doi: 10.2174/97816080530631120101

YEKTA, A.E., Pichavant, M., Audigane, P. 2018. Evaluation of geochemical reactivity of hydrogen in sandstone: Application to geological storage. Applied Geochemistry 95, 182-194, ISSN 0883-2927, doi: 10.1016/j.apgeochem.2018.05.021

YOON, H., Valocchi, A.J., Werth, C.J., Dewers, T. 2012. Pore-scale simulation of mixing-induced calcium carbonate precipitation and dissolution in a microfluidic pore network. Water Resour. Res. 48, W02524, doi: 10.1029/2011WR011192.

YOON, H., Kang, Q., Valocchi, A. 2015. Lattice Boltzmann-based approaches for pore-scale reactive transport. Rev. Mineral. Geochem. 80, 393-431, doi: 10.2138/rmg.2015.80.12

YOON, H., Major, J., Dewers, T., Eichhubl, P. 2017. Application of a pore-scale reactive transport model to a natural analog for reaction-induced pore alterations. Journal of Petroleum Science and Engineering 155, 11-20, ISSN 0920-4105, doi: 10.1016/j.petrol.2017.01.002.

Conference contributions

Hinz, C., Enzmann, F., Kersten[1], M. 2019. Pore scale modeling of calcite cement dissolution in a reservoir sandstone matrix. 16th International Symposium on Water-Rock Interaction, Tomsk, Russia

Hinz, C., Enzmann, F., Kersten[1], M. 2018. Pore-scale simulation of calcite cement dissolution in sandstone. Goldschmidt Abstracts, 2018, 1021. 28th Goldschmidt conference 2018, Boston, USA

Hinz[1], C., Enzmann, F., Kersten, M. 2018. Pore-scale simulation of kinetic calcite pore cement dissolution in a µCT sandstone sample. 10th Interpore conference 2018, New Orleans, USA

Hinz[1], C., Enzmann, F., Kersten, M. 2017. Dynamic simulation of kinetic calcite dissolution in a µCT-generated pore space. Goldschmidt Abstracts, 2017, 1641. 27th Goldschmidt conference 2017, Paris, France

Hinz[1], C., Enzmann, F., Kersten, M. 2017. Dynamic simulation of pore scale reactive transport in geological porous media. Book of abstracts of International Conference on Porous Media (InterPore), ISSN 2518-3826 (electronic), 378. 9th Interpore conference 2017, Rotterdam, Netherlands

Hinz[1], C., Enzmann, F., Becker, J., Kersten, M. 2016. Dynamic simulation of pore scale precipitation in geological porous media. 1st Meeting of the German National Chapter of InterPore 2016, Leipzig, Germany

Hinz, C., Enzmann, F., Chagneau, A., Schäfer, T., Glatt, E., Kersten[1], M. 2016. Dynamic simulation of diffusion controlled celestite precipitation in a µCT-generated pore space. Goldschmidt Abstracts, 2016, 1121. 26th Goldschmidt conference 2016, Yokohama, Japan

Hinz, C., Enzmann[1], F., Schäfer, T., Glatt, E., Kersten, M. 2016. Dynamic simulation of diffusion controlled celestite precipitation in pore scale porous media. Book of abstracts of International Conference on Porous Media (InterPore), ISSN 2518-3826 (electronic), 37. 8th Interpore conference 2016, Cincinnati, USA

Hinz[1], C., Enzmann, F., Schäfer, T., Glatt, E., Kersten, M. 2015. Dynamic simulation of diffusion controlled celestite precipitation in porous media. 7th Interpore conference 2015, Padua, Italy

Ruecker[1], M., Bartels, W.-B., Berg, S., Mahani, H., Ott, H., Georgiadis, A., Brussee, N., Coorn, A., van der Linde, H., **Hinz, C.**, Jacob, A., Wagner, C., Henkel, S., Enzmann, F., Bonnin, A., Stampanoni, M., Hassanizadeh, S.M., Blunt, M. 2016. Goldschmidt Abstracts, 2016, 2670. 26th Goldschmidt conference 2016, Yokohama, Japan

[1] Presenting author

Appendix

Supplementary material is attached as DVD containing (1) the code script files and default input text files. (2) The automated MATLAB post-processing tools are attached alongside other useful scripts for processing ReacDict and GeoDict data. In addition, (3) the initial geometries are copied to the DVD. (4) Animations are supplemented representing data at a volume of several hundreds of GB. Accordingly, final data files are not copied to the disk due to the limitation in storage capacity. Further data is available on request.

PhreeqC Data

```
SOLUTION 1
 unit mol/kgw
 pH 6.31999
 pe 10.8479
 temp 60
 C 0.000342799
 Ca 2.049
 Cl 8.98699
 Na 4.89
 -water 1
END
SELECTED_OUTPUT; -reset false; -pH true; -pe true; -temp true; -totals C Ca Cl Na
 -kinetic_reactants Calcite
 -saturation_indices CO2(g)
USE solution 1
KINETICS 1
Calcite
 -m0 0.000110355
 -m 0.000110355
 -parms 6000 1 2.592e+06 1.04645e-05
 -time 1 s
END
```

Fig. 55. Random IPhreeqc input 1

This input text is extracted from stored log data of the calcite pore cement dissolution simulation after 3 s of flow time.

The kinetic calcite reaction calculation concerns three voxel surfaces with a minor amount of solid calcite in each of the three neighbored voxels. This kinetic reaction is independent of the virtual particles, although the pore fluid in the current voxel is altered by the solution containers.

```
SOLUTION 1
 unit mol/kgw
 pH 6.23309
 pe 11.0064
 temp 60
 C 0.000277956
 Ca 1.66053
 Cl 7.28306
 Na 3.96286
 -water 25
END
SOLUTION 2
 unit mol/kgw
 pH 6.25438
 pe 10.9871
 temp 60
 C 0.00027981
 Ca 1.67098
 Cl 7.32896
 Na 3.98783
 -water 1
END
SELECTED_OUTPUT; -reset false; -pH true; -pe true; -temp true; -totals C Ca Cl Na
 -kinetic_reactants Calcite
 -saturation_indices CO2(g)
MIX
 1 0.5
 2 0.5
SAVE solution 3
END
USE solution 3
KINETICS 1
Calcite
 -m0 51.7281
 -m 51.7281
 -parms 4000 1 2.592e+06 8.81473e-06
 -time 0.9 s
END
```

Fig. 56. Random IPhreeqc input 2

This input text is extracted from stored log data of the calcite pore cement dissolution simulation after 56 s of flow time.

SOLUTION 1 illustrates the carried solution of a virtual particle with a mass multiplicity of 25, which is mixed with the pore fluid solution of the current voxel (SOLUTION 2). The resulting aqueous solution 3 is used for the kinetic reaction calculation, which concerns two voxel surfaces with a major amount of solid calcite in both neighbored voxels and a reaction time of 0.9 s.

```
RATES

Calcite
        -start
1       REM   PARM(1) = specific surface area of calcite, cm^2/mol calcite
2       REM   PARM(2) = exponent for M/M0

10      si_cc       = SI("Calcite")
20      IF (M <= 0  and si_cc < 0) THEN GOTO 200
30      k1          = 10^(0.198 - 444.0 / TK )
40      k2          = 10^(2.84 - 2177.0 /TK )
50      IF TC <= 25 THEN k3 = 10^(-5.86 - 317.0 / TK)
60      IF TC > 25 THEN k3 = 10^(-1.1 - 1737.0 / TK )
80      IF M0 > 0 THEN area = PARM(1) * M0 * (M/M0)^PARM(2) ELSE area = PARM(1) * M
110     rate        = area * (k1 * ACT("H+") + k2 * ACT("CO2") + k3 * ACT("H2O"))
120     rate        = rate * (1 - 10^(2/3*si_cc))
130     moles       = rate * 0.001 * TIME # convert from mmol to mol
200     SAVE moles
        -end
```

Fig. 57. PhreeqC v3.4 RATES data block for kinetic calcite reactions

This RATES block has been used by ReacDict simulations onto the dissolution of calcite pore cements.

```
RATES

Calcite
        -start
1       REM   PARM(1) = reactive surface area
2       REM   PARM(2) = initially exponent for M/M0, actually unused
3       REM   PARM(3) = AlterationFactor for ReacDict to determine max moles for dissolution
4       REM   PARM(4) = Max moles for precipitation

10      si_cc       = SI("Calcite")
20      IF (M <= 0  and si_cc < 0) THEN GOTO 200
30      k1          = 10^(0.198 - 444.0 / TK )
40      k2          = 10^(2.84 - 2177.0 / TK )
50      IF TC <= 25 THEN k3 = 10^(-5.86 - 317.0 / TK)
60      IF TC >   25 THEN k3 = 10^(-1.1 - 1737.0 / TK )
100     area        = PARM(1)
110     rate        = area * (k1 * ACT("H+") + k2 * ACT("CO2") + k3 * ACT("H2O"))
120     rate        = rate * (1 - 10^(2/3 * si_cc))        # area * (rate_f – rate_b)
130     moles       = rate * 0.001 * TIME                  # convert from mmol to mol
140     IF si_cc > 0 THEN GOTO 190
150     IF si_cc = 0 THEN GOTO 200
160     IF moles < -1 * M / PARM(3) THEN moles = -1 * M / PARM(3)
190     IF moles > PARM(4) THEN moles = PARM(4)
200     SAVE moles
        -end
```

Fig. 58. Adjusted RATES data block for kinetic calcite reactions

This RATES block has only been used at the simulation of calcite pore cement dissolution. The input for parameter (1) was changed from SSA to the reactive surface area while parameter (2) has rendered obsolete at this point, so that it doesn't interfere with the surface roughness factor. Parameters (3) and (4) have been implemented to limit pore alteration to the available volume in order to prevent numerical errors.

Description of data input

Table 18. List of general input parameters

Grey lines highlight deprecated input.

General input keyword	Parameter type	Function
PCname	String	PC name; necessary for GeoDict MPI execution. Alternatively, use multiple threads instead of multiple processes.
DebugMessages	true or false	Extended output parameters
begin	Integer	Begin step, you can change this parameter to restart your simulation from step *value*. Alternatively have a look at command line parameters.
NumberOfTimeSteps	Integer	Number of timesteps performed by ReacDict. Overwrites *days* keyword.
days	Double	Alternatively calculates the number of timesteps.
KeepDir	Integer	Keep the last *value* timestep directories. Type "0" to keep all timesteps.
Saveruns_Xs	Integer	Store a timestep directory whenever *value* seconds have been simulated.
FlowDict	true or false	Use advective transport if set to *true*.
FlowDictExecutable	String	Full path to FlowDict executable, e.g., */geodict/LIR*
AddiDictExecutable	String	Full path to AddiDict executable, e.g., */geodict/GD2018Tracker64*
mpiexec	String	Your MPI execution command (necessary for GeoDict MPI execution). Default is *mpiexec*.
FileNaming	String	This *string* will change FlowDict file names.
Directory	String	Full path to your Project Directory. It is created if non-existent.
PresetGDT	String	Your geometry as GeoDict structure. See Matlab processing tools if you do not have a *.gdt* file.
PresetGPP	String	An actual *.gpp* file. The header string is of importance.
PresetVAP	String	A *.vap* file according to your *preset_gdt* geometry. Not necessary if *FlowDictEachTimeStep true* or *StructureChanged true*.
PresetGFR	String	A *.gfr* file according to your *preset_gdt* geometry.
PhreeqcDatabase	String	Full path to your chosen PhreeqC database.

Table 19. List of ReacDict input parameters

Grey lines highlight deprecated or expert input parameters.

Input keyword	Type	Function
AlterationFactor	Float	The given value is multiplied with calculated pore alteration. In this way, you might want to accelerate your simulation. However, it is highly recommended to set *DebugMessages true* and to check this value manually in PhreeqC runs so that pore alteration does not become higher than available space.
ClosedPoresMaterial	Integer	If material number is used at the input geometry, then these voxels are checked for being open pore whenever particles are nearby.

Input keyword	Type	Function
CombineParticles	true or false	Combines particles by employing the –water PhreeqC keyword. This option reduces the number of particles and, thereby, the computational time.
CombineParticlesOnlyInitial	true or false	Useful option, IF PhreeqC errors occur due to high –water values.
DiffusionCoefficient	Doubles	Diffusion coefficients for each Solution in the same order as the Solution keywords. Separated by commas (no spacebars).
FlowDictEachTimestep	true or false	Initializes FlowDict at each timestep
GeochemTimestep	double	The geochemical calculation interval [s]. This has to be a multiple of *AD.Trajectories.TimeStep*.
InflowSolutionNumber	Integer	Number of Solution applied for inflow particles (used if *FlowDict true*).
InflowBarrierMaterial	Integer	See *InflowParticleBarrier*. Please consider that particles should not be able to stick to that material after collisions.
InflowParticleBarrier	true or false	Creates a Barrier at the inflow for particle transport simulation (highly recommended for low Péclet numbers). Material number is defined by *InflowBarrierMaterial*.
MaterialPhases	Strings	Reactive material names as used by PhreeqC. Strings separated by commas (no spacebars, e.g.: Calcite,Aragonite). These materials need specifications (see Table 21).
MaxNumberOfParticles	Integer	Maximum number of particles limits ReacDict runtime. This option requires *CombineParticles* true. Not compatible with *NewParticlesBasedOnFlow* true and thus deprecated.
MixPercentual	true or false	true: MIX xy 1/#solutions; false: MIX xy 1
n_interacting	Integer	The number of particles. If *FlowDict false*: total number of particles. If FlowDict true: Number of particles inflowing each timestep (deprecated).
NewParticlesBasedOnFlow	true or false	Particles are created at the inflow plane according to the velocity and time step. In combination with *CombineParticles*, there is a significant reduction of AddiDict runtimes.
NonReactiveMaterial	Integer	Precipitation permitted at surfaces of this material-no if no other surface is present.
OtherMaterial	Integer	Precipitation allowed at surfaces of this material-no.
PhreeqcSpecies	Strings	The elements used at Solution in the appropriate order. Strings separated by commas (no spacebars, e.g.: Ca,C,Cl).
PhreeqcPressure	Double	Always uses this value in PhreeqC calculations if it's different from the default value ($1\ atm$). Consider the pressure range of the chosen PhreeqC database.
PoreFluidSolutionNumber	Integer	Number of Solution applied for all pore fluid solutions (if *FlowDict false* excl. *ZReservoirVec*).
PorousDissIfNoSurface	true or false	Takes care of porous "artefacts" depending on *SurfaceReactionOnly true*.
Solution	Floats	One keyword-block for each solution, later on numbered beginning from 0. Separated by commas (no spacebars): pH,temp,[pe,]PhreeqcSpecies
StructureChanged	true or false	Initializes FlowDict at first step if set to *true*.
SurfaceReactionOnly	true or false	Reactions are calculated only at solid surfaces (voxels next to solid materials).

Input keyword	Type	Function
SkipVoxel	Integer	If *NewParticlesBasedOnFlow true* and *CombineParticles true*: reduces number of inflow particles to max 1 particle at each square of NxN voxels. Default is 3; this value depends on (1) ROI size and (2) flow velocity.
TrackSpecies	Strings	Species for whom an output file is created each timestep containing values for all voxels. Separated by commas (no spacebars), e,g,; HCO3-,Ca+2
ZReservoirVec	Integers	One keyword block for each reservoir (if *FlowDict true* only one reservoir is applied). Creates a reservoir box from z0-z1 across all x and y. Not considered if *NewParticlesBasedOnFlow true*. Separated by commas (no spacebars): z-voxel-no-begin, z-voxel-no-end, Solution-no

Table 20. Geochemical fluid specifications

Fluids are characterized by either "*InflowSolution.no.name value*" or "*PoreSolution.no.name value*". However, only one inflow solution is possible at the current ReacDict version. Example: *PoreSolution.1.Cl 3.268e-6*. Grey lines highlight expert settings.

Input keyword	Type	Function
PoreSolution.no.pH	Double	pH value of solution no X. Numbers start at 1.
.no.temp	Double	Temperature in K.
.no.pe	Double	Redox sensitivity, necessary for kinetic reactions
.no.elementname	Double	For any concentrations, element abbreviations must be used according to PhreeqC, e.g., Cl, Ca, C or C(4)
InflowSolution.no.Diffusivity	Double	Diffusion coefficient, required only for inflow solution
InflowSolution.no.CollisionParameters	Doubles	Default: 0.5,0 (restitution, adhesion). For restitution values smaller than one, energy is absorbed by the collision and the particle slows down. For example, a 0.5 restitution value means that a particle loses half of its velocity in the collision and gets 50% slower. The adhesion (Hamaker constant) is by default set to 0 to prevent particles from sticking to solid surfaces. Separated by commas (no spacebars). Accordingly, the ReacDict default collision model is the Hamaker model.
InflowSolution.no.areaXXYYZZ	Integers	Default: 0,*nx*,0,*ny*,0,0 (in voxels). Defines the particle creation volume. By default the inflow plane.
PoreSolution.no.areaXXYYZZ	Integers	De fault: 0,*nx*,0,*ny*,0,*nz* (in voxels). Defines the volume determined by the solution given for PoreSolution no X. By default the entire volume. However, multiple solutions may be forwarded for defining the initial setup.

Table 21. Material specifications

Keywords are written as, e.g., *Materialname*.MaterialNumber and must be specified at any line after *MaterialPhases*. Example: *Calcite.MaterialNumber 2*

Input keyword	Type	Function
MaterialNumber	Integer	Material number used in geometry file (evtl. also in *PresetGDT*)
Calculation	String	Specifies the way PhreeqC calculates the dissolution (and precipitation): *kinetic* or *equilibrium*
Density	Double	Material density in kg/m³
MolarMass	Double	Molar mass of material. E.g., 100.096 for pure Calcite ($CaCO_3$)
SurfaceRoughnessFactor	Double	A global factor for material dissolution

Table 22. AddiDict input parameters

AddiDict is tested with particles defined at molecule size ($m \to 0$). Accordingly, different settings possibly won't work. Grey lines highlight expert settings.

Input keyword	Parameter type	Function
TimeStepInSec	Double	Timestep in seconds. In AddiDict GUI called maximal time.
AD.DiffusionOnly	true or false	Used if *FlowDict false*: if then set to *false*, your *PresetVAP* file will always be used.
AD.Trajectories.TimeStep	Double	The accuracy for performing particle motion [s]. This has to be chosen in consideration of *GeochemTimestep*.
AD.LicenseFileName	String	Full path to your GeoDict license file (*.lic*).
AD.NumberOfProcesses	Integer	Determines the number of MPI processes used by AddiDict
AD.NumberOfThreads	Integer	Determines the number of threading cores used by each *AD.NumberOfProcesses*
AD.VoxelLength	Double	The isotropic voxel length (in x, y, z). Thus, only one parameter is possible.
AD.MaterialIDs	Integers	The material numbers used according to your input parameters. Separated by commas (no spacebars). These have to be defined at *AD.Material* (see below).
AD.FluidDensity	Integer	The density [kg/m^3] of your pore fluid *PoreFluidSolutionNumber*. Applied at fixed particle size.
AD.Temperature	Double	The temperature in Kelvin. Applied at fixed particle size.
AD.KinematicViscosity	Double	The kinematic viscosity [m^2/s] of your *PoreFluidSolutionNumber*. Applied at fixed particle size.
AD.ParticleMotionUDFFileName	String	If you choose *AD.UseParticleMotionUDF true*, this file (*.so*) will be used (expert setting).
AD.UseParticleMotionUDF	true or false	Use an alternative UDF file for influencing the particle motion (expert setting).
AD.ParticleDistribution.DensityValue	Double	One density value [kg/m^3] for all of your particles.
AD.CollisionParameters	Doubles	AddiDict collision parameters according to your input parameters. Look at AddiDict *.pde* files or use GeoDict descriptions for more details. Separated by commas (no spacebars). Deprecated input parameter.
AD.BrownianMotion	true or false	Enables the diffusive motion of particles.
AD.CunninghamCorrection	true or false	Enables the use of *AD.CunninghamLambda* for correcting the diffusive motion of particles. Applied at fixed particle size.
AD.CunninghamLambda	Double	Your Cunningham correction factor.
AD.OutletLength	Integer	AddiDict outlet length, default is *0*.
AD.SlidingOn	true or false	Enables sliding. Default is *false*
AD.StoreCollisions	true or false	Count and store the number of collisions in *TrackerFinalParticles.gpp*
AD.TrapCodeStalledParticles	Integer	Trapped particles get the status *value*. Default is *34*.

Input keyword	Parameter type	Function
AD.TimeStepScaling	Double	Scales AD.Trajectories.TimeStep, expert parameter
AD.WithEstatic	true or false	Includes electrostatic effects. Default is *false*.
AD.WriteCollisionNormal	true or false	Default is *false*.
AD.Material	Integer,Strings	One keyword block for each material defined in *AD.MaterialIDs* and for material number 0. Separated by commas (no spacebars): *material-no, material (Water, Calcite, Manual), material-type (Fluid, Solid, Porous), [if Porous: Fluid-name(Water)], Information-string*

Table 23. FlowDict input parameters (LIR solver)

FlowDict is tested with the LIR solver. Thus, in this version of ReacDict, FlowDict should be run with that configuration. The parameters in this table are applied if the keyword *FlowDict* is set to *true*, otherwise these parameters do not need to be defined. Grey lines highlight expert settings or default values that need no editing.

Input keyword	Parameter type	Function
FD.Equation	String	The equation used for computing the flow field. The default is *NAVIERSTOKES_BRINKMAN* (LIR solver). Also recommended for performance reasons: *STOKES_BRINKMAN*.
FD.FlowBoundary	String	Boundary condition in flow direction. Default: *Symmetric*
FD.FlowDirection	String	The default string is *z*
FD.Fluid	String	The default string is *Water*.
FD.InletLength	Integer	The length of your inlet in voxels.
FD.MaxIterationNumber	Integer	Stopping criterion for FlowDict.
FD.MaxRunTime	Integer	Stopping criterion for FlowDict [seconds].
FD.NumberOfProcesses	Integer	Number of cores used for multithreading.
FD.NumberOfRefinements	Integer	Default *value* is *10*. Used if *FD.Refinement Enabled*
FD.PhysicalDensity	Double	Density of your fluid [kg/m^3].
FD.PhysicalViscosity	Double	Viscosity of your fluid at given temperature.
FD.PressureDifference	Double	The pressure difference from inflow to outflow.
FD.Refinement	String	Choose *Enabled* or *Disabled*.
FD.Relaxation	Double	Should be a value from *0-2* (stable-fast computation). Decrease value, if necessary due to FlowDict errors. Default is *1*.
FD.RelaxationPressure	Double	See GeoDict information for more details.
FD.RelaxationVelocity	Double	See GeoDict information for more details.
FD.StoppingErrorBound	Double	Stopping criterion for FlowDict. Exact FlowDict error, so choose <=1. Default is *0.01* implying an error of 1 %.
FD.StoppingTolerance	Double	Stopping criterion for FlowDict. Choose <=1
FD.TangentialBoundaryX	String	Boundary condition in X direction. Default: *Symmetric*
FD.TangentialBoundaryY	String	Boundary condition in Y direction. Default: *Symmetric*
FD.UseErrorBound	Integer	Enable the use of *FD.ErrorBound*. Use *0* or *1*.
FD.UseLateral	Integer	Enable the consideration of tangential convergence parameteres. Use *0* or *1*.
FD.UseMaxIterations	Integer	Enable the use of *FD.MaxIterationNumber*. Use *0* or *1*.
FD.UseMaxTime	Integer	Enable the use of *FD.MaxRunTime*. Use *0* or *1*.
FD.UseTolerance	Integer	Enable the use of *FD.StoppingTolerance*. Use *0* or *1*.

Description of data output

Table 24. Data files

ReacDict and the coupled GeoDict software store a number of files at any timestep. These files are either required as input data for the execution (or restart) of ReacDict or are given as data for post-processing purposes.

File name	Data
geometry.gdt	GeoDict compressed structure file
***.pde**	FlowDict / AddiDict input parameters
***.vap**	FlowDict flow/pressure field
***.gfr**	FlowDict flow resistivity
***results.txt**	FlowDict computation results (permeability, velocity)
***.log**	FlowDict log file
TrackerInitialParticles.gpp	AddiDict input particle positions, types, offset time
TrackerFinalParticles.gpp	AddiDict particle positions at the end of the timestep
Trajectories.gpt	AddiDict particle positions as paths
***summary*.log**	ReacDict log file containing cumulative results
pCO2.rd	ReacDict 3D data: CO2 partial pressure in atm
phases.rd	ReacDict 3D data: voxel-fractions for reactive mineral phases
KinPoreFluidReac1d.rd	ReacDict 3D data: Boolean values for continuing local kinetic reactions
Solutions.rd	Aqueous solution details, particle-related
TrackMolality1d.rd	ReacDict 3D data: optional dataset tracking (multiple) user-defined species
VoxelSolution.rd	ReacDict 3D data: Aqueous solution details, voxel-related

Matlab processing tools

Table 25. Matlab visualization tools

A set of data processing functions is available. However, for processing GeoDict files the GeoDict module GeoLab might also be used. The available codes read ReacDict and GeoDict files and are capable of visualizing ReacDict data in 2D images concerning the parameters in this table. Data can automatically be processed on consecutive time steps. Thereby, the plots can be organized as Matlab subplots. However, flow files need to be uncompressed in order to be readable by Matlab functions and the C++ code. Readable files without given plotting possibility are sufficiently visualizable within GeoDict (excluding Solutions.rd). With additional knowhow and effort, vectorized parameters are principally visualizable within GeoDict and other 3D visualization software (e.g., Avizo).

Readable file	Parameters that can be visualized in Matlab as a 2D image/plot
.vap (FD flow/pressure field)	2D Péclet number
TrackerFinalParticles.gpp (AD)	3D Particle distribution
geometry.gdt (GD)	---
.gfr (FD flow resistivity)	---
Trajectories.gpt (AD)	---
Solutions.rd	---
TrackMolality1d.rd	Molality as defined by *TrackSpecies*
VoxelSolution.rd	pH, temp, pe, species as defined by *PhreeqcSpecies*
pCO2.rd	$pCO_2 \Rightarrow \log pCO_2 = SI\ CO_2(g)$
phases.rd	Exact voxel porosity of reactive materials. Pore alteration rate
***summary_run*.log**	Time resolved: Reaction rate (mol/Ls), Damköhler number, core hours, runtime, Number of particles, Alteration/reaction
***results.txt (FD)**	Global Péclet number

Readable file	Parameters that can be visualized in Matlab as a 2D image/plot
***results.txt, *summary*.log**	Porosity permeability plot
.gdt, phases.rd, *summary*	Reaction rate (mol/m²s)

PhreeqC data input

Table 26. PhreeqC keyword data blocks employed by ReacDict

PhreeqC is fully implemented into ReacDict by making use of the C++ library IPhreeqc. The hydrogeochemical code is coupled to particle and pore fluid solutions mixing with each other and performing reaction calculations wherever necessary. Therefore, a set of keyword data blocks are employed as listed in this table, which is based on Parkhurst and Appelo (2013).

Keyword data block	Function
EQUILIBRIUM_PHASES	Define assemblage of minerals and gases to react with an aqueous solution
KINETICS	Specify kinetic reactions and define parameters
MIX	Define mixing fractions of aqueous solutions
SELECTED_OUTPUT	Print specified quantities to a user-defined file. IPhreeqc enables direct access to selected values without writing any files.
SOLUTION	Define the composition of an aqueous solution
SAVE	Save results of batch reactions for use in subsequent simulations
USE	Select aqueous solution or other reactants that define batch reactions

Curriculum Vitae

Christian Hinz

Geoscientist

Contact: christian.hinz@uni-mainz.de
christian.hinz@math2market.de

Professional experience

01/2019 – today	Application Specialist Digital Rock Physics Math2Market GmbH, Kaiserslautern
01/2016 – 12/2018	Research Assistant (BMWi-project HyINTEGER) JGU Mainz, Hydrogeochemistry group
04/2014 – 12/2015	E-commerce employee ergo Bachmann & Palkovich GmbH, Wiesbaden
08/2013 – 10/2014	Student employee, digitization of the collection Museum Wiesbaden, Natural history collection
04/2011 – 12/2015	Student Assistant positions: Trainer Geological Working Methods, Programming with R, Python and MATLAB JGU Mainz, Institute for Geosciences

Education

08/2015 – 08/2019	Doctoral studies: Geology/Palaeontology JGU Mainz, Institute for Geosciences *Reactive flow in porous media based on numerical simulations at the pore scale*
10/2012 – 07/2015	M.Sc. Geosciences JGU Mainz, Institute for Geosciences
04/2010 – 10/2012	B.Sc. Geosciences JGU Mainz, Institute for Geosciences